AC-driven Quantum Phase Transitions

Nonequilibrium aspects of criticality

Vorgelegt von MSc.

Victor Manuel Bastidas Valencia

aus Santiago de Cali

von der Fakultät II – Mathematik und Naturwissenschaften
der Technischen Universität Berlin

zur Erlangung des akademischen Grades

Doktor der Naturwissenschaften

— Dr. rer. nat. —

genehmigte Dissertation

Promotionsausschuss

Vorsitzende	:	Prof. Dr. rer. nat. Janine Maultzsch, TU Berlin
1. Gutachter	:	Prof. Dr. rer. nat. Tobias Brandes, TU Berlin
2. Gutachter	:	Prof. Dr. rer. nat. Michael Thorwart, Uni- Hamburg

Tag der wissenschaftlichen Aussprache: 31. January 2013

Berlin, 2013
D 83

Contents

To the memory of my father and my dear friend Arcelia Ortega.

Abstract

The development of novel experimental techniques to externally control manybody systems has been extensively increased in the last years. A manybody phenomenon of fundamental interest is a quantum phase transition (QPT). The typical description of nonequilibrium QPTs is based on the fact, that the external control renormalizes the parameters of the system, in such a way the critical points are shifted from the equilibrium values. From this point of view, the non-stationary dynamics of the system still resembles the equilibrium behavior. This thesis focuses on the theoretical description of quantum criticality under the effect of monochromatic driving. Our approach reveals an allowance of a unique possibility to explore novel states of matter and effective interactions which are absent in equilibrium systems by means of driving. We explore aspects of nonequilibrium criticality in models in $(d+1)$-dimensions, which exhibit second-order QPTs in the absence of driving. In this work d stands for the spatial dimension and 1 corresponds to the temporal dimension.

First, we investigate two models in spatial dimension $d = 0$: the Dicke model and the Lipkin-Meshkov-Glick model. In equilibrium, a mean-field description of the energy landscape of these models shows a transition from a monostable to a bistable configuration at the critical point. Intriguingly, our analysis reveals the existence of a complex multistable structure of the quasienergy landscape for the driven models. For example, while the undriven Dicke model only undergoes a second-order QPT, the driven model exhibits a new non-equilibrium first-order QPT.

In $d = 1$, we investigate the quantum Ising model in a transverse field. In addition to the appearance of a Ising-like transition occurring at a shifted critical point, the external field induces infinite anisotropic transitions between two different ferromagnetically ordered phases.

Finally, in $d = 2$, we investigate the Wen-plaquette model. In the driven case besides the spin polarized trivial phase and the conventional topologically ordered phase, the system reveals the existence of a new topological phase. To describe the topological quantum phase transition (TQPT), we introduce generalized "string-like" cycle-averaged order parameters.

Zusammenfassung

In den letzten Jahren zeigte die Entwicklung von experimentellen Methoden, um Vielteilchenquantensysteme zu kontrollieren, beträchtliche Fortschritte. Eines der interessantesten Vielteilchenquantenphänomene sind Quantenphasenübergänge. Die typische Beschreibung von Nichtgleichgewichtsquantenphasenübergängen basiert auf der Tatsache, dass die Parameter des Systems durch die externe Kontrolle renormalisiert werden, sodass sich die kritischen Punkte vom Gleichgewichtspunkt verschieben. Aus dieser Sicht ähnelt die nicht-stationäre Dynamik des Systems dem Verhalten im Gleichgewicht. Die theoretische Betrachtung des kritischen Verhaltens unter Nichtgleichgewichtsbedingungen steht im Fokus dieser Arbeit. Überraschenderweise werden in einem monochromatisch getriebenen System neue Zustände der Materie und effektive Wechselwirkungen erzeugt, die im Gleichtgewicht abwesend sind. Im Allgemeinen wird das kritische Verhalten von $(d+1)$-dimensionalen Quantensystemen untersucht, die im Gleichtgewicht einen Quantenphasenübergang zweiter Ordnung zeigen. In Rahmen dieser Arbeit wird d für die räumliche Dimension und 1 für die zeitliche Dimension stehen.

Als erstes beschäftigen wir uns mit zwei nulldimensionalen Modellen: dem Dicke-Modell und dem Lipkin-Meshkov-Glick-Modell. Im Gleichgewicht zeigt eine "Mean-Field"-Betrachtung der Energielandschaften, dass die Systeme am kritischen Punkt einen Übergang vom "mono-stabilen" zum bistabilen Bereich aufweisen. Interessanterweise zeigt unsere Untersuchung eine komplexe, multi-stabile Struktur von Quasienergielandschaften für den getriebenen Fall. Zum Beispiel während das Dicke-Modell im ungetriebenen Fall nur einen Phasenübergang zweiter Ordnung zeigt, zeigt das getriebene Modell zusätzlich einen neuen Nichtgleichgewichtsquantenphasenübergang erster Ordnung.

Für den Fall $d = 1$ untersuchen wir das Quanten-Ising-Modell in einem zeitperiodischen, transversalen Feld. Neben dem Ising-typischen Phasenübergang an einem verschobenen kritischen Punkt, induziert das äußere Feld unendlich viele anisotropische Übergänge zwischen unterschiedlichen ferromagnetisch geordneten Phasen.

Schlussendlich, für $d = 2$, betrachten wir das Wen-Plaquetten-Model. Wir werden sehen, dass im getriebenen Fall – neben der trivialen Spin-polarisierten Phase und der gewöhnlichen topologisch geordneten Phase – das System neuartige topologische Phasen zeigt. Um diese topologischen Quantenphasenübergänge zu beschreiben, führen wir verallgemeinerte "String-ähnliche", über eine Periode gemittelte Ordnungsparameter ein.

Acknowledgments

First of all, I would like to deeply thank Tobias Brandes for give the opportunity and the honor to work in his group and for being my Doktorvater, his academical and personal support have been fundamental in the development of this work. His vision of physics and his amazing lectures kept me motivated and enthusiastic during these years.

I am deeply grateful to Clive Emary for being my co-supervisor, and especially for his infinite patience to explain me the more abstract concepts of physics. He was always available for discussions and his enthusiasm in physics was a continuous motivation.

I am very thankful to Michael Thorwart for the inspiring discussions about Floquet theory, for the possibility to visit his group, and for agreeing to be the second evaluator (2. Gutachter).

I also thank Janine Maultzsch for agreeing to be the chairwomen (Vorsitzende).

I am grateful to Gloria Platero for inviting me to Instituto de Ciencia de materiales de Madrid (ICMM-CSIC), and to Gergerly Zaránd for inviting me to Budapest University of Technology and Economics.

Furthermore, I like to thank all the people of my group at TU Berlin. Especially to my friend and colleague Philipp Strasberg for our interesting discussions about physics. Christina Pöltl and Christian Nietner, sharing the office with me, had always time for informal discussions about physics during the expresso pause. I am thankful to Mathias Hayn, Christian Nietner, Gernot Schaller, and Malte Vogl for the discussions about the intricacies of criticality in nonequilibrium and for the proof-reading of this work. I thank my colleagues Georg Engelhardt and Benjamin Regler for their enthusiasm in our collaboration. Together, we have discovered many aspects of criticality under the effect of driving.

I am thankful for the financial support of the Deutscher Akademischer Austausch Dienst (DAAD) during my studies.

I would like to thank my "little" brother Rodrigo Bastidas, and my friends, Vicente, Brahyan, Andres Lisimaco, Gina, Isabel, Michal, Pilar, Melissa and Tine for their moral support and friendship during this years.

Finally, I would like to thank Yuko Sato, the love of my life. She was the inspiration of the last two chapters of my thesis and the responsible for the last proof-reading of this work. I discover with her that love creates long-range correlations, which are stronger that the ones arising at quantum critical points.

1. Introduction

1.1. Quantum criticality in equilibrium

Symmetry breaking is a paradigm of condensed matter physics in which the states of matter are characterized as symmetry broken phases [1, 2], i.e., a solid corresponds to a broken translational symmetry, and a superconductor to a broken $U(1)$ abelian-Gauge symmetry.

Nature admits transitions between different states of matter driven by thermal fluctuations, which are referred to as classical phase transitions [2]. These phase transitions are characterized by the emergence of long-range spatial and temporal correlations when the system approaches the critical point. A beautiful aspect of the theory of critical phenomena is that universal power laws characterize the scaling of some physical quantities as they approach the critical point [2].

However, one question arises: what are the characteristics of a phase transition in the limit when the temperature goes to zero? In this limit, as is expected, the thermal fluctuations do not play any role, however, the quantum fluctuations can entirely drive a change of phase in the system, which corresponds to a quantum phase transition (QPT). In contrast to classical phase transitions, a QPT is characterized by a dramatic change of the ground state properties [3], and similarly to classical phase transitions, as the system approaches the critical point, the spatial and temporal characteristic length scales are divergent. In the case of second-order QPTs, the characteristic energy scale corresponds to the energy of the lowest excitation above the ground state [3]. For finite sizes, the spectrum of a typical system exhibits an anticrossing between the ground state and the first excited state at the critical point.

In contrast to second-order (continuous) QPTs, first-order QPTs are characterized by an exact crossing between the ground state and the first excited state in the finite size limit that still remains in the thermodynamic limit [4]. At the critical point, the ground state of the system is characterized by three-fold degenerate vacua. While the low energy behavior of a second-order phase transition is described by a $\lambda\phi^4$ Landau functional of the order parameter ϕ, the description of a first-order QPT requires a $\lambda\phi^6$ expansion [2, 4].

Rather recently, novel states of matter have been found which cannot be classified inside the paradigm of Landau symmetry breaking [5, 6]. These novel states of

matter are characterized by an intrinsic robustness against the effects of an environment as a consequence of the topological properties of the ground state. Examples of topological states of matter include the integer and fractional quantum Hall effect [7, 8], topological insulators and superconductors [9, 10, 11].

This novel manifestation of criticality in nature is characterized by transitions between different topological quantum numbers and corresponds to a topological quantum phase transition (TQPT). In the integer quantum Hall effect, the different topological phases correspond to the Hall Plateaus. A transition between states with different Hall conductance can occur without symmetry breaking. Therefore the transition is described by a change in the Chern numbers, which characterize the topology of the system [10, 11].

1.2. Quantum criticality in nonequilibrium

In spite of the well known behavior of QPT in equilibrium systems, relatively little is known about the critical behavior under nonequilibrium conditions. In fact, one of the most intriguing issues here is the precise definition of a nonequilibrium QPT and the question of whether or not concepts such as nonanalyticities of the ground state, phase diagrams, critical exponents, scaling behavior etc. still hold then.

In general, the dynamics of nonequilibrium QPT has been addressed from slightly different conceptual points of view, depending on the way in which the nonequilibrium conditions are induced. Previous works have explored the evolution of systems that are slowly driven through the critical point. At this point, there is a diverging relaxation time and correlation length, therefore the dynamics cannot be adiabatic in the thermodynamic limit. This kind of effect is enclosed in the Kibble-Zurek mechanism [12, 13, 14]. Such nonadiabatic effects can be also discussed even when the temporal evolution follows a sudden change of the coupling constants of the system Hamiltonian [15]. Even if one prepares the system initially in a ground state of the undriven model, the situation becomes highly nontrivial under the effect of an external control, since the system will experience transitions to excited states.

Our particular interest in this thesis is focused on periodically-driven manybody systems. There is a surge in interest in ac-driven QPTs, among researchers of diverse communities [16, 17, 18, 19, 20]. The investigation of criticality under the effect of driving is interesting and relevant, not only from a fundamental point of view, but for future technological applications as a consequence of the current feasibilities of the experimental methods to control and simulate quantum many-body systems.

1.3. Experimental feasibilities

The current experimental setups allow for a high degree of control of the parameters of the system. Particularly, the possibility to experimentally explore the nonequilibrium dynamics of the system under the effect of an external driving is interesting. In quantum optics, the superradiant QPT [21, 22, 23] has been realized experimentally in a simulation of the Dicke model with a Bose-Einstein condensate in an optical cavity [24]. Such an experimental realization consists in a nonequilibrium setup that allows one to explore diverse aspects of criticality in the Dicke model; such as roton-type mode softening in a Bose-Einstein condensate with cavity-mediated long-range interactions [25], and spontaneous symmetry breaking by adiabatically crossing the critical point [26].

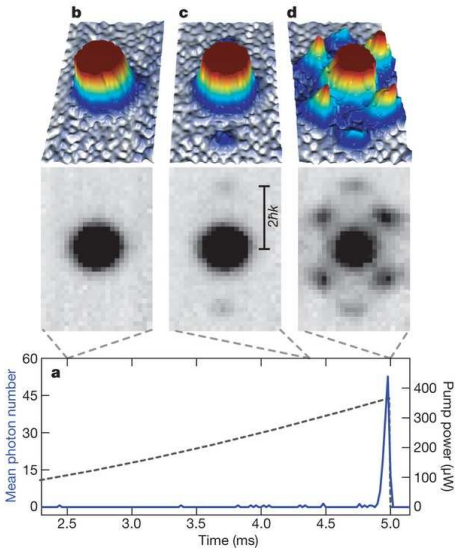

Figure 1.1.: Experimental observation of the superradiant transition [24]. (a) Depicts the adiabatic variation of the pump power, (b) and (c) the macroscopic occupation of the $k = 0$ mode, and (d) the macroscopic occupation of higher motional energy levels

In the experiment, the normal phase corresponds to the condensate phase of the atomic ensemble. By varying the intensity of an external pump laser, a macroscopic occupation of higher motional energy levels can be reached, which corresponds to the analogue of superradiant phase. Figure 1.1 depicts the experimental observation of the superradiant QPT.

Recently, experimental realizations of one-dimensional spin chains have been suggested, where a quantum simulation of the system close to the phase transition is possible, and a wide range of control of the parameters is accessible [27, 28, 29, 30, 31, 32]. Furthermore, the transition from a superfluid to a Mott insulator induced by means of monochromatic external driving predicted in Ref. [16] has been experimentally tested with Bose-Einstein condensates in optical lattices [33].

A realization of quantum magnets in a system of cold atoms placed in an optical lattice has been suggested [34, 35, 36], which allows the implementation of the spin-1/2 Kitaev model on a hexagonal lattice. This opens a new possibility to investigate spin systems with topological order [6]. These systems have a huge potential for applications in quantum information technologies as topologically-protected qubits. By controlling the tunneling and the self-interaction strength of the ensemble of cold atoms, it is possible to simulate anisotropic Heisenberg-like interactions of the effective spin system on a honeycomb lattice [34].

The description of nonequilibrium QPTs under the effect of monochromatic driving is addressed in this thesis. We assume that in equilibrium the system exhibits a second-order QPT, and we consider an external driving that preserves the symmetries of the undriven model. We investigate the effect that quantum resonances and symmetries have on the critical behavior. In particular, if the driving frequency is on resonance with collective excitations of the manybody system, we show that the system exhibits a behavior with no analogue in equilibrium. In previous works, the driving renormalizes the energy scales of the system such that the transition can be reached for parameters largely deviated from the undriven critical points. In contrast we show that the driving plays an essential role in the conventional and topological QPTs under study, because it induces novel quantum phases that exist as a consequence of dynamical stabilization [45, 66, 92].

1.4. Structure

The thesis is divided into six chapters. The introduction in this chapter 1 contains the motivation and the outline of the thesis. The driven version of the Dicke model is discussed in chapter 2. The Dicke model is a paradigmatic model of criticality in quantum optics. However, a "no-go theorem" forbids the occurrence of the superradiant QPT in cavity QED. To circumvent such a constraint on criticality, a study of the weak driving regime is necessary. The recent experimental realization of the superradiant QPT in a Bose Einstein condensate in an optical cavity motivates the discussion of the strong driving limit. In chapter 3, the periodically driven Lipkin-Meshkov-Glick (LMG) model is investigated, which is closely related to the Dicke model, but more tractable numerically. To understand the character of multistability for a finite size of the system, the quantum evolution of a wave packet initially localized at a minimum of the quasienergy landscape is studied. Furthermore, both the continuous and the stroboscopic quantum evolution are discussed. After the description of the intriguing aspects of systems with spatial dimension $d = 0$, nonequilibrium criticality in the one-dimensional Ising model is explored in chapter 4. In contrast to the zero-dimensional models, the Ising model is characterized by a set of infinite collective excitations, and destructive interference in time plays an important role. Additionally, the cycle-averaged magnetization and total energy are calculated, which lead to a discussion about the order of the nonequilibrium QPT in terms of nonanalyticities of the derivatives of the cycle-averaged energy. After the investigation of conventional ac-driven QPTs, the nonequilibrium TQPT in the driven Wen-plaquette model is described in chapter 5. A set of highly nonlocal spin-duality transformations allows a description of the Wen model in terms of the Ising model physics. The topological character of the Wen model requires a description of the QPT in terms of nonlocal order parameters, which correspond to

long-range correlation functions for a driven Ising model in the dual picture. Furthermore, the Floquet-Chern numbers which characterize the different topological phases are calculated. In chapter 6, a conclusion and outlook is given.

2. AC-driven Quantum Phase Transitions in the Dicke model

The Dicke model (DM) is a paradigm of collective behavior in quantum mechanics [21] and describes the interaction of N two-level atoms with a single-mode bosonic field. The DM undergoes a quantum phase transition (QPT) at a critical atom-field coupling, the same order of magnitude as the atomic level splitting [22, 23]. Whereas in cavity QED it is forbidden by a "no-go theorem" [37, 38], the superradiant QPT has recently been realized experimentally in a simulation of the DM with a Bose-Einstein condensate in an optical cavity [24], with a subsequent observation of spontaneous symmetry breaking by adiabatically crossing the critical point [26].

In this chapter we study a driven version of the DM in which we assume a time-dependent atom-field coupling. In comparison to previous works which consider non-adiabatic modulation of a single two-level system [39, 40, 41, 42] or an N-atom system under adiabatic change of the parameters [14, 17], here we address the fundamental issue of the influence of non-adiabatic modulation on QPTs.

In the limit of weak driving strength we show that our driven DM exhibits a set of new nonequilibrium normal-superradiant QPTs (QPT sidebands) when the driving is near resonance with the excitation energies of the undriven system. The QPTs are of second order and similar in kind to the original Hepp-Lieb transition [22]. We show that these nonequilibrium QPTs are not forbidden by the no-go theorem, thus bringing the otherwise-forbidden Dicke-type QPT in the realm of observability in cavity and circuit QED setups. Our analysis also allows us to go beyond this perturbative regime and investigate the limit of strong driving. In this regime we show that, in comparison with previous proposals for driven QPTs [18, 19, 20], the nature of criticality changes dramatically. We find a rich nonequilibrium phase diagram replete with a host of macroscopically-distinct meta-stable phases and a nonequilibrium first-order QPT with no analogues in the static case [43].

2.1. The driven Dicke model

Following Dicke [21], we describe an ensemble of N identical, distinguishable two-level atoms (level splitting ω_0) by means of collective operators $\hat{J}_\alpha = \frac{1}{2}\sum_{i=1}^{N}\sigma_i^\alpha$, where σ_i^α are the Pauli matrices with $\alpha \in \{x, y, z\}$. These operators satisfy the

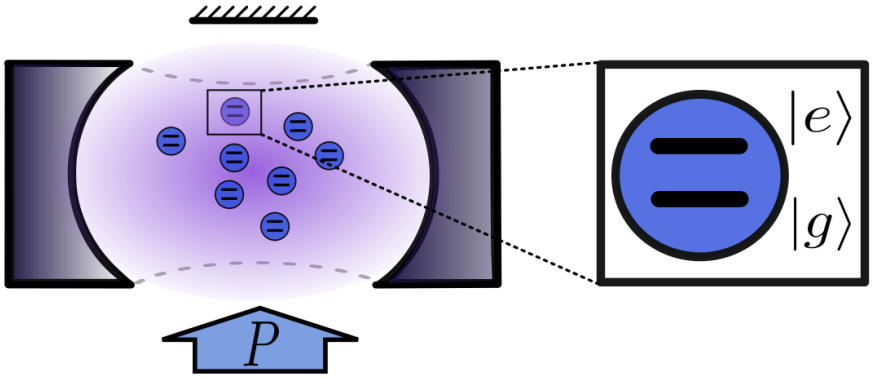

Figure 2.1.: Ensemble of two-level atoms interacting collectively with a single-mode cavity field. The ground state of the atom is denoted by $|g\rangle$ and the excited state by $|e\rangle$.

$SU(2)$ algebra $\left[\hat{J}_\alpha, \hat{J}_\beta\right] = i\epsilon_{\alpha\beta\gamma}\hat{J}_\gamma$. The atomic ensemble interacts with a bosonic mode of frequency ω via a dipole interaction. With the atom-field coupling strength time-dependent, we obtain the *driven* DM:

$$\hat{H}(t) = \omega\hat{a}^\dagger\hat{a} + \omega_0\hat{J}_z + \frac{\lambda(t)}{\sqrt{N}}(\hat{a}^\dagger + \hat{a})\left(\hat{J}_+ + \hat{J}_-\right), \tag{2.1}$$

and in the following we shall consider a monochromatic modulation with a static contribution: $\lambda(t) = \lambda_0 + \lambda_1 \cos\Omega t$. In this chapter we consider Dicke states i.e., the whole analysis is reduced to the Hilbert subspace characterized by a maximal total angular momentum $j = N/2$ [23].

Even under the effect of driving, the Hamiltonian Eq. (2.1) has a conserved parity

$$\hat{\Pi} = \exp(\mathrm{i}\pi(\hat{a}^\dagger\hat{a} + \hat{J}_z + j\hat{\mathbb{1}})), \tag{2.2}$$

such that $[\hat{H}(t), \hat{\Pi}] = 0$. Figure 2.1 depicts a typical cavity QED setup, where a cloud of two-level systems interacts with a single-mode cavity field via dipole interaction.

2.1.1. The superradiant QPT in the undriven Dicke model

The Dicke model was originally conceived to describe light-matter interactions in equilibrium. In the absence of driving, i.e., when $\lambda_1 = 0$, the Dicke model exhibits a second-order QPT at the critical coupling $\lambda_0^c = \sqrt{\omega\omega_0}/2$ from the normal phase ($\lambda_0 < \lambda_0^c$)—which is characterized by microscopic excitations of the system, to a superradiant phase ($\lambda_0 > \lambda_0^c$) characterized by macroscopic occupations of the bosonic

mode as well as the atomic ensemble. In the case of a set of N incoherent atomic emitters, the intensity of the emitted light is expected to be proportional to N, in contrast, when the system enters into the superradiant phase, the intensity of the emitted light scales as N^2, which is a signature of collective coherent motion of the light-matter system [22, 23].

In the thermodynamic limit $N \to \infty$ the system is characterized by atom-field collective excitations commonly referred to as the bosonic and the atomic branches with energies ε_+ and ε_- respectively [23]. When the system approaches the critical coupling $\lambda_0 \to \lambda_0^c$ there is a softening of the atomic branch, i.e., $\varepsilon_- \to 0$. Additionally, both the scaled mean photon number as well as the mean energy per atom in the ground state exhibit nonanalyticities in the second derivative after the atom-field coupling λ_0, which is a hallmark of a second-order QPT.

Despite the appealing nature of the Dicke model to describe light-matter interactions and criticality in quantum optics, there is an assumption that is only justified in the weak coupling limit. To derive the Dicke model, one usually neglects the diamagnetic term of the light-matter interaction. This term is directly proportional to the square of the atom-field coupling and inversely proportional to the atomic level splitting ω_0. Rather recently, it has been proven a "no-go theorem" that forbids the superradiant QPT to occur in cavity QED [37, 38]. Essentially, the argument is based on the fact that the diamagnetic term prevents the existence of gapless excitations above the ground state. Therefore, in the thermodynamic limit the singularities in the observables are avoided, as there is not crossing between the first excited state and the ground state [3]. In contrast to the weak atom-field coupling regime—where the system is in the unexcited phase, when the system is close to the critical coupling, the diamagnetic term cannot be safely neglected.

Our approach is this chapter is to overcome the "no-go theorem" by considering the effect of a nonadiabatic external control on the dynamics of the system. In this case, however, the system is characterized by non-stationary states and the notion of quantum phases that one has in equilibrium should be extended to nonequilibrium conditions.

2.1.2. Effective bosonized Hamiltonian for the symmetric phase

One can think about the superradiant QPT in terms of stability, i.e., when the normal phase is unstable, the system exhibits a transition into a bistable configuration, which corresponds to the superradiant phase. Such a description becomes clearer in a mean-field description, from this perspective, the energy landscape has a single minimum in the normal phase, and, at the critical coupling λ_0^c, the system experiences a bifurcation [23]. Motivated by the last discussion, let us begin

our analysis by investigating the stability of the normal phase under driving. To this end, we construct a normal-phase effective Hamiltonian in the same way as in Ref. [23] for the undriven case: we make a Holstein-Primakoff representation of the angular momentum algebra [44] in terms of bosonic operators $\hat{b}, \hat{b}^\dagger$

$$\begin{aligned} \hat{J}_z &= \hat{b}^\dagger \hat{b} - \frac{N}{2}\hat{\mathbb{1}}, \\ \hat{J}_+ &= \hat{b}^\dagger \sqrt{N - \hat{b}^\dagger \hat{b}}, \\ \hat{J}_- &= \sqrt{N - b^\dagger b}\ \hat{b}, \end{aligned} \tag{2.3}$$

and take the thermodynamic limit, assuming that $\hat{b}/N \to 0$. The result is the driven normal-phase Hamiltonian

$$\hat{H}_{\mathrm{S}}(t) = \omega \hat{a}^\dagger \hat{a} + \omega_0 \hat{b}^\dagger \hat{b} + \lambda(t)(\hat{a}^\dagger + \hat{a})(\hat{b}^\dagger + \hat{b}) - \frac{N\omega_0}{2}\hat{\mathbb{1}}, \tag{2.4}$$

which describes fluctuations about the vacuum cavity state and an unexcited atomic ensemble, i.e., the symmetric phase. Let us now introduce the quadrature operators

$$\hat{x} = \frac{\hat{a}^\dagger + \hat{a}}{\sqrt{2\omega}}, \quad \hat{p}_x = \mathrm{i}\sqrt{\frac{\omega}{2}}(\hat{a}^\dagger - \hat{a}), \tag{2.5}$$

and

$$\hat{y} = \frac{\hat{b}^\dagger + \hat{b}}{\sqrt{2\omega_0}}, \quad \hat{p}_y = \mathrm{i}\sqrt{\frac{\omega}{2}}(\hat{b}^\dagger - \hat{b}), \tag{2.6}$$

where $(\hat{x}, \hat{p}_x)$ are quadratures of the cavity field, and $(\hat{y}, \hat{p}_y)$ the corresponding quadratures of the atomic ensemble. In terms of the abstract coordinate representation Eqs. (2.5) and (2.6), the Hamiltonian Eq. (2.4) can be written as

$$\hat{H}_{\mathrm{S}}(t) = \frac{1}{2}(\hat{p}_x^2 + \omega^2 \hat{x}^2 + \hat{p}_y^2 + \omega_0^2 \hat{y}^2) + 2\sqrt{\omega\omega_0}\hat{x}\hat{y} - \frac{1}{2}\left(\omega + \omega_0 + N\omega_0\right)\hat{\mathbb{1}}. \tag{2.7}$$

In the Heisenberg picture, the equations of motion for the normal coordinate operators of this model, $\hat{q}_\pm(t) = (\hat{x}(t) \pm \hat{y}(t))/\sqrt{2}$, read [45]

$$\ddot{\hat{q}}_\pm(t) + \left[\varepsilon_\pm^2 \pm 2\omega\lambda_1 \cos\Omega t\right]\hat{q}_\pm(t) = 0, \tag{2.8}$$

with $\varepsilon_\pm = \sqrt{\omega^2 \pm 2\lambda_0\omega}$, the excitation energies of the undriven normal phase and where we have set $\omega_0 = \omega$ for simplicity. Equation (2.8) represents two uncoupled Mathieu equations [46]. In classical dynamics, the Mathieu equation exhibits the phenomenon of parametric resonance and has stable and unstable solutions whose location is given by the Arnold tongues [46]. The manifestation of parametric resonance in the quantum regime has also been studied in Ref. [47].

2.1.3. Resonance conditions

Now let us discuss the stability of the normal phase based on the concept of parametric resonance. In our case, when both normal modes $\hat{q}_\pm$ are stable, Hamiltonian $\hat{H}_{\rm S}(t)$ permits bound solutions, localized around unoccupied field and atomic modes. Either scaled field occupation, $2\langle\hat{a}^\dagger\hat{a}\rangle/N$, or scaled atomic occupation, $2\langle\hat{b}^\dagger\hat{b}\rangle/N = 2\langle\hat{J}_z\rangle/N + 1$, may be taken as the order parameter for this system, and here they are both zero ($N \to \infty$). When unstable, $\hat{H}_{\rm S}(t)$ possesses only unbounded solutions and ceases to be a valid approximation to the full Hamiltonian (admitting the possibility that the order-parameter becomes finite).

Figure 2.2 depicts these stable zones as a function of the static parameters λ_0 and ω — the colored zones correspond to stability, white zones, instability. Without driving, $\lambda_1 = 0$, the stability-instability transition corresponds to the standard DM QPT along the line $\lambda_0 = \omega/2$ (on resonance). Increasing the driving strength λ_1 has two effects: it leads to a shift of this critical line—as a consequence of parametric stabilization [46]—and more importantly, it opens up new zones of instability in the normal phase. The precise locations of these zones can be obtained from the known behavior of the Arnold tongues [46]. When they first appear, these zones are located around the resonance between driving frequency and the undriven excitation energies: $2\varepsilon_\pm = m\Omega$ with integer $m \geq 0$. A similar instability for $m = 1$ was briefly discussed in the dispersive limit $\omega \gg \omega_0$ in Ref. [49]. For sufficiently small driving, the width of the mth unstable zone scales like $(2/\Omega)^{2m-1}(\lambda_1\,\omega)^m$ [46, 48]. For large λ_1 the new instability zones dominate the parameter space [Fig. 2.2(b)]. Just as the change in stability of the undriven normal-phase effective Hamiltonian indicates the occurrence of a QPT, we interpret the change in the stability of $\hat{H}_{\rm S}(t)$ as ushering the occurrence of a nonequilibrium QPT.

2.2. The rotating wave approximation and the effective Hamiltonian approach

To obtain more information about the nonequilibrium QPTs and the unstable zones of Fig. 2.2, we employ Floquet theory [50] and make use of the rotating wave approximation (RWA), similar to that found in Refs. [51, 52]. Motivated by the fact that for small static coupling λ_0, the mth instability zone arises close to $\omega_0 = \omega \approx m\Omega/2$, we perform a canonical transformation of Eq. (2.1), into the rotating frame

$$\hat{U}_m(t) = \exp\left[-\mathrm{i}\Upsilon(t)(\hat{a}^\dagger + \hat{a})\hat{J}_x\right]\exp\left[-\mathrm{i}\theta_m(t)(\hat{a}^\dagger\hat{a} + \hat{J}_z)\right], \tag{2.9}$$

where $\theta_m(t) = \frac{m\Omega t}{2}$ and $\Upsilon(t) = \frac{2}{\sqrt{N}}(\frac{\lambda_1}{\Omega})\sin\Omega t$. In the rotating frame the dynamics is governed by the Hamiltonian $\hat{H}_m(t) = \hat{U}_m^\dagger(t)\hat{\mathcal{H}}\hat{U}_m(t)$, where $\hat{\mathcal{H}} = \hat{H}(t) - \mathrm{i}\frac{\partial}{\partial t}$ is

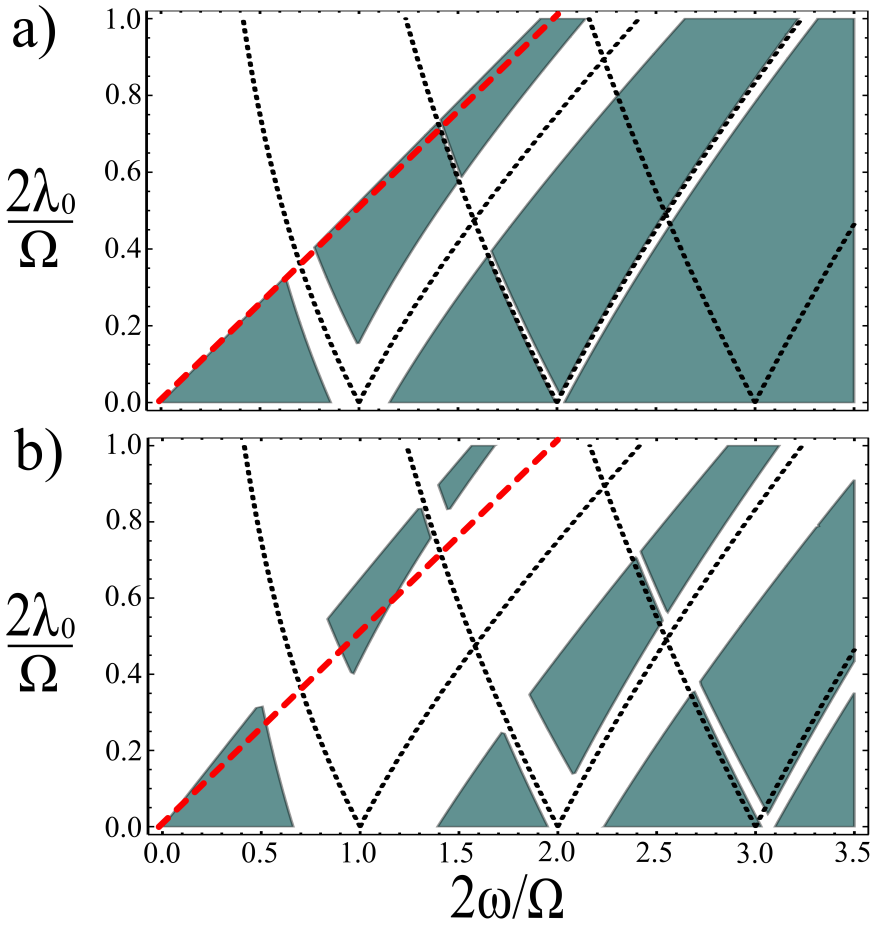

Figure 2.2.: Stability diagram of the nonequilibrium normal phase on resonance $\omega = \omega_0$ for (a) weak driving, $\lambda_1/\Omega = 0.15$, and (b) strong driving, $\lambda_1/\Omega = 0.4$. The colored zones correspond to stability, white zones, instability. In the undriven case, the stable and unstable zones are separated by the line $\lambda_0^c = \omega/2$ on resonance (dotted red line). For weak driving instability zones open up around the resonance conditions $2\varepsilon_\pm = m\Omega$ for $m = 1, 2, 3$ (dotted black lines), which grow and begin to dominate for large driving.

the Floquet Hamiltonian [50]. The explicit form of the Hamiltonian in the rotating frame is

$$\begin{aligned}\hat{H}_m(t) &= \delta^{(m)}\hat{a}^\dagger\hat{a} + \left\{\omega_0 \cos\left[\Upsilon(t)\left(\hat{a}^\dagger e^{\mathrm{i}\theta_m(t)} + \hat{a}e^{-\mathrm{i}\theta_m(t)}\right)\right] - m\Omega/2\right\}\hat{J}_z \\ &+\frac{\lambda_0}{\sqrt{N}}\left(\hat{a}^\dagger e^{\mathrm{i}\theta_m(t)} + \hat{a}e^{-\mathrm{i}\theta_m(t)}\right)\left(\hat{J}_+ e^{\mathrm{i}\theta_m(t)} + \hat{J}_- e^{-\mathrm{i}\theta_m(t)}\right) \\ &-\mathrm{i}\frac{\omega}{2}\Upsilon(t)\left(\hat{a}^\dagger e^{\mathrm{i}\theta_m(t)} - \hat{a}e^{-\mathrm{i}\theta_m(t)}\right)\left(\hat{J}_+ e^{\mathrm{i}\theta_m(t)} + \hat{J}_- e^{-\mathrm{i}\theta_m(t)}\right) \\ &+\frac{\omega}{4}\left[\Upsilon(t)\left(\hat{J}_+ e^{\mathrm{i}\theta_m(t)} + \hat{J}_- e^{-\mathrm{i}\theta_m(t)}\right)\right]^2 \\ &-\mathrm{i}\frac{\omega_0}{2}\sin\left[\Upsilon(t)\left(\hat{a}^\dagger e^{\mathrm{i}\theta_m(t)} + \hat{a}e^{-\mathrm{i}\theta_m(t)}\right)\right]\left(\hat{J}_+ e^{\mathrm{i}\theta_m(t)} - \hat{J}_- e^{-\mathrm{i}\theta_m(t)}\right) \quad (2.10)\end{aligned}$$

where $\delta^{(m)} = \omega - m\Omega/2$. We then rewrite this equation using the operator identities

$$\begin{aligned}\cos[\hat{\mathcal{O}}_m(t)\sin\Omega t] &= \mathcal{J}_0[\hat{\mathcal{O}}_m(t)] + 2\sum_{n=1}^{\infty}\mathcal{J}_{2n}[\hat{\mathcal{O}}_m(t)]\cos(2n\Omega t), \\ \sin[\hat{\mathcal{O}}_m(t)\sin\Omega t] &= 2\sum_{n=0}^{\infty}\mathcal{J}_{2n+1}[\hat{\mathcal{O}}_m(t)]\sin[(2n+1)\Omega t], \end{aligned} \quad (2.11)$$

where $\mathcal{J}_m[z]$ denotes the Bessel function of integer order m [48], and the time-dependent operator argument is given by $\hat{\mathcal{O}}_m(t) = \frac{2}{\sqrt{N}}\left(\frac{\lambda_1}{\Omega}\right)\left(\hat{a}^\dagger e^{\mathrm{i}\theta_m(t)} + \hat{a}e^{-\mathrm{i}\theta_m(t)}\right)$. Considering the power series expansion of the Bessel functions, it is possible to write the Hamiltonian Eq. (2.10) in the general form

$$\hat{H}_m(t) = \sum_{n=-\infty}^{\infty}\hat{h}_n^{(m)}e^{\mathrm{i}n\Omega t}. \quad (2.12)$$

In the rotating frame we are able to explicitly describe multiphoton processes that arise as a consequence of the interplay between the quantum cavity field and the classical external driving [50]. To perform the RWA [42, 51, 52], we neglect the contributions due to virtual processes that occur faster than the characteristic time scales of the system (see Appendix A). Therefore, we consider only the zero frequency component $\hat{H}_m(t) \approx \hat{h}_0^{(m)}$ of the Hamiltonian Eq. (2.12). For example, in the case of the $m = 0$ resonance, a general condition of RWA validity in the strong driving regime should be satisfied for all $|n| > 0$: $\lambda_0,\ \omega_0\|\mathcal{J}_n[\hat{\mathcal{O}}_m(0)]\|,\ \omega\|\mathcal{J}_n[\hat{\mathcal{O}}_m(0)]\| \ll \Omega$, where $\|\cdot\|$ is an operator norm. In contrast, in the weak driving regime $\lambda_1/\Omega \ll 1$, we require $\lambda_0,\ \omega,\ \omega_0 \ll \Omega$. The norm of the Bessel function is always bounded, therefore we can summarize the conditions for weak and strong driving as $\lambda_0,\ \omega,\ \omega_0 \ll \Omega$.

2.2.1. Sidebands QPT

We focus here on the weak driving regime, and obtain the effective Hamiltonian around a quantum resonance for $m = 0, 1, 2$.

In the weak driving regime, the approximation to Hamiltonian $\hat{h}_0^{(0)}$ up to second order in λ_1/Ω is

$$\begin{aligned}\hat{h}_0^{(0)} &\approx \delta^{(0)}\hat{a}^\dagger\hat{a} + \delta_0^{(0)}\hat{J}_z + \frac{\lambda_0}{\sqrt{N}}(\hat{a}^\dagger + \hat{a})\left(\hat{J}_+ + \hat{J}_-\right) \\ &\quad -\frac{\omega_0}{N}\left(\frac{\lambda_1}{\Omega}\right)^2(\hat{a}^\dagger + \hat{a})^2\hat{J}_z + 2\omega\left(\frac{\lambda_1}{\Omega}\right)^2\frac{\hat{J}_x^2}{N}. \end{aligned} \tag{2.13}$$

Therefore we obtain a model similar to the undriven DM, that can be analyzed in the same way [23]. This analysis reveals a second-order QPT along the critical line $\lambda_0 = \omega/2 + \omega(\lambda_1/\Omega)^2$ ($\omega = \omega_0$), which gives the first contribution to the shift of the DM phase boundary observed in Fig.2.2. For the higher resonances, $m > 0$, exact expressions for $\hat{h}_0^{(m)}$ are difficult to obtain. However, it is possible to write down explicit expansions up to any finite order in λ_1/Ω. To second order, the $m = 1$ effective Hamiltonian reads

$$\begin{aligned}\hat{h}_0^{(1)} &= \delta^{(1)}\hat{a}^\dagger\hat{a} + \delta_0^{(1)}\hat{J}_z \\ &\quad +\frac{\lambda_0}{\sqrt{N}}\left(\hat{a}^\dagger\hat{J}_- + \hat{a}\hat{J}_+\right) + \frac{\lambda_1}{2\sqrt{N}}\left(\hat{a}^\dagger\hat{J}_+ + \hat{a}\hat{J}_-\right) \\ &\quad -2\omega_0\left(\frac{\lambda_1}{\Omega}\right)^2\hat{a}^\dagger\hat{a}\frac{\hat{J}_z}{N} + \omega\left(\frac{\lambda_1}{\Omega}\right)^2\frac{\hat{J}_-\hat{J}_+}{N}. \end{aligned} \tag{2.14}$$

The region of validity of this Hamiltonian is $\omega \approx \omega_0$ and $\delta^{(1)},\ \delta_0^{(1)},\ \lambda_0,\ (\lambda_1/\Omega)^2 \ll \omega, \omega_0$. The first two lines of this Hamiltonian represent a model similar to the original Dicke model in which energy conserving and nonconserving parts of the interaction have independent coupling parameters (λ_0 and $\lambda_1/2$, respectively) similar to [53]. At second order in λ_1/Ω, new effective interactions arise: the terms on the third line of Eq. (2.14) can be interpreted as an effective dispersive atom-field interaction and a dipole-dipole interaction between the atoms. Analytically, this Hamiltonian may again be treated in the same way as the undriven DM, from which we observe a second-order superradiant transition occurring at the critical lines $\lambda_0 = -\lambda_1/2 + |\delta^{(1)} + \omega(\lambda_1/\Omega)^2|$, and similarly for the $m = 2$ case

$$\begin{aligned}\hat{h}_0^{(2)} &= \delta^{(2)}\hat{a}^\dagger\hat{a} + \delta_0^{(2)}\hat{J}_z + \frac{\lambda_0}{\sqrt{N}}\left(\hat{a}^\dagger\hat{J}_- + \hat{a}\hat{J}_+\right) \\ &\quad -2\omega_0\left(\frac{\lambda_1}{\Omega}\right)^2\hat{a}^\dagger\hat{a}\frac{\hat{J}_z}{N} + \omega\left(\frac{\lambda_1}{\Omega}\right)^2\frac{\hat{J}_-\hat{J}_+}{N} \\ &\quad +\frac{\omega_0}{2N}\left(\frac{\lambda_1}{\Omega}\right)^2[(\hat{a}^\dagger)^2 + \hat{a}^2]J_z - \frac{\omega}{4N}\left(\frac{\lambda_1}{\Omega}\right)^2(\hat{J}_+^2 + \hat{J}_-^2). \end{aligned} \tag{2.15}$$

A similar analysis for the $m = 2$ case yields a further second-order QPT along the lines at $\lambda_0 = \delta^{(2)} + \frac{\omega}{2}(\lambda_1/\Omega)^2$ and $\lambda_0 = -\delta^{(2)} - \frac{3\omega}{2}(\lambda_1/\Omega)^2$. This analysis can be repeated for the all values of m.

To study the quantum criticality described by the effective Hamiltonian $\hat{h}_0^{(m)}$ we consider the Holstein-Primakoff representation of the angular momentum algebra Eq. (2.3). In this representation, the driven Dicke Hamiltonian is written in terms of two bosonic modes $\hat{a}$ and $\hat{b}$. We introduce macroscopic displacements $X\sqrt{N/2}$, $Y\sqrt{N/2}$ of order $\sqrt{N}$ for the bosonic $\hat{a}$ and for the atomic $\hat{b}$ modes, respectively. These macroscopic displacements are defined by

$$\hat{a} = \hat{c} \pm X\sqrt{\frac{N}{2}}\hat{\mathbb{1}}, \qquad \hat{b} = \hat{d} \mp Y\sqrt{\frac{N}{2}}\hat{\mathbb{1}}. \tag{2.16}$$

In order to describe the QPT, we derive effective quadratic bosonic Hamiltonians for both the normal phase and the superradiant phase [23]. In the thermodynamic limit $N \to \infty$, we perform a series expansion of the Hamiltonian $\hat{h}_0^{(m)}$ in powers of $\sqrt{N/2}$

$$\hat{h}_0^{(m)} \approx \hat{h}_Q^{(m)}(\hat{c}, \hat{d}, \hat{c}^\dagger, \hat{d}^\dagger) + \sqrt{\frac{N}{2}}\ \hat{h}_L^{(m)}(\hat{c}, \hat{d}, \hat{c}^\dagger, \hat{d}^\dagger) + \frac{N}{2}\ E_G^{(m)}(X, Y)\hat{\mathbb{1}}, \tag{2.17}$$

where $\hat{h}_Q^{(m)}$ is the desired effective quadratic bosonic Hamiltonian (depending on the choice of the macroscopic displacements Eq. (2.16)), $\hat{h}_L^{(m)}$ contains linear bosonic terms, and $E_G^{(m)}(X, Y)$ is the lowest quasienergy (LQE). In this thesis, we consider an alternative way to describe the quantum phases of the system based on the description of the stable energy configurations of the LQE landscape $E_G^{(m)}(X, Y)$. Such a geometrical description contains all the important information, because the linear term $\hat{h}_L^{(m)}$ of Hamiltonian expansion Eq. (2.17) vanishes for macroscopic displacements located at a critical point of the LQE, as the coefficients of the expansion are proportional to the first derivatives of $E_G^{(m)}(X, Y)$ after the displacements X and Y. Correspondingly, the quadratic term $\hat{h}_Q^{(m)}$ contains the geometric information of the principal curvatures in the neighborhood of a minimum as it contains second derivatives of $E_G^{(m)}(X, Y)$ after the macroscopic displacements. Interestingly, such principal curvatures are nothing but the energies of collective light-matter excitations characterizing the QPT. Therefore, when a stable configuration of the LQE landscape exhibits a transition into a saddle point, there is a softening of a collective excitation, that is related—from the geometrical point of view, to an infinite curvature radius in the neighborhood of the critical point.

For small driving, thus, Fig. 2.2 shows that the original DM QPT is joined by a set of new nonequilibrium *QPT sidebands*, the visible number of which (i.e. have significant width) increases with increasing driving strength. Each of these nonequilibrium QPTs is similar to the original transition in many respects; the transitions

are of the second-order, mean-field type, with the same critical exponents as in undriven DM [23].

2.2.2. Circumvention of the "no-go theorem" via side-bands QPT

One of the main consequences of the sidebands QPT consists in the fact, that a modulation of the coupling strength allows to effectively realize the Dicke QPT in a non-equilibrium setting, which is not forbidden by the no-go theorem. An important difference from superradiance in equilibrium setups is that, whereas the original DM QPT occurs for a static coupling $\lambda_0 \sim \omega/2$, the sideband QPTs occur for a coupling $\lambda_0 \sim \delta^{(m)} \ll \omega, \omega_0$ with the driving strength also of the same magnitude. In contrast to the static case, since the detuning $\delta^{(m)}$ can be made arbitrarily small, the diamagnetic term $\hat{H}_{NG} = \alpha \frac{[\lambda(t)]^2}{\omega_0}(\hat{a}^\dagger + \hat{a})^2$ arising from the square of the vector potential can be neglected even for $\alpha > 1$. Therefore, the sideband QPTs are not prohibited by the no-go theorem [37, 38] and should thus be observable in e.g. cavity- and circuit- QED experiments. We remark that this is different from previous proposals, e.g. [54, 55], where the no-go theorem is overcome by considering effective degrees of freedom not bound by the Thomas-Reiche-Kuhn sum rule [37, 38].

2.3. The effective Hamiltonian for the $m = 0$ case

We focus here on a particular case that admits a complete analytical description both in the weak coupling as well as in the strong coupling limit. Therefore, in this section we address the expansion of the effective Hamiltonian $\hat{h}_0^{(m)}$.

The full fundamental $m = 0$ effective Hamiltonian derived with this approach reads:

$$\begin{aligned} \hat{h}_0^{(0)} &= \delta^{(0)}\hat{a}^\dagger\hat{a} + \delta_0^{(0)}\mathcal{J}_0\left(\frac{2\lambda_1}{\Omega\sqrt{N}}(\hat{a}^\dagger + \hat{a})\right)\hat{J}_z \\ &\quad + \frac{\lambda_0}{\sqrt{N}}(\hat{a}^\dagger + \hat{a})\left(\hat{J}_+ + \hat{J}_-\right) + 2\omega\left(\frac{\lambda_1}{\Omega}\right)^2\frac{\hat{J}_x^2}{N}. \end{aligned} \tag{2.18}$$

In the thermodynamic limit, $N \to \infty$, we obtain a quadratic effective Hamiltonian with leading term $\frac{1}{2}NE_G^{(0)}(X, Y)$ with

$$\begin{aligned} E_G^{(0)}(X, Y) &= \omega X^2 + \omega_0(Y^2 - 1)\mathcal{J}_0\left(\frac{4\lambda_1 X}{\sqrt{2}\Omega}\right) \\ &\quad - \frac{4\lambda_0}{\sqrt{2}}XY\sqrt{2 - Y^2} + \omega\left(\frac{\lambda_1}{\Omega}\right)^2 Y^2(2 - Y^2). \end{aligned} \tag{2.19}$$

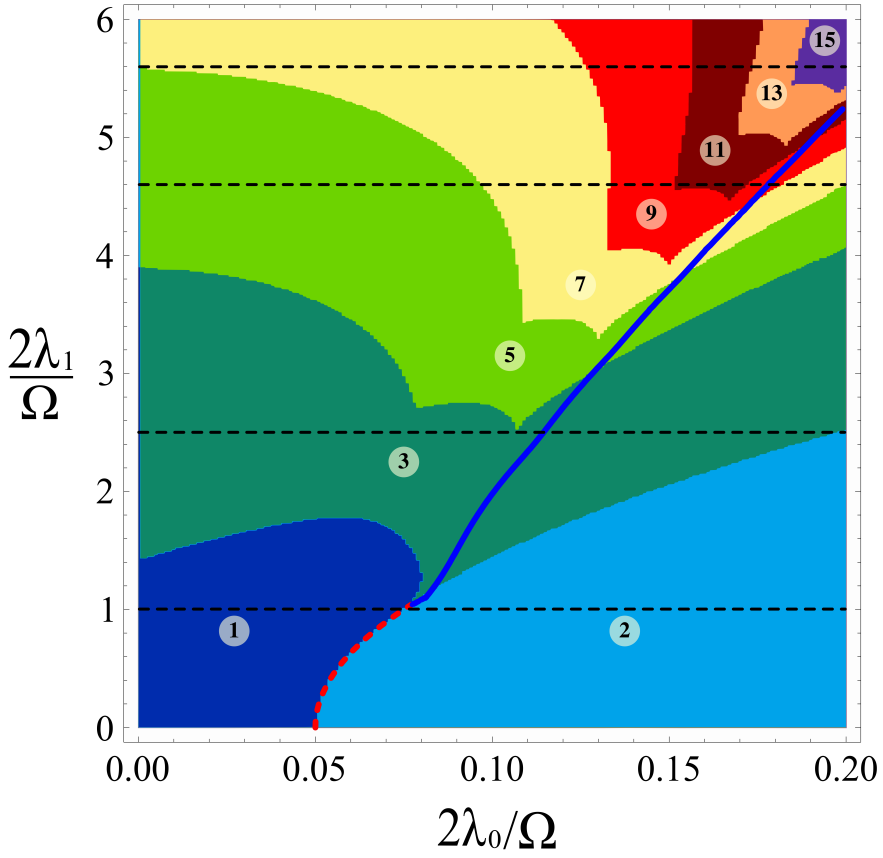

Figure 2.3.: Phase diagram as a function of static coupling (λ_0) and driving amplitude (λ_1) of effective Hamiltonian $\hat{h}_0^{(0)}$, which describes the driven DM near the $m = 0$ resonance. The labels indicate the number of local minima of the ground-state energy landscape $E_G^{(0)}$ in the corresponding zone. The normal phase is the region where there is just a single minimum ($X = Y = 0$). The superradiant phase is a region with two global minima (nonzero order parameter). The boundary between these two regions marks a second-order QPT (dotted red curve). Outside these regions, the energy surface has an odd number ≥ 3 of total minima, sometimes with a single global minima, sometimes with two. The boundary between these possibilities is a first-order QPT (solid blue line). The parameters are $\omega/\Omega = \omega_0/\Omega = 0.05$.

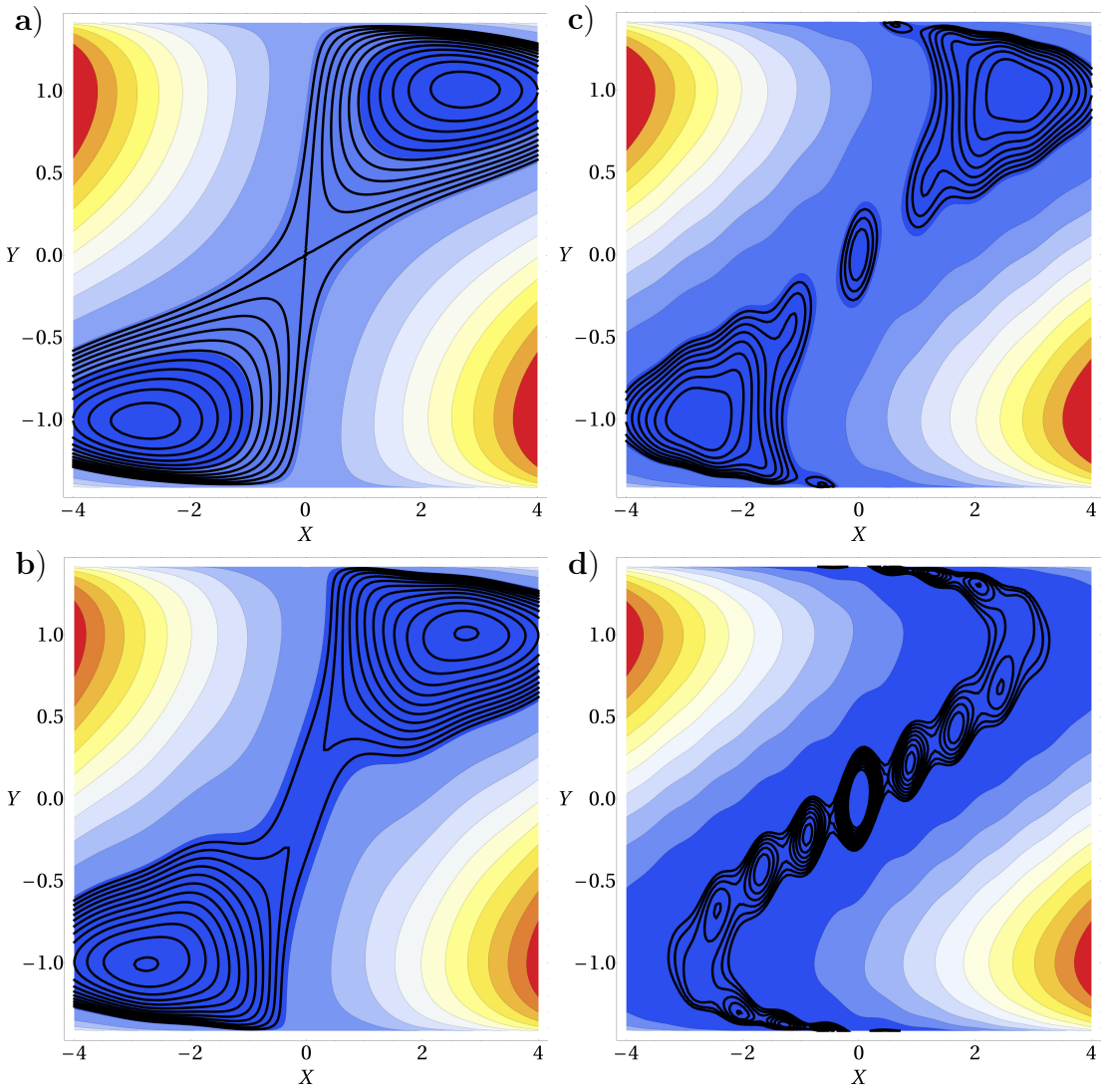

Figure 2.4.: Contours of the ground-state energy landscape $E_G^{(0)}(X, Y)$ for a fixed value of the static coupling ($2\lambda_0/\Omega = 0.195$) and increasing driving amplitudes (λ_1) represented by dashed straight lines in Fig. 2.3. The four panels show (a) the superradiant phase with two global minima ($\lambda_1 = 1.0$), (b) the emergence of a local minimum at the origin ($\lambda_1 = 2.5$), (c) multiple minima, but still two global minima ($\lambda_1 = 4.6$), and (d) a single global minima at the origin plus many further local minima ($\lambda_1 = 5.6$). Panels (c) and (d) are separated by the first-order phase transition. The parameters are $\omega/\Omega = \omega_0/\Omega = 0.05$.

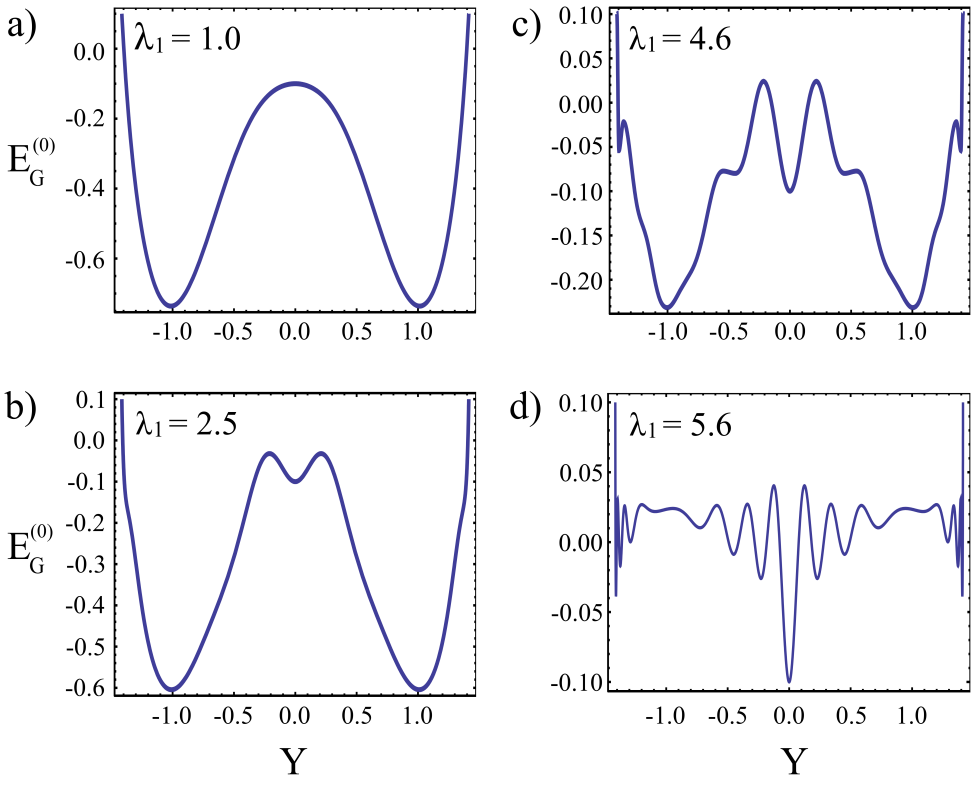

Figure 2.5.: Sections of the ground-state energy landscape $E_G^{(0)}(X, Y)$ for a fixed value of the static coupling ($2\lambda_0/\Omega = 0.195$) and increasing driving amplitudes (λ_1) represented by dashed straight lines in Fig. 2.3. This sections correspond to the function $E_G^{(0)}(X[Y], Y)$, where $X[Y]$ is a line in the order-parameter space crossing all the critical points of the ground-state energy. The four panels show (a) the superradiant phase with two global minima, (b) the emergence of a local minimum at the origin, (c) multiple minima, but still two global minima, and (d) a single global minima at the origin plus many further local minima. Panels (c) and (d) are separated by the first-order phase transition. The parameters are $\omega/\Omega = \omega_0/\Omega = 0.05$.

The global minima of $E_G^{(0)}(X,Y)$ give the ground-state energy of $\hat{h}_0^{(0)}$ and either X or Y may be taken as order-parameter. In the undriven case, the energy surface $E_G^{(0)}(X,Y)$ exhibits a bifurcation from single to double minima at the QPT. In the driven case, while retaining this bifurcation, $E_G^{(0)}(X,Y)$ also develops multiple additional minima, with the general trend that the number of minima increases with driving strength (see Fig. 2.3). Figure 2.4 shows a sequence of contours of the energy surface for increasing driving strength with static coupling $\lambda_0 > \lambda_0^c$, and Fig. 2.5 the corresponding sequence of cuts through the energy surface. As is clear from this sequence, at a certain value of λ_1, the potential switches from having two global minima to just a single one at the origin. At the boundary between these behaviors, the potential exhibits three global minima where normal-phase-like (with $X = Y = 0$) and superradiant-like (with $|X|, |Y| > 0$) solutions coexist. The system is therefore seen to exhibit a *first-order QPT* [4] as a function of driving strength, the location of which is shown in Fig. 2.3. Furthermore, we interpret the local minima of $E_G^{(0)}(X,Y)$ as metastable phases of $\hat{h}_0^{(0)}$. These metastable states are related to the phenomenon of parametric stabilization [46]. Since these are separated from the global minima by macroscopic displacements, we expect transitions between different metastable states to be suppressed, such that the corresponding values of the order-parameters are observable. This possibility is reinforced when one recalls that Eq. (2.19) actually describes the lowest *quasienergy*, which does not have the same thermodynamic significance as the lowest actual energy.

In summary, then, we have discussed a driven Dicke model through the use of a series of effective Hamiltonians obtained under the RWA. For weak driving the system exhibits a set of QPT side-bands for which the no-go theorem is circumvented. At strong driving the long-time dynamics of the system in the $m = 0$ resonance case is governed by the effective Hamiltonian $\hat{h}_0^{(0)}$, which exhibits rich structure with a first-order quantum phase transition and metastable states. We anticipate that the higher resonances show similar behavior. Our methodology should be generalizable to investigate similar regimes for other phase transitions.

2.4. Experimental realization

In this section we discuss feasible experimental realizations of our model. In the context of cavity QED, it has been shown experimentally that it is possible to produce a nonadiabatic optically-induced modulation of the atom-field coupling, while maintaining the atomic level splitting and the cavity mode frequency constant. This modulation of the light-matter coupling was obtained by means of a quantum well waveguide structure. Such a setup allows to switch on the light-matter interaction within less than one cycle of light [56]. Essentially, the two-level system corresponds to two subbands of the conduction band in the quantum well. In this scenario, the

strength of the atom-field coupling is proportional to the electron density in the lowest subband, therefore a modulation of the coupling is possible by varying the density in time. For low electron densities, the ratio between the coupling λ_0 and the atomic excitation energy ω_0 has order $\lambda_0/\omega_0 \approx 10^{-6}$ in this system, which is far too small to observe the undriven Dicke QPT. Furthermore, the no-go theorem should apply to this setup and, even if the coupling strength could be increased sufficiently, no QPT would be observed. This therefore promises to be a good candidate system where driving can induce our proposed QPT sidebands with critical behavior for weak coupling and weak driving $\lambda_0, \lambda_1 \ll \omega, \omega_0, \Omega$.

Another possible experimental realization of our model where circumvention of the no-go theorem might be critical is circuit QED. The implementation may consist of several Cooper pair quantum boxes embedded in a microwave resonator [39, 57].

Whilst circumvention of the no-go theorem is an important consequence of the QPT sidebands, they are interesting in their own right. Note that although the sideband Hamiltonians are similar to the original DM, there are differences (e.g. effective dipole-dipole interaction in Eqs. (2.13), (2.14) and (2.15)) and an experimental investigation of these effects would be interesting. In this context, it should be possible to realize these sidebands in a Bose-Einstein condensate coupled to an optical cavity setup as in the Esslinger experiment [24, 25, 26]. In this setup, the effective atom-field coupling could be controlled externally by varying the intensity of the pump laser as a function of time about a static value. The sideband QPTs should then be observable in the limit weak pump laser intensities and nonadiabatic modulation.

3. AC-driven Quantum Phase Transitions in the Lipkin-Meshkov-Glick Model

The Lipkin-Meshkov-Glick (LMG) model is nowdays a classic model of quantum criticality. Originally, the LMG model was proposed in 1965 in the context of nuclear physics to describe the dynamics of N interacting fermions distributed in two N-fold degenerate levels [58]. Despite of the original motivation of the Lipkin-Meshkov-Glick (LMG) model as a toy model to test approximation methods in manybody physics, currently it constitutes an active field of research and a natural scenario to study the relation between QPTs and spin squeezing [59] and quantum Fisher information as a resource for high-precision quantum estimation [60].

In this chapter we study the LMG model under monochromatic modulation of the interparticle interaction. Previous works have considered dynamical properties of the LMG model under an adiabatic change of parameters of the system across the quantum critical point [61], the effect of fast and slow quenches of the transverse field [62], and a driven uniaxial LMG model [63, 64, 65]. Here, we address the fundamental issue of driving-induced QPTs in the LMG model.

By using an external driving, we show how one can dramatically change the original monostable-bistable transition in the undriven system to obtain a rich zoology of novel quantum phases that are absent in equilibrium. We show that for weak driving, the quasienergy landscape still resembles the original transition. Interestingly, however, when the driving amplitude increases, an enormous number of stable configurations appear, which correspond to local minima of the quasienergy landscape [66]. This gives rise to a novel route of experimental studies exploring the characteristics of criticality under nonequilibrium conditions.

3.1. The driven LMG model

The driven LMG model describes N interacting two-level systems in a transverse local field. The model Hamiltonian reads

$$\hat{H}(t) = -h\hat{J}_z - \frac{1}{N}\left(\gamma^x(t)\hat{J}_x^2 + \gamma^y\hat{J}_y^2\right), \tag{3.1}$$

where $\hat{J}_\alpha = \frac{1}{2}\sum_{i=1}^{N}\sigma_i^\alpha$ denote collective angular momentum operators and σ_i^α are the Pauli matrices with $\alpha \in \{x, y, z\}$. These operators satisfy the $SU(2)$ algebra $\left[\hat{J}_\alpha, \hat{J}_\beta\right] = i\epsilon_{\alpha\beta\gamma}\hat{J}_\gamma$. In the following we shall consider $h < 0$, and a monochromatic modulation of the interparticle interaction with a static contribution: $\gamma^x(t) = \gamma_0^x + \gamma_1^x \cos\Omega t$.

In this chapter we consider Dicke states i.e., the whole analysis is reduced to the Hilbert subspace characterized by a maximal total angular momentum $j = N/2$ [23]. Associated with the Hamiltonian Eq. (3.1) is a conserved parity

$$\hat{\Pi} = \exp(\mathrm{i}\pi(\hat{J}_z + j\hat{\mathbb{1}})), \tag{3.2}$$

such that $[\hat{H}(t), \hat{\Pi}] = 0$.

3.1.1. The QPT in the undriven LMG model

In the case of the undriven LMG model ($\gamma_1^x = 0$), an analytic study of the ground-state energy surface in the thermodynamic limit $N \to \infty$ leads to a phase diagram in the (γ_0^x, γ^y)-plane, which is divided into four regions depending on the geometry of the surface. As a consequence of the parity symmetry Eq. (3.2) of the LMG Hamiltonian, it is sufficient to consider the region with $|\gamma_0^x| < \gamma^y$. This analysis shows that in the region $|\gamma_0^x| < \gamma^y < -h$ the ground-state energy landscape has a single global minimum, whereas in the regions with $|\gamma_0^x| < -h < \gamma^y$ the surface has two global minima. By crossing the critical line $\gamma^y = -h$, the single global minimum splits into two global minima and the system exhibits a continuous transition from a symmetric state to a symmetry-broken state, i.e., a second-order QPT. Figure 3.1 depicts the phase diagram of the undriven LMG model.

A typical energy surface in zone I displays one minimum and one maximum, which signal the lower and upper edges of the spectrum. In zone II the energy surface has two absolute minima (corresponding to the broken-phase degenerate ground states), a saddle point, and one maximum (the upper spectrum edge). In zone III the energy surface has two absolute minima, two saddle points, and two absolute maxima corresponding to a degenerate upper state. Finally, in zone IV the surface contains two minima, two saddle points, a local maximum and an absolute maximum signaling the upper bound of the spectrum [67].

In the context of nuclear physics, the undriven version of the LMG model allows to describe a transition of the nucleus from a spherically symmetric to a non-spherically symmetric shape [58]. This transition can be understood as a continuous bifurcation in the ground-state energy per nucleon, where a single minimum (corresponding to the symmetric configuration) splits into two degenerate minima of the energy (corresponding to the nonsymmetric phase).

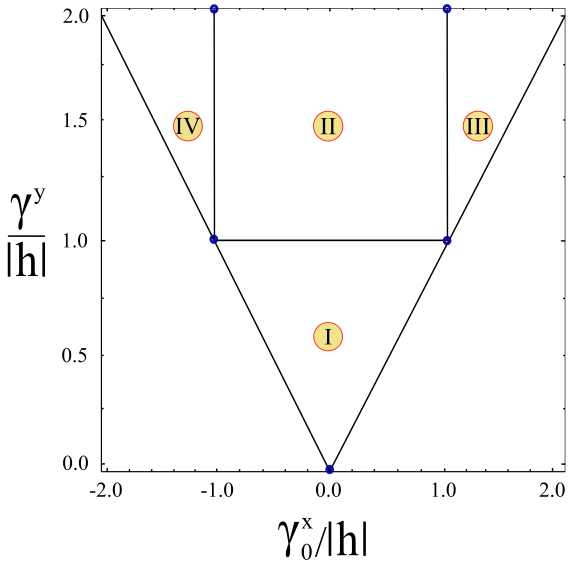

Figure 3.1.: Phase diagram of QPT in the undriven Lipkin-Meshkov-Glick model We consider $h/|h| = -1$. In zone I the energy surface has a maximum and a minimum, in zone II it has two minima, one saddle point and a maximum. Correspondingly, the surface has two maxima, two minima and two saddle points in zones III and IV.

3.1.2. Effective bosonized Hamiltonian for the symmetric phase

We begin our analysis by investigating the stability of the symmetric phase under the effect of an external driving. To this end, we construct a symmetric phase effective Hamiltonian in the same way as in Ref. [23]. We make a Holstein-Primakoff representation of the angular momentum algebra [44] in terms of bosonic operators $\hat{b}, \hat{b}^\dagger$ as in Eq. (2.3), and take the thermodynamic limit $N \to \infty$, assuming $\hat{b}/N \to 0$. The result is a bosonized Hamiltonian for the symmetric phase which reads

$$\hat{H}_{\rm S}(t) = -h\ \hat{b}^\dagger \hat{b} - \frac{1}{4}[\gamma^x(t)(\hat{b}^\dagger + \hat{b})^2 - \gamma^y(\hat{b}^\dagger - \hat{b})^2] + \frac{Nh}{2}\hat{\mathbb{1}}, \tag{3.3}$$

which resemble the bosonized Hamiltonian for the undriven LMG model [68, 69], in this case, however, the Hamiltonian is characterized by a time dependent squeezing parameter [59]. By introducing the coordinate operators

$$\hat{q} = \sqrt{-\frac{1}{2h}\left(\frac{h}{h+\gamma^y}\right)}(\hat{b}^\dagger + \hat{b}), \tag{3.4}$$

$$\hat{p} = \mathrm{i}\sqrt{-\frac{h}{2}\left(1+\frac{\gamma^y}{h}\right)}(\hat{b}^\dagger - \hat{b}), \tag{3.5}$$

we obtain the Hamiltonian of a parametrically-driven harmonic oscillator [46, 70, 71, 72, 73]

$$\hat{H}_{\rm S}(t) = \frac{\hat{p}^2}{2} + \frac{1}{2}\left(\epsilon^2 + h\gamma_1^x\left(1+\frac{\gamma^y}{h}\right)\cos\Omega t\right)\hat{q}^2 + \frac{Nh}{2}\hat{\mathbb{1}}, \tag{3.6}$$

where

$$\epsilon = -h\sqrt{\left(1+\frac{\gamma^y}{h}\right)\left(1+\frac{\gamma_0^x}{h}\right)} \tag{3.7}$$

is the characteristic energy scale of the system in the absence of driving ($\gamma_1^x = 0$). The undriven system exhibits a critical behavior which is related to softening of the collective excitation spectrum, i.e., when the system is close to the critical point ($\gamma^y \to -h$), the system exhibits a gapless excitation above the ground state ($\epsilon \to 0$). Therefore, in the region $|\gamma_0^x| < -h < \gamma^y$ the symmetric phase becomes unstable. Interestingly, in the driven system the situation can be highly nontrivial as a consequence of mechanisms such as parametric resonance and parametric stabilization, which are characteristic of the parametrically-driven harmonic oscillator [43, 46]. As a consequence, one can tune up conveniently the parameters close to resonance in order to manipulate the stability of the system, i.e., to produce a change of phase for parameters which are far away from the critical point of the undriven system.

3.1.3. Resonance conditions

In the thermodynamic limit, the undriven LMG model is characterized by a single collective excitation with energy ϵ. Under the effect of an external driving, the possibility of multiphotonic resonances arises [42, 50]. In the semiclassical theory of light-matter interaction, we can interpret a Floquet state as a light-matter quantum state containing a definite, though very large, number of photons [50]. Multiple transitions between quantum states of the system that are not directly coupled by the interaction can occur by means of intermediate states with a different number of photons [50, 52]. In particular, m-photon transitions occur when the condition

$$2\epsilon = m\Omega, \tag{3.8}$$

with integer m is satisfied. For a parametric oscillator with fundamental frequency ϵ, Eq. (3.8) is the usual resonance condition [46]. In Floquet theory, Eq. (3.8) implies the existence of a crossing between the energy levels when the energy spectrum of the undriven system is folded into the first Brillouin zone (FBZ) in quasienergy space [50]. We focus on the parameter regime $\delta^{(m)}, \gamma_0^x, \gamma^y \ll \Omega$, where the detuning $\delta^{(m)} = -h - \frac{m\Omega}{2}$ describes how far the system is from resonance, and the resonance condition Eq. (3.8) reads

$$-h \approx \frac{m\Omega}{2}. \tag{3.9}$$

Such a resonance condition will be used in the next section to perform a description of the system based on an effective time-independent Hamiltonian which is valid for parameters close to a multiphotonic resonance.

3.2. The rotating wave approximation and the effective Hamiltonian approach

As we are interested in the asymptotic quantum dynamics and the description of critical signatures, it is convenient to describe the dynamics of the system in a rotating frame. In the limit $\delta^{(m)}, \gamma_0^x, \gamma^y \ll \Omega$, it is possible to neglect the fast oscillations in the rotating frame, and a treatment of the system based on the description for time-independent systems is possible via an approximate effective Hamiltonian. Motivated by the m-photon resonance condition Eq. (3.9), we perform a study of the system based on the RWA [43, 52, 73]. Let us perform an unitary transformation of Hamiltonian Eq. (3.1) into a convenient rotating frame via the unitary operator

$$\hat{U}_m(t) = \exp\left[-\mathrm{i}\Theta(t)\hat{J}_x^2\right] \exp\left[-\mathrm{i}\theta_m(t)\hat{J}_z\right], \tag{3.10}$$

where $\Theta(t) = \frac{\gamma_1^x \sin\Omega t}{N\Omega}$ and $\theta_m(t) = \frac{m\Omega t}{2}$. In the rotating frame the dynamics is governed by the Hamiltonian $\hat{H}_m(t) = \hat{U}_m^\dagger(t)\hat{\mathcal{H}}\hat{U}_m(t)$, where $\hat{\mathcal{H}} = \hat{H}(t) - \mathrm{i}\frac{\partial}{\partial t}$ is the Floquet Hamiltonian [50]. The explicit form of this operator is given by

$$\begin{aligned}\hat{H}_m(t) &= -\frac{h}{2}\left\{[\hat{J}_z + \mathrm{i}\hat{\Lambda}_1^m(t)]\hat{\mathcal{O}}_1^m(t) + h.c\right\} - \frac{m\Omega}{2}\hat{J}_z \\ &+\frac{\gamma^y}{4N}\left\{[\hat{J}_z + \mathrm{i}\hat{\Lambda}_1^m(t)]^2\hat{\mathcal{O}}_2^m(t) + h.c\right\} \\ &-\frac{\gamma^y}{2N}\left\{\hat{J}_z^2 + [\hat{\Lambda}_1^m(t)]^2\right\} - \frac{\gamma_0^x}{N}[\hat{\Lambda}_2^m(t)]^2. \end{aligned} \tag{3.11}$$

We consider here the notation

$$\hat{\mathcal{O}}_1^m(t) = \sum_{l=-\infty}^{\infty} \mathcal{J}_l\left[\frac{\gamma_1^x}{N\Omega}(2\hat{\Lambda}_2^m(t) + 1)\right] e^{\mathrm{i}l\Omega t}, \tag{3.12}$$

$$\hat{\mathcal{O}}_2^m(t) = \sum_{l=-\infty}^{\infty} \mathcal{J}_l\left[\frac{4\gamma_1^x}{N\Omega}(\hat{\Lambda}_2^m(t) + 1)\right] e^{\mathrm{i}l\Omega t}, \tag{3.13}$$

where $\mathcal{J}_l(z)$ is the lth-order Bessel function [48], and

$$\hat{\Lambda}_1^m(t) = -\hat{J}_y\cos\theta_m(t) - \hat{J}_x\sin\theta_m(t), \tag{3.14}$$

$$\hat{\Lambda}_2^m(t) = \hat{J}_x\cos\theta_m(t) - \hat{J}_y\sin\theta_m(t). \tag{3.15}$$

The Hamiltonian Eq. (3.11) can be written in the form

$$\hat{H}_m(t) = \sum_{n=-\infty}^{\infty} \hat{h}_n^{(m)} e^{\mathrm{i}n\Omega t}. \tag{3.16}$$

In analogy with the standard RWA of quantum optics, we obtain an approximate Hamiltonian to describe the mth resonance by neglecting all the terms in $\hat{H}_m(t)$ with oscillatory time-dependence: $\hat{H}_m(t) \approx \hat{h}_0^{(m)}$, as we describe in Appendix A. The effective Hamiltonian $\hat{h}_0^{(m)}$ governs the dynamics in the rotating frame.

Next we perform a bosonization procedure of $\hat{h}_0^{(m)}$ via the Holstein-Primakoff representation Eq. (2.3). In the bosonized version, the effective Hamiltonian is written in terms of the bosonic mode $\hat{b}$. To investigate the criticality in the system we introduce a complex macroscopic displacement of order $\sqrt{N}$ for the bosonic operator as follows

$$\hat{b} = \hat{c} + \alpha\sqrt{N}\hat{\mathbb{1}}, \tag{3.17}$$

where $\alpha = (Q + \mathrm{i}P)$ (Q and P are dimensionless parameters) and $\hat{c}$ is a bosonic operator describing quantum fluctuations in the system. In the thermodynamic

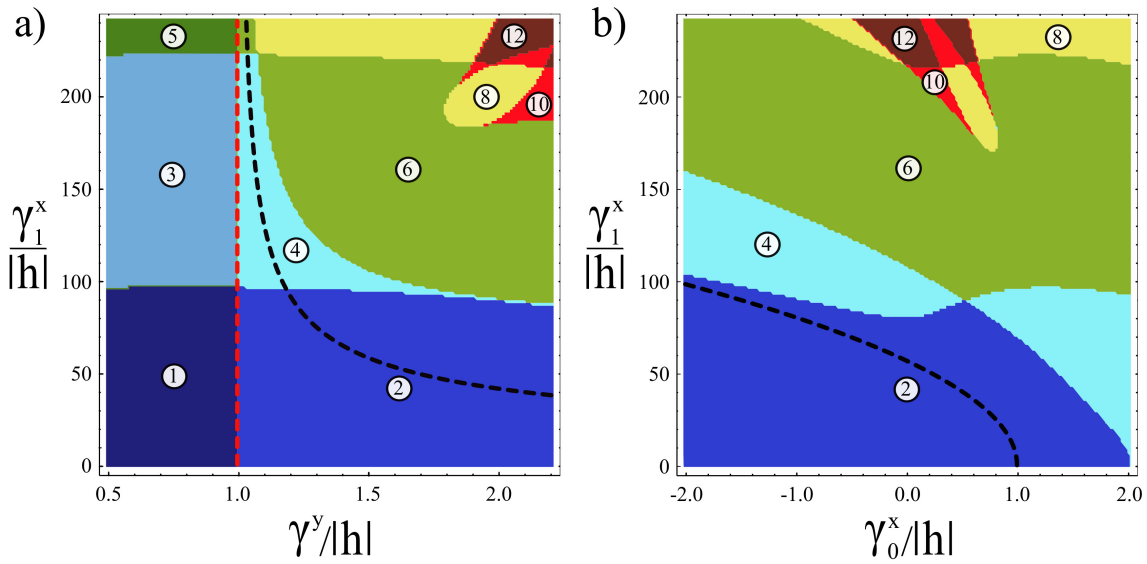

Figure 3.2.: Phase diagram of the nonequilibrium QPT in the Lipkin-Meshkov-Glick model. The number of local minima of the quasienergy surface $E_G^{(0)}(Q,P)$ in the colored zones is indicated by the labels. (a) Depicts the phase diagram as a function of γ^y and the driving amplitude γ_1^x for $\gamma_0^x/|h| = 0.5$, and (b) as a function of γ_0^x and γ_1^x for $\gamma^y/|h| = 2$. The dashed red line in (a) resembles the second-order QPT in the undriven LMG model that occurs at $\gamma^y/|h| = 1$, in the driven case, however, this line separates regions with even and odd number of minima. The dashed black lines in (a) and (b) depict the transition of the symmetric phase $(Q,P) = (0,0)$ from a saddle point to a local maximum, and correspond to the contour $\lambda_2 = 0$. We consider the parameters $\Omega/|h| = 40$ and $h/|h| = -1$.

limit $N \to \infty$, we perform a series expansion of the effective Hamiltonian in powers of $\sqrt{N}$ leading to

$$\hat{h}_0^{(m)} = \hat{h}_Q^{(m)}(\hat{c},\hat{c}^\dagger) + \sqrt{N}\,\hat{h}_L^{(m)}(\hat{c},\hat{c}^\dagger) + NE_G^{(m)}(Q,P)\hat{\mathbb{1}}, \tag{3.18}$$

where $\hat{h}_Q^{(m)}(\hat{c},\hat{c}^\dagger)$ is a quadratic bosonic Hamiltonian (depending on the choice of the macroscopic displacements Eq. (3.17)), $\hat{h}_L^{(m)}(\hat{c},\hat{c}^\dagger)$ contains linear bosonic terms, and $E_G^{(m)}(Q,P)$ is the LQE.

3.3. The effective Hamiltonian for the $m = 0$ case

Instead of performing an abstract general theory for the effective Hamiltonian related to general m-photon resonances, we focus here on an particular case that contains the more relevant information, i.e., we consider the case $m = 0$. In this case, the effective Hamiltonian reads

$$\begin{aligned}\hat{h}_0^{(0)} &= \left[-\frac{h}{2}(\hat{J}_z - \mathrm{i}\hat{J}_y)\mathcal{J}_0\left[\frac{\gamma_1^x}{N\Omega}(2\hat{J}_x+1)\right] + \frac{\gamma^y}{4N}(\hat{J}_z - \mathrm{i}\hat{J}_y)^2\mathcal{J}_0\left[\frac{4\gamma_1^x}{N\Omega}(\hat{J}_x+1)\right] + h.c\right] \\ &\quad -\frac{\gamma^y}{2N}(\hat{J}_z^2 + \hat{J}_y^2) - \frac{\gamma_0^x}{N}\hat{J}_x^2 \ . \end{aligned} \tag{3.19}$$

In this section, we focus on the thermodynamic limit $N \to \infty$, where we expand the Holstein-Primakoff representation Eq.(2.3) with respect to the complex macroscopic displacement Eq. (3.17). We next consider the scaled angular momentum operators

$$\hat{X}_1 = \frac{\hat{J}_x}{N} = Q\sqrt{1-|\alpha|^2}, \tag{3.20}$$

$$\hat{X}_2 = \frac{\hat{J}_y}{N} = P\sqrt{1-|\alpha|^2}, \tag{3.21}$$

$$\hat{X}_3 = \frac{\hat{J}_z}{N} = \left(|\alpha|^2 - \frac{1}{2}\right), \tag{3.22}$$

that satisfy $[\hat{X}_i, \hat{X}_j] = 0$ in the thermodynamic limit. Therefore, in this limit, the scaled angular momentum operators become c-number variables. Eqs. (3.20), (3.21) and (3.22) describe a mapping from the coordinates (Q, P) onto the Bloch sphere, because the norm of the vector $\boldsymbol{R} = (X_1, X_2, X_3)$ has constant length $\|\boldsymbol{R}\| = 1/2$. From Eqs. (3.20) and (3.21) it follows that $|\alpha|^2 \leq 1$. Furthermore, one can see from these relations that all points (Q, P) with $|\alpha|^2 = 1$ correspond to $X_3 = 1/2$. Therefore, all points of the boundary $|\alpha|^2 = 1$ are mapped into the north pole of the Bloch sphere. For the interior points $|\alpha|^2 < 1$, the transformation is bijective, e.g., the origin $(Q, P) = (0, 0)$ is mapped into the south pole $X_3 = -1/2$.

By replacing Eqs. (3.20),(3.21), and (3.22) into the effective Hamiltonian Eq. (3.19) we obtain the LQE for the $m = 0$ case

$$\begin{aligned} E_G^{(0)}(Q,P) &= -h\left(|\alpha|^2 - \frac{1}{2}\right)\mathcal{J}_0\left[\frac{2\gamma_1^x}{\Omega}Q\sqrt{1-|\alpha|^2}\right] \\ &\quad + \frac{\gamma^y}{2}\left[\left(|\alpha|^2 - \frac{1}{2}\right)^2 - \left(1-|\alpha|^2\right)P^2\right]\mathcal{J}_0\left[\frac{4\gamma_1^x}{\Omega}Q\sqrt{1-|\alpha|^2}\right] \\ &\quad - \frac{\gamma^y}{2}\left[\left(|\alpha|^2 - \frac{1}{2}\right)^2 + \left(1-|\alpha|^2\right)P^2\right] - \gamma_0^x\left(1-|\alpha|^2\right)Q^2. \end{aligned} \tag{3.23}$$

In the undriven case, a classification of the quantum phases of the LMG Hamiltonian is usually performed by studying the global minima of the energy landscape [67]. However, in this work we interpret the local minima of the LQE as metastable phases of the driven system. These metastable states are related to the phenomenon of parametric stabilization [46]. Since these are separated from the global minima by macroscopic displacements, we expect transitions to be suppressed, such that the corresponding values of the order parameters are observable. This possibility is reinforced when one recalls that $E_G^{(\bar{0})}(Q, P)$ does not have the same thermodynamic significance as the lowest actual energy. Therefore, in this work we consider the number of minima of the LQE landscape as a criterion to establish a new phase diagram. A related work perform a quasienergy description of the Jaynes-Cummings model, where states localized at the bottom of the quasienergy landscape are squeezed [74]. Furthermore, in a driven Duffing oscillator, the multiphoton Rabi transitions and the relaxational transitions can be interpreted by means of quasienergy landscape [75].

Fig.3.2 depicts the phase diagram as a function of γ^y, γ_0^x and γ_1^x. In these phase diagrams, we see many regions corresponding to different number of minima of the LQE landscape. Additionally, the phase diagrams show the appearance of many novel metastable phases, which are separated from each other by boundary lines, whose crossings correspond to nonequilibrium multicritical points. By crossing the line $\gamma^y = -h$ in Fig.3.2 (a), the single global minimum at $(Q, P) = (0, 0)$ splits into two macroscopically separated global minima thus resembling the second order QPT known from the time-independent model. Interestingly, regions with even and odd number of minima are characterized by the existence of two and one global minima respectively. We can study the stability of the global minimum at $(Q, P) = (0, 0)$ analytically by computing the Jacobian-matrix at the origin of the LQE landscape and its eigenvalues

$$\lambda_1 = -2\left(h + \gamma^y\right), \tag{3.24}$$

$$\lambda_2 = -2h - 2\gamma_0^x - \left(h + \gamma^y\right)\left(\frac{\gamma_1^x}{\Omega}\right)^2. \tag{3.25}$$

Both eigenvalues are positive in the region $\gamma_y < -h$ (the contours $\lambda_1 = 0$ and $\lambda_2 = 0$ are depicted as red and black dashed lines respectively in Fig.3.2). In the region $\gamma_y > -h$ and $\gamma_1^x < \Omega\sqrt{\left(\frac{2h+2\gamma_0^x}{-h-\gamma^y}\right)}$ (region between the dashed curves in Fig.3.2 (a)), λ_1 is negative and λ_2 is positive. Furthermore λ_1 and λ_2 are negative for $\gamma_1^x > \Omega\sqrt{\left(\frac{2h+2\gamma_0^x}{-h-\gamma^y}\right)}$, and therefore, by crossing the curve $\lambda_2 = 0$, the saddle point at the origin becomes a local maximum. Consequently, in the region $\gamma_y > -h$ the single central minimum splits up in two global minima. The phase diagram depicted

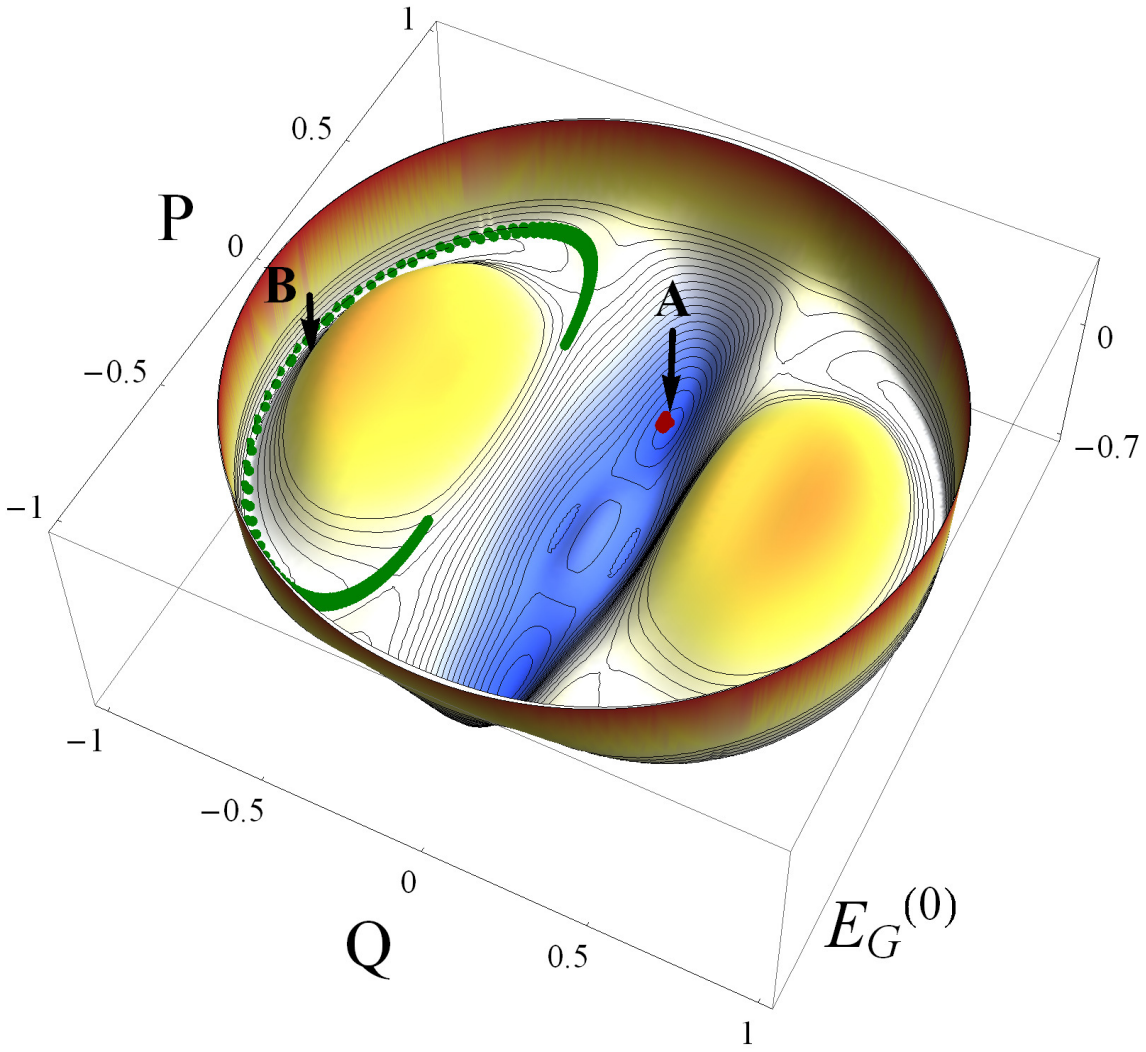

Figure 3.3.: Lowest quasienergy landscape for the parameters $\frac{1}{|h|}(h, \gamma_0^x, \gamma_1^x, \gamma^y) = (-1, -1, 210, 2)$. In the undriven system, these parameters correspond to the symmetry-broken phase. The quantum evolution for $N = 100$ particles within one period is calculated when the system is initialized in a spin coherent state. The green line on the surface depicts the evolution of an initial wave packet centered at minima B and the red line shows the corresponding evolution for a wave packet initially centered at A. We consider the parameters $\Omega/|h| = 40$ and $h/|h| = -1$.

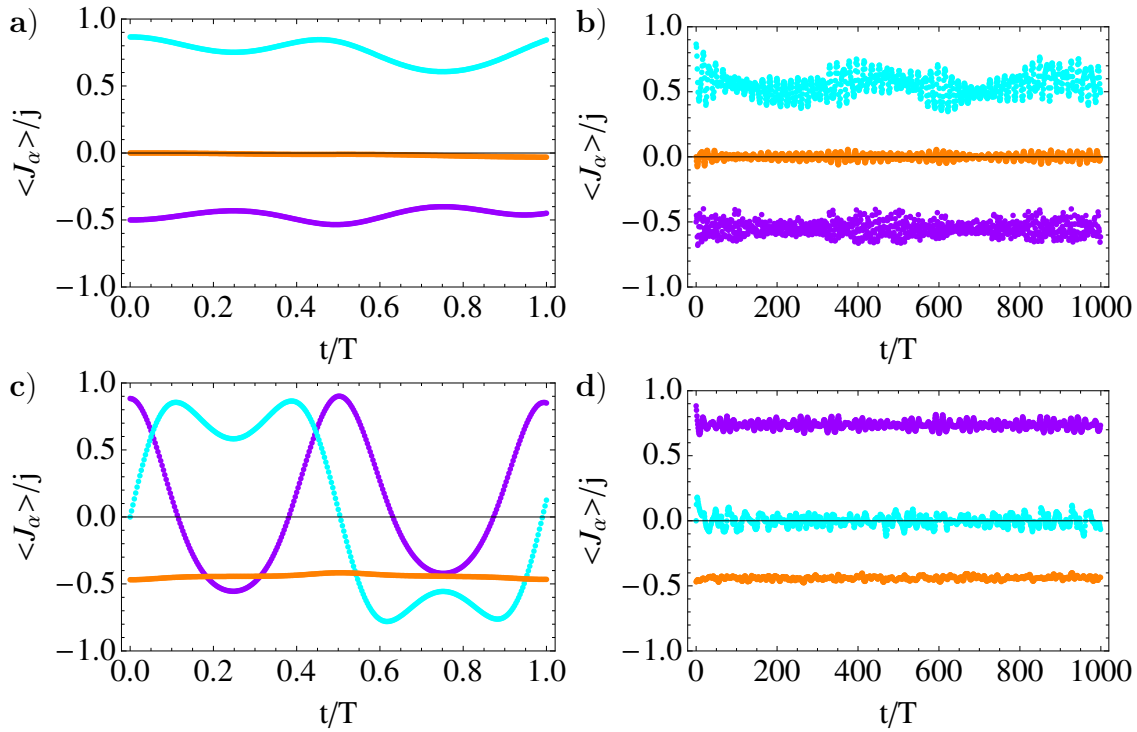

Figure 3.4.: Quantum evolution of the observables for finite size $N = 100$ and parameters $\frac{1}{|h|}(h, \gamma_0^x, \gamma_1^x, \gamma^y) = (-1, -1, 210, 2)$. The expectation values $\langle \hat{J}_x \rangle / j, \langle \hat{J}_y \rangle / j$ and $\langle \hat{J}_z \rangle / j$ are depicted by the orange, cyan and magenta curves respectively. (a) Depicts the quantum evolution within one period and (b) depicts the stroboscopic dynamics when the system is initialized in a wave packet centered at the minimum A depicted in Fig. 3.3. Correspondingly, (c) and (d) depict the inter-period and stroboscopic evolution, respectively, when the system is initialized in a wave packet centered at the minimum B depicted in Fig. 3.3. We consider the parameters $\Omega/|h| = 40$, $h/|h| = -1$.

in Fig.3.2 (b) is characterized by $\lambda_1 < 0$, and therefore, the dashed line corresponds to the boundary between the regions below and above the level curve $\lambda_2 = 0$, where the origin is a saddle point and a maximum respectively.

An example for the LQE is given in Fig. 3.3, where the parameters are chosen in such a way that the undriven system ($\gamma_1^y = 0$) is in the symmetry-broken phase. As the LQE corresponds to the ground state energy in the undriven case, it exhibits two global minima corresponding to macroscopically separated states degenerate in energy. In the driven system, apart from the two global minima characteristic of the undriven system (in Fig. 3.3 denoted with A), new characteristics of the LQE landscape appear, e.g. two local minima (denoted with B). These new local minima are strongly related to the quantum evolution of the system, as we describe in the next section.

3.4. Quantum evolution

In this section we investigate the quantum evolution when the system is initially prepared in a spin coherent state centered at a local minimum of the LQE surface. The spin coherent states are characterized by a minimum uncertainty and are the closest quantum states to a classical angular momentum state [76]. To describe geometrically the quantum evolution, we parametrize the Bloch sphere using spherical coordinates and express the angular momentum components in terms of the azimuthal (ϕ) and polar (θ) angles as follows:

$$X_1 = \frac{1}{2}\sin\theta\cos\phi, \tag{3.26}$$

$$X_2 = \frac{1}{2}\sin\theta\sin\phi, \tag{3.27}$$

$$X_3 = -\frac{1}{2}\cos\theta. \tag{3.28}$$

By replacing this set of equations into Eqs. (3.20)-(3.22) we find a relation between the (θ, ϕ) and (Q, P) coordinate systems

$$\theta = \pi - \arccos\left[2\left(Q^2 + P^2\right) - 1\right], \tag{3.29}$$

$$\phi = \arccos\left[\frac{2Q}{\sin(\theta)}\sqrt{1 - Q^2 - P^2}\right]. \tag{3.30}$$

With the angular coordinates ϕ and θ, we can represent the spin coherent state $|\phi, \theta\rangle$ by using

$$|\phi, \theta\rangle = (1 + |\tau|^2)^{-j} \exp[\tau \hat{J}_+] \, |j, -j\rangle, \tag{3.31}$$

with $\tau = e^{-i\phi}\tan\frac{\theta}{2}$. This procedure describes a mapping from a point of the LQE surface onto the set of spin coherent states.

To study the quantum evolution we consider a system consisting of $N = 100$ particles. For a finite size N, the numerical problem consists in the solution of $2N+1$ coupled ordinary differential equations. After the numerical integration of the Schrödinger equation, we construct the evolution operator $\hat{U}(t,0)$, which allows us to calculate the state of the system at any time $t > 0$: $|\Psi, t\rangle = \hat{U}(t,0)\,|\phi,\theta\rangle$, providing that we prepare initially the system in a spin coherent state $|\Psi, 0\rangle = |\phi,\theta\rangle$. We now proceed to calculate the normalized expectation values of the spin components in the state $|\Psi, t\rangle$. Fig. 3.4 (a) depicts the continuous time evolution within one period of the driving $T = 2\pi/\Omega$ of an initial wave packet centered at the minimum A in Fig. 3.3. Similarly, Fig. 3.4 (c) shows the inter-period dynamics when the initial wave packet is centered at the minimum B in Fig. 3.3.

To obtain a better geometrical picture of the quantum evolution we represent the mean values of the angular momentum components by means of the coordinates Q and P. Therefore, we project the expectation values onto the Bloch sphere by calculating the angles ϕ and θ and then solving Eqs. (3.29) and (3.30) for Q and P. The result is shown in Fig. 3.3 for $N = 100$ particles, where the time evolution for initial wave packets centered in minima A and B is depicted by the red and green curves, respectively. The trajectory initialized in A is strongly trapped within the minimum, whereas the other trajectory exhibits higher oscillations around the initial state. For finite size $N \gg 1$ the trajectories take place approximately over the surface of the LQE landscape, i.e., the mean value of the spin evolves in average along points with equal values of $E_G^{(0)}$. This behavior is connected to the fact that the eigenvalues of the effective Hamiltonian—from which the LQE is derived, correspond to the quasienergies of the system and the average value of the quasienergy is conserved in a time-periodic system. The state in the laboratory frame $|\Psi, t\rangle$ and the state in the rotating frame $|\Psi_m, t\rangle$ — in which the LQE is derived, are connected via

$$|\Psi, t\rangle = \hat{U}_m(t)|\Psi_m, t\rangle \tag{3.32}$$

$$\approx \hat{U}_m(t)\hat{e}^{-\mathrm{i}\hat{h}_0^{(m)}t}|\Psi, 0\rangle, \tag{3.33}$$

where $\hat{U}_{rot}(t,0) \approx \hat{e}^{-\mathrm{i}\hat{h}_0^{(m)}t}$ denote the propagator in the rotating frame and $|\Psi_m, 0\rangle = |\Psi, 0\rangle$ as a consequence of Eq. (3.10). Furthermore, the propagators in the laboratory and rotating frame are related by $\hat{U}(t,0) \approx \hat{U}_m(t)e^{-\mathrm{i}\hat{h}_0^{(m)}t}$. Additionally, there is a very interesting relation between the stroboscopic quantum evolution and the parity operator Eq. (3.2) that can be established using the relation

$$\hat{U}_m(t_r) = \left[\hat{\Pi}\exp\left(\mathrm{i}\frac{\pi N}{2}\right)\right]^{\frac{mr}{2}}, \tag{3.34}$$

for $t_r = \frac{2r\pi}{\Omega}$ with integer r. As a consequence of this, for $m = 0$ we have $\hat{U}_m(t_r) = \hat{\mathbb{1}}$, which implies that the states in the laboratory frame and in the rotating frame are

identical for these times. Thus, the stroboscopic time evolution is governed entirely by $\hat{h}_0^{(0)}$ (see Appendix A). The stroboscopic long-time evolution of the observables is displayed in Fig. 3.4(b). Here, the quantum evolution is strongly trapped in the neighborhood of the minimum A in Fig. 3.3. A similar situation occurs in Fig. 3.4(d) for a wave packet initially centered at the minimum B in Fig. 3.3. By calculating the quantum evolution with different system sizes, one finds that the quantum fluctuations of the trajectories decrease with number of particles, and therefore, in the thermodynamic limit, the time evolution has to be constrained to the LQE landscape. Because the time evolution is connected with the geometrical features of the LQE landscape, it is justified to use it as a background to define the existence of new metastable phases.

3.5. Experimental realization

Recently, the uniaxial LMG model has been realized experimentally by using a spinor Bose-Einstein condensate, where the inter-particle interaction can be controlled by means of Fechbach resonances [77]. Rather recently, appealing experimental realizations of the LMG model in optical cavity QED [78, 79] and circuit QED [80] have been suggested, which allow for a high degree of control of the system. Another possibilities are the optical realization of the uniaxial driven LMG in photonic lattices [81] and by using superconducting charge qubits connected in parallel to a common superconductor inductance [82]. Furthermore, a recent proposal allows for a realization of large-spin systems in molecular-magnets under the effect of periodic transverse fields [65].

The kicked top has been realized experimentally in an ensemble of laser-cooled Cs atoms [83], such a model is closely related to our model, the difference is that, whereas we consider a monochromatic driving, the experimental setup allows for a realization of multicolor driving, characteristic of a periodic train of delta kicks. Furthermore, a realization of two-axis-twisting Hamiltonian by using a two-component atomic Bose-Einstein condensate was recently suggested [84], the basic idea is that by using a repeated Rabi pulses control scheme on a one-axis-twisting Hamiltonian, which corresponds essentially to a driven version of the LMG model, it is possible to simulate stroboscopically an effective two-axis Hamiltonian.

4. AC-driven Quantum Phase Transitions in the Ising Model

The two preceding chapters described nonequilibrium aspects of criticality in $0+1$ dimensions, where 0 stand for the spatial dimension and 1 for the temporal dimension. In this chapter we study the one-dimensional AC-driven quantum Ising model. In the absence of driving, the Ising model is a paradigmatic model for quantum criticality in equilibrium and is exactly solvable even for a finite spin chain. In the thermodynamic limit, the Ising model exhibits a second-order QPT [3].

The dynamics of one-dimensional spin chains has been addressed extensively when the system is driven slowly through the critical point [12, 85, 86], where there is a diverging relaxation time and correlation length, and the dynamics cannot be adiabatic in the thermodynamic limit. As a consequence of this, the final state of the system consists of ordered domains whose finite size depend upon the velocity of the parameter variation [13]. A nontrivial oscillation of the magnetization [87] and the connection between symmetry and coherent destruction of tunneling (CDT) [88] has been investigated in a finite size periodically-driven Ising model. Furthermore, under the effect of a nonadiabatic external control of the transverse field, the Ising chain exhibits dynamical freezing of the response [89, 90], and synchronization with the external driving in the asymptotic dynamics as a consequence of destructive interference in time [91].

Our aim in this chapter is to describe the nonequilibrium behavior of a one-dimensional Ising model under the effect of a nonadiabatic monochromatic transverse field from the perspective of quantum criticality. In particular, we describe the dynamics by means of an effective Hamiltonian which simulates an undriven system. We show that in the asymptotic dynamics the nonequilibrium quantum phases correspond to states of the system which are synchronized with the driving. In contrast to previous works [89, 90, 91], however, we describe the role of manybody CDT in the critical behavior by investigating signatures of criticality both in the laboratory frame as well as in the rotating frame [92].

4.1. The driven Ising model

The periodically-driven transverse Ising model describes the dynamics of N interacting two-level systems in a time-dependent transverse local field [89, 90, 91]

$$\hat{H}(t) = -g(t)\sum_{i=1}^{N}\sigma_i^x - J\sum_{i=1}^{N}\sigma_i^z\sigma_{i+1}^z, \tag{4.1}$$

where σ_i^α are Pauli matrices at the ith site and we assume periodic boundary conditions $\sigma_1^\alpha = \sigma_{N+1}^\alpha$ for $\alpha \in \{x, y, z\}$. In the following we shall consider $J > 0$, and a monochromatic modulation of the transverse field with a static contribution $g(t) = g_0 + g_1 \cos \Omega t$. Associated with the Hamiltonian Eq. (4.1) is a conserved parity $\hat{\Pi}$, such that $[\hat{H}(t), \hat{\Pi}] = 0$, which is given by

$$\hat{\Pi} = \bigotimes_{i=1}^{N}\sigma_i^x. \tag{4.2}$$

4.1.1. The ferromagnetic QPT in the undriven Ising model

In the thermodynamic limit $N \to \infty$, the undriven Ising model ($g_1 = 0$) exhibits a second-order QPT at $g_0^c = J$ from a symmetric paramagnetic phase ($g_0 > J$) to a symmetry-broken ferromagnetic phase ($g_0 < J$) [3]. In the weak exchange interaction limit $g_0 \gg J$, the ground state is a paramagnet $|\psi\rangle_{\rm GP} = \bigotimes_{i=1}^{N} |\rightarrow\rangle_i$ with all the spins polarized up along the x axis. In the weak static transverse field limit $g_0 \ll J$, the system exhibits two degenerate ferromagnetic ground states with all the spins either pointing up $|\psi\rangle_{\rm GF,+} = \bigotimes_{i=1}^{N} |\uparrow\rangle_i$ or down $|\psi\rangle_{\rm GF,-} = \bigotimes_{i=1}^{N} |\downarrow\rangle_i$ along the z axis.

In the thermodynamic limit, the Ising model is characterized by an infinite set of collective excitations with fermionic character. Following closely the classic book of Sachdev [3] and Ref. [12], the Hamiltonian Eq. (4.1) in the undriven case $g_1 = 0$ can be written as a Hamiltonian of free spin-less fermions

$$\hat{H} = \frac{1}{2}\sum_k \epsilon_k(\hat{\gamma}_k^\dagger\hat{\gamma}_k - \hat{\bar{\gamma}}_k^\dagger\hat{\bar{\gamma}}_k) = \sum_{k\geq 0}\epsilon_k(\hat{\gamma}_k^\dagger\hat{\gamma}_k + \hat{\gamma}_{-k}^\dagger\hat{\gamma}_{-k} - \hat{\mathbb{1}}_k), \tag{4.3}$$

where $\hat{\mathbb{1}}_k$ is the identity operator acting in the Nambu subspace $\{|1_{-k}, 1_k\rangle, |0_{-k}, 0_k\rangle\}$ consisting of doubly occupied $|1_{-k}, 1_k\rangle$ and unoccupied $|0_{-k}, 0_k\rangle$ states of $\pm k$ fermions [85, 86, 93]. The energy dispersion of the spin-less fermions is given by

$$\epsilon_k = 2\sqrt{(g_0 - J\cos k)^2 + (J\sin k)^2}. \tag{4.4}$$

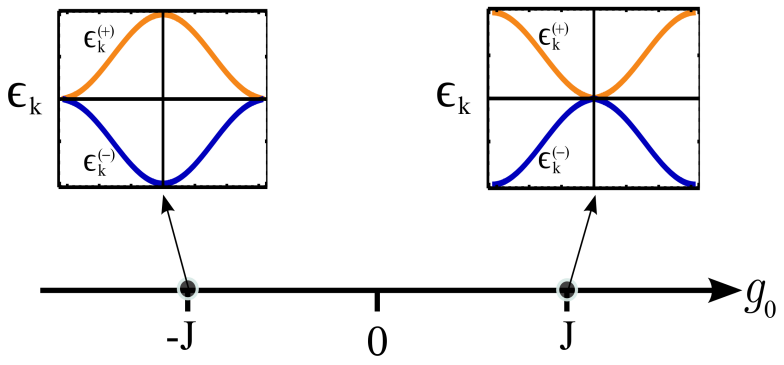

Figure 4.1.: Behavior of the energy dispersion ϵ_k at the critical points $g_0 = \pm J$.

To obtain Eq. (4.3) we have used the property $\hat{\tilde{\gamma}}_k = -\hat{\gamma}^\dagger_{-k}$ of the quasiparticle operator [12]. As a consequence of the parity Eq. (4.2), there is a doubling of the quasiparticle spectrum. Therefore, there are two branches of energy, i.e., $\epsilon_k^{(+)} = \epsilon_k$ for the "particles" and $\epsilon_k^{(-)} = -\epsilon_k$ for the "holes". This picture is very helpful because the energy dispersion of the "particles" resembles the conduction band, and the energy dispersion of the "holes" the valence band, respectively. Correspondingly, the band gap is given by $\Delta E_k = \epsilon_k^{(+)} - \epsilon_k^{(-)} = 2\epsilon_k$.

Similarly to the discussion made in the previous chapters, the QPT in the Ising model is characterized by a softening of a pair of k-modes, i.e., with momentum $+k$ and $-k$ respectively. In particular, for positive static transverse field $g_0 > 0$, the gap closes at the center $k = 0$ of the FBZ in quasimomentum space. In contrast, if one allows for a negative transverse field $g_0 < 0$, the gap closes at the boundaries $k = \pm\pi$ of FBZ. Figure 4.1 depicts the energy dispersion at the critical points.

The second derivative with respect to g_0 of the ground-state energy per particle

$$E_G^{(-)} = -\lim_{N\to\infty} \frac{1}{N} \sum_{k\geq 0} \epsilon_k = -\int_0^\pi \frac{dk}{2\pi} \epsilon_k = -\frac{2}{\pi}\sqrt{g_0^2 + J^2}\, E\left[\frac{4g_0 J}{(g_0+J)^2}\right], \qquad (4.5)$$

where $E[z]$ is the complete elliptic integral of the second kind [48], is not analytic, which is a signature of a second-order QPT [3].

4.2. The dynamic Bogoliubov-de Gennes equations

We consider the restriction of the Hamiltonian Eq. (4.1) to the subspace with even (+) number of fermionic quasiparticles (see Appendix C). After a Jordan-Wigner transformation, the Hamiltonian Eq. (4.1) can be written in terms of fermionic

operators. A discrete Fourier transform allows us to write the Hamiltonian Eq. (4.1) in quasimomentum space as follows

$$\hat{H}(t) = \sum_{k\geq 0} \left\{ 2\left[g(t) - J\cos k\right](\hat{c}_k^\dagger \hat{c}_k + \hat{c}_{-k}^\dagger \hat{c}_{-k}) - 2g(t)\hat{\mathbb{1}}_k \right\} + \sum_{k\geq 0} 2J\sin k(\hat{c}_k^\dagger \hat{c}_{-k}^\dagger + \hat{c}_{-k}\hat{c}_k) = \sum_{k\geq 0} \hat{H}_k(t), \tag{4.6}$$

where $\hat{c}_k^\dagger$ and $\hat{c}_k$ are fermionic operators [3]. For finite size N of the spin chain, the quasimomentum is restricted to $k \in \{\pm\frac{\pi}{N}, \pm\frac{3\pi}{N}, \ldots, \pm\frac{(N-1)\pi}{N}\}$. In the following, we focus on the thermodynamic limit $N \to \infty$, where we have $-\pi \leq k \leq \pi$.

Even if we prepare the system initially in a ground state of the undriven model, under the effect of nonadiabatic external driving, the system will experience transitions to excited states. Rather recently, a formalism has been developed to deal with this kind of dynamical situations [12, 85, 86, 94]. The idea is based on the fact that Hamiltonian Eq. (4.6) conserves momentum and parity. As a consequence, we can use the BCS ansatz for the evolution of the quantum state of the system

$$|\psi, t\rangle = \bigotimes_{k\geq 0} \left[u_k(t)|1_{-k}, 1_k\rangle + v_k(t)|0_{-k}, 0_k\rangle\right], \tag{4.7}$$

which implies that for a given quasimomentum k, the quantum evolution is restricted to the Nambu subspace.

The matrix representation of the operator $\hat{H}_k(t)$ in the Nambu subspace is given by

$$H_k(t) = \begin{pmatrix} \mu(t) - 2\omega_k & \Delta_k \\ \Delta_k & -\mu(t) \end{pmatrix}, \tag{4.8}$$

where $H_k(t)$ is the Bogoliubov-de Gennes (BdG) Hamiltonian, $\omega_k = 2J\cos k$, $\Delta_k = 2J\sin k$, and $\mu(t) = 2g(t)$. By defining the spinor $\Psi_k^\dagger(t) = (u_k^*(t), v_k^*(t))$, and considering the BCS ansatz Eq (4.7), it is possible to show that the coefficients $u_k(t)$ and $v_k(t)$ should satisfy the differential equation

$$\mathrm{i}\frac{d}{dt}\Psi_k(t) = H_k(t)\Psi_k(t), \tag{4.9}$$

which constitutes the dynamical version of the Bogoliubov-de Gennes equation [12]. At this point we have translated the manybody problem into the solution of the time-dependent Schrödinger equation for an effective two-level system. In Appendix B we discuss the more relevant aspects of the periodically-driven two-level system.

Under periodic driving, the Floquet theorem states that the solution of Eq. (4.9) can be written as

$$\Psi_k(t) = A_+ e^{-\mathrm{i}\varepsilon_k^{(+)}t}\Phi_k^{(+)}(t) + A_- e^{-\mathrm{i}\varepsilon_k^{(-)}t}\Phi_k^{(-)}(t), \tag{4.10}$$

where $\Phi_k^{(\pm)}(t)$ denote the Floquet modes corresponding to the quasienergies $-\Omega/2 \leq \varepsilon_k^{(\pm)} \leq \Omega/2$. Furthermore, in the extended Hilbert space $\mathscr{H} = \mathscr{R} \otimes \mathscr{T}$, where $\mathscr{R}$ is the Hilbert space of square integrable functions and $\mathscr{T}$ is the space of time-periodic functions (see Appendix A), the Floquet states satisfy the eigenvalue problem

$$\mathcal{H}_k \Phi_k^{(\lambda)}(t) = \varepsilon_k^{(\lambda)} \Phi_k^{(\lambda)}(t), \tag{4.11}$$

where $\lambda \in \{+,-\}$, $\mathcal{H}_k = H_k(t) - i\mathbb{1}_k \frac{\partial}{\partial t}$ is the Floquet-Bogoliubov-de Gennes (FBdG) Hamiltonian, $\varepsilon_k^{(\lambda)}$ are the quasienergies, and the Floquet modes $\Phi_k^{(\lambda)}(t+T) = \Phi_k^{(\lambda)}(t)$ have the same period $T = 2\pi/\Omega$ as the external driving [50, 52, 95].

4.2.1. Resonance conditions

As we have previously discussed in section 4.1, in the thermodynamic limit, the Ising model is characterized by an infinite set of collective excitations. Under the effect of an external driving, the possibility of multiphotonic resonances arises [50, 95]. To study such quantum resonances, let us consider the system in the absence of driving $g_1 = 0$. In this case, the Floquet modes and the quasienergies become the stationary states $\phi_k^{\pm}$ and the excitation spectrum $\epsilon_k^{(\pm)} = -\omega_k \pm \epsilon_k$ of the undriven system (see Eq. (4.4)), respectively [95]. Therefore, the solution of Eq. (4.9) can be written in the form of Eq. (4.10) as follows

$$\psi_k(t) = a_+ e^{-\mathrm{i}\epsilon_k^{(+)} t} \phi_k^{(+)} + a_- e^{-\mathrm{i}\epsilon_k^{(-)} t} \phi_k^{(-)}. \tag{4.12}$$

The condition for m-photon transitions is satisfied when the gap is an integer multiple of the driving

$$2\epsilon_k = m\Omega. \tag{4.13}$$

For a parametric oscillator with fundamental frequency ϵ_k, Eq. (4.13) is the usual resonance condition [46]. In Floquet theory, Eq. (4.13) implies the existence of a crossing between the single-particle energy levels ϵ_k and $-\epsilon_k$ when the energy spectrum is folded into the FBZ in quasienergy space [50]. Such a crossing occurs at the wave vector

$$k_0 = \pm \arccos\left(\frac{g_0^2 + J^2 - (\frac{m\Omega}{4})^2}{2 g_0 J} \right), \tag{4.14}$$

where the resonance condition is fulfilled, as depicted in Fig. 4.2 (a). Fig. 4.2 (a) depicts the energy dispersion relation of the undriven system and the continuous lines in Fig. 4.2 (b) the corresponding folding of the energy spectrum into the FBZ in quasienergy space $-\Omega/2 \leq \epsilon_k \leq \Omega/2$. In this thesis we focus on the weak spin-spin coupling limit $g_0, \Omega \gg J$. In this limit the multiphoton resonance condition reads

$$g_0 = \frac{m\Omega}{4}. \tag{4.15}$$

Such resonance condition will be used in the next section to perform a description of the system based on an effective time-independent Hamiltonian which is valid for parameters close to a multiphotonic resonance.

4.3. Physics in the rotating frame

The dynamical BdG equations allow us to investigate the full quantum evolution of the driven system. As we are interested in the asymptotic quantum dynamics and the description of critical signatures, it is convenient to describe the dynamics of the system in a rotating frame. In the weak spin-spin interaction limit, it is possible to neglect the fast oscillations in the rotating frame, and a description of the system based on the description for time-independent systems is possible via an approximate effective Hamiltonian.

4.3.1. The rotating wave approximation and the effective Hamiltonian approach

Motivated by the m-photon resonance condition in the weak spin-spin coupling limit Eq. (4.15), we perform a description of the system based on the RWA [52]. Let us perform a unitary transformation of the Hamiltonian Eq. (4.1) into a convenient rotating frame via the unitary operator

$$\begin{aligned}\hat{U}_m(t) &= \exp\left(\mathrm{i}\alpha_m(t)\sum_{i=1}^{N}\sigma_i^x\right) = \prod_{k\geq 0}\hat{U}_{k,m}(t) \\ &= \prod_{k\geq 0}\exp\left[-2\mathrm{i}\alpha_m(t)(\hat{c}_k^\dagger\hat{c}_k + \hat{c}_{-k}^\dagger\hat{c}_{-k} - \hat{\mathbb{1}}_k)\right],\end{aligned} \tag{4.16}$$

where $\alpha_m(t) = m(\Omega/4)t + \frac{g_1}{\Omega}\sin\Omega t$. In the Nambu subspace, the operator $\hat{U}_{k,m}(t)$ has the matrix representation

$$U_{k,m}(t) = \begin{pmatrix} e^{-2\mathrm{i}\alpha_m(t)} & 0 \\ 0 & e^{2\mathrm{i}\alpha_m(t)} \end{pmatrix}. \tag{4.17}$$

In the rotating frame, the dynamics is governed by the Hamiltonian $\hat{H}_m(t) = \hat{U}_m^\dagger(t)\hat{\mathcal{H}}\hat{U}_m(t)$, where

$$\hat{\mathcal{H}} = \hat{H}(t) - \mathrm{i}\frac{\partial}{\partial t} = \sum_{k\geq 0}\hat{\mathcal{H}}_k = \sum_{k\geq 0}\left[\hat{H}_k(t) - \mathrm{i}\hat{\mathbb{1}}_k\frac{\partial}{\partial t}\right] \tag{4.18}$$

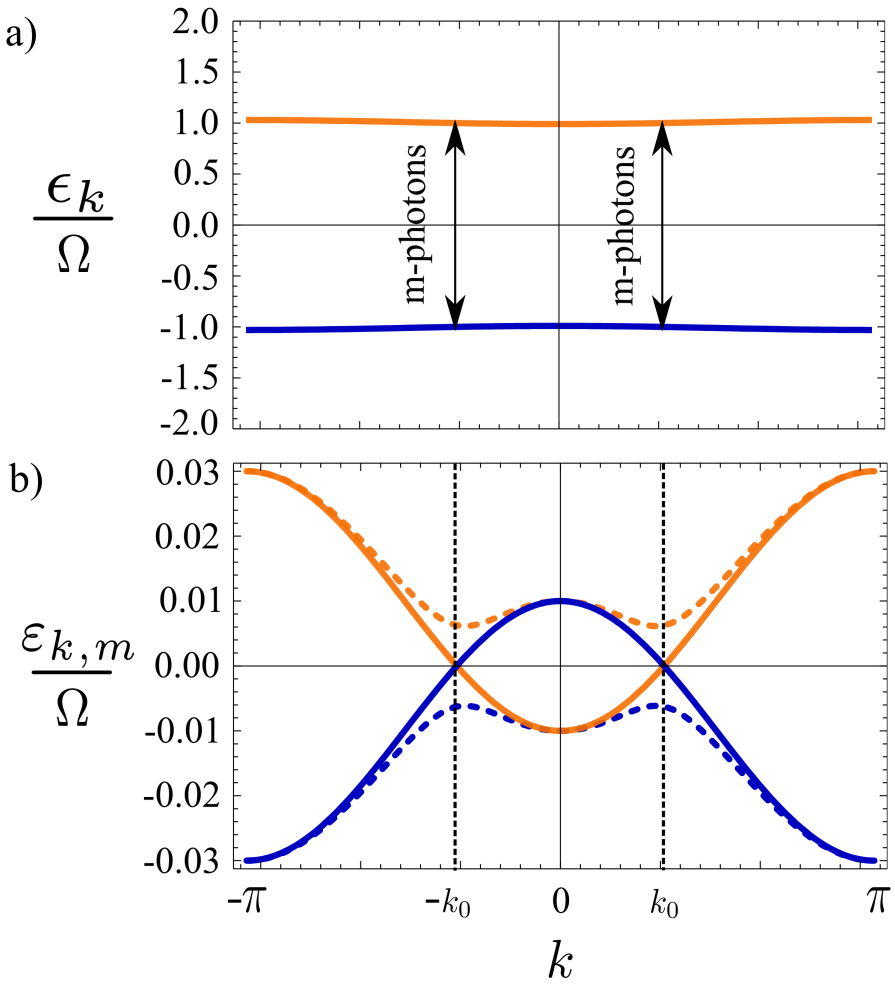

Figure 4.2.: (a) Typical gapped energy spectrum $\pm\epsilon_k$ of the undriven system corresponding to the paramagnetic phase $g_0 \gg J$. In this case, the energy dispersion is slightly curved because the curvature is proportional to the spin-spin interaction strength J. (b) The continuous lines depict the spectrum $\pm\epsilon_k$ when it is folded into the FBZ in quasienergy space, the crossing at $k = \pm k_0$ is related to a two-photon resonance. The dashed lines represent the quasienergy spectrum $\pm\varepsilon_{k,m}$ for a driving amplitude $g_1/\Omega = 1$. The parameters are $m = 2$, $J/\Omega = 0.01$, and $g_0/\Omega = 0.505$.

is the Floquet Hamiltonian. The explicit form of the Hamiltonian in the rotating frame is given by

$$\hat{H}_m(t) = -\delta^{(m)} \sum_{i=1}^{N} \sigma_i^x + \frac{J}{2} \sin[4\alpha_m(t)] \sum_{i=1}^{N} (\sigma_i^z \sigma_{i+1}^y + \sigma_i^y \sigma_{i+1}^z) \\ - \frac{J}{2} \{1 + \cos[4\alpha_m(t)]\} \sum_{i=1}^{N} \sigma_i^z \sigma_{i+1}^z - \frac{J}{2} \{1 - \cos[4\alpha_m(t)]\} \sum_{i=1}^{N} \sigma_i^y \sigma_{i+1}^y, \quad (4.19)$$

where the detuning $\delta^{(m)} = g_0 - m(\Omega/4)$ describes how far the system is detuned from resonance, and m is an integer that denotes the order of the multiphotonic resonance [50]. By using the identity

$$\exp(\mathrm{i}z \sin \Omega t) = \sum_{l=-\infty}^{\infty} \mathcal{J}_l(z) e^{\mathrm{i}l\Omega t}, \quad (4.20)$$

where $\mathcal{J}_l(z)$ is the lth-order Bessel function [48], the Hamiltonian Eq. (4.19) can be written in the form

$$\hat{H}_m(t) = \sum_{n=-\infty}^{\infty} \hat{h}_n^{(m)} e^{\mathrm{i}n\Omega t}. \quad (4.21)$$

As we describe in Appendix (A), we obtain an approximate Hamiltonian to describe the mth resonance by neglecting all the terms in $\hat{H}_m(t)$ with oscillatory time-dependence: $\hat{H}_m(t) \approx \hat{h}_0^{(m)}$. This approximation is valid as long as the conditions

$$\delta^{(m)}, J\mathcal{J}_m\left(\frac{4g_1}{\Omega}\right) \ll \Omega \quad (4.22)$$

holds [52].

Finally, we obtain the time-independent effective Hamiltonian

$$\hat{h}_0^{(m)} = -\delta^{(m)} \sum_{i=1}^{N} \sigma_i^x - \sum_{i=1}^{N} (J_z^{(m)} \sigma_i^z \sigma_{i+1}^z + J_y^{(m)} \sigma_i^y \sigma_{i+1}^y), \quad (4.23)$$

where the parameters $J_z^{(m)} = \frac{J}{2}[1 + (-1)^m \mathcal{J}_m(\frac{4g_1}{\Omega})]$ and $J_y^{(m)} = \frac{J}{2}[1 - (-1)^m \mathcal{J}_m(\frac{4g_1}{\Omega})]$ denote effective anisotropies in the rotating frame. Interestingly, the effective Hamiltonian Eq. (4.23) corresponds to an exactly solvable model, i.e., it is unitarily equivalent to the XY anisotropic spin chain in a transverse field [96, 97, 98]. However, in our case, the anisotropies depend both the order m of the resonance as well as the driving amplitude g_1. Therefore, the driving amplitude of the local field now plays the role of a new parameter that influences the criticality of the system.

4.3.2. Signatures of criticality in the rotating frame

Under the RWA, the Hamiltonian $\hat{h}_0^{(m)}$ and the Floquet Hamiltonian $\hat{\mathcal{H}} = \hat{H}(t) - \mathrm{i}\frac{\partial}{\partial t}$ are isospectral operators, which implies that the eigenvalues of the effective Hamiltonian correspond to the quasienergies.

As we show in Appendix D— similarly to the Ising model [3]—after a Jordan-Wigner transformation, and a discrete Fourier transform, the Hamiltonian Eq. (4.23) can be written as follows

$$\begin{aligned}\hat{h}_0^{(m)} = &\sum_{k\geq 0}\left[(2\delta^{(m)} - \omega_k)(\hat{c}_k^\dagger \hat{c}_k + \hat{c}_{-k}^\dagger \hat{c}_{-k}) - 2\delta^{(m)}\hat{\mathbb{1}}_k\right] \\ &+ \sum_{k\geq 0}(-1)^m \Delta_k \mathcal{J}_m\left(\frac{4g_1}{\Omega}\right)(\hat{c}_k^\dagger \hat{c}_{-k}^\dagger + \hat{c}_{-k}\hat{c}_k) = \sum_{k\geq 0}\hat{h}_{0,k}^{(m)}. \end{aligned} \tag{4.24}$$

The matrix representation of $\hat{h}_{0,k}^{(m)}$ in the Nambu subspace is given by

$$h_{0,k}^{(m)} = \begin{pmatrix} 2\delta^{(m)} - 2\omega_k & (-1)^m \Delta_k \mathcal{J}_m(\frac{4g_1}{\Omega}) \\ (-1)^m \Delta_k \mathcal{J}_m(\frac{4g_1}{\Omega}) & -2\delta^{(m)} \end{pmatrix}. \tag{4.25}$$

The Hamiltonian Eq. (4.24) can be diagonalized via a Bogoliubov transformation

$$\hat{h}_0^{(m)} = \sum_{k\geq 0}\varepsilon_{k,m}\left(\hat{\gamma}_k^\dagger \hat{\gamma}_k + \hat{\gamma}_{-k}^\dagger \hat{\gamma}_{-k} - \hat{\mathbb{1}}_k\right), \tag{4.26}$$

where

$$\varepsilon_{k,m} = 2\sqrt{(\delta^{(m)} - J\cos k)^2 + \left[J\mathcal{J}_m\left(\frac{4g_1}{\Omega}\right)\sin k\right]^2}. \tag{4.27}$$

Furthermore, the quasienergies are defined (modulus Ω) by the equation

$$\varepsilon_{k,m}^{(\pm)} = -\omega_k \pm \varepsilon_{k,m} + \frac{m\Omega}{2}, \tag{4.28}$$

as defined in Eq. (4.11). The quasienergy gap in the fermion picture is given by $\Delta E_{k,m} = \varepsilon_{k,m}^{(+)} - \varepsilon_{k,m}^{(-)} = 2\varepsilon_{k,m}$. Therefore, when the gap closes (modulus Ω), the effective Hamiltonian exhibits a behavior which resembles the dynamics of a critical quantum system. The dashed lines in Fig. 4.2 (b) depict the quasienergy dispersion relation for $g_1 \neq 0$. We observe that the driving lifts the degeneracy giving rise to an anticrossing. Based on the well-known results for the time-independent XY model that we summarize in Appendix D, we find that the system described by the effective Hamiltonian Eq. (4.23) exhibits an effective nonequilibrium Ising-like QPT along the critical lines $|\delta^{(m)}| = J$, and a nonequilibrium anisotropic QPT along the

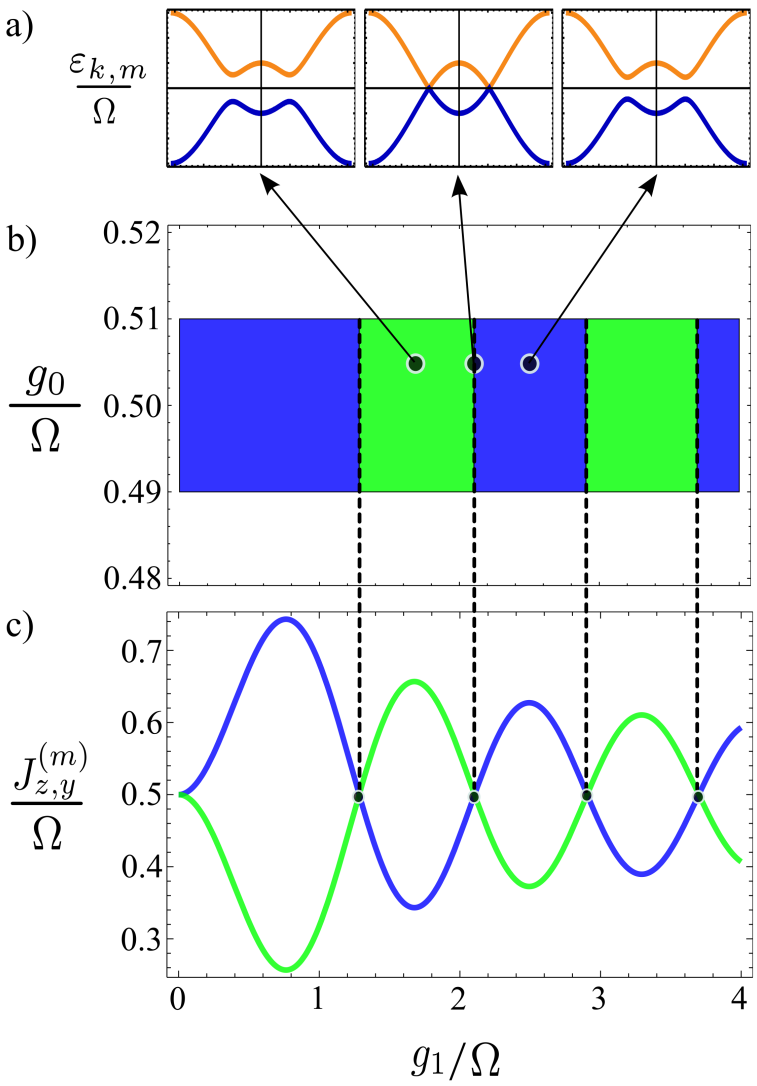

Figure 4.3.: Nonequilibrium QPT in the driven Ising chain in a time-dependent transverse field $g(t) = g_0 + g_1 \cos \Omega t$. (a) Depicts the quasienergy dispersion relations $\pm\varepsilon_{k,m}$ for parameters in the ferromagnetic phases FMZ and FMY, and along a critical line. (b) Depicts the phase diagram of the nonequilibrium phase transition around the $m = 2$ resonance as a function of the driving amplitude g_1 and the static local field g_0. The white zones represent the paramagnetic phase. Correspondingly, the blue zones represent the ferromagnetic phase FMZ and the green zones the ferromagnetic phase FMY. (c) Depicts the effective asymmetries in the z direction $J_z^{(m)}$ (blue curve) and y direction $J_y^{(m)}$ (green curve) as a function of the driving amplitude g_1. For this plot, we consider $J/\Omega = 0.01$.

lines where $\mathcal{J}_m\left(\frac{4g_1}{\Omega}\right) = 0$, as long as the condition $|\delta^{(m)}| < J$ holds. The anisotropic transition is characterized by two ferromagnetic phases, i.e., for $J_z^{(m)} > J_y^{(m)}$ the system is in a ferromagnetically-ordered phase along z direction FMZ, while it is the other way around in the FMY phase.

In a periodically-driven sytem, it can be defined a generalized parity symmetry in the extended Hilbert space $\mathscr{H} = \mathscr{R} \otimes \mathscr{T}$ (see Appendices A and B), where $\mathscr{R}$ is the Hilbert space of square integrable functions and $\mathscr{T}$ is the space of time-periodic functions [95]. The gapless quasienergy excitation spectrum for parameters along the critical lines is a direct consequence of coherent destruction of tunneling (CDT). This effect arises when there is a crossing of two energy levels as a consequence of the external driving. Therefore, by varying the parameters of the external control, the degeneracy can be created or lifted [99, 100]. Figure 4.3 (a) depicts the character of the quasienergy excitation spectrum $\pm\varepsilon_{k,m}$ for parameters in the ferromagnetic phase FMY, along the critical line, and in the ferromagnetic phase FMZ, respectively. Figure 4.3 (b) depicts the phase diagram for the nonequilibrium QPT in the neighborhood of the two-photon resonance. The white zones in the phase diagram correspond to the effective paramagnetic phase and are defined by the inequality $J < |\delta^{(m)}| < |\delta^{(m)}_{\max}|$, for $m = 2$, where $\delta^{(m)}_{\max}$ denotes the maximum detuning for which the RWA is still valid. In the particular case $\delta^{(m)} = 0$, the effective Hamiltonian Eq. (4.23) is unitarily equivalent to the XY model in the absence of transverse field. Therefore, in this special case the system only exhibits the conventional anisotropic transitions between the ferromagnetically ordered FMZ and FMY phases. In Fig. 4.3 (c) we plot the the effective asymmetries $J_z^{(m)}$ and $J_y^{(m)}$ as a function of the driving amplitude g_1 in the case of a two-photon resonance.

4.4. Physics in the laboratory frame

As we previously mentioned, the eigenvalues of the effective Hamiltonian Eq. (4.23) correspond to the quasienergies Eq. (4.27) of the system. However, the corresponding eigenstates do not necessarily correspond to Floquet modes. In order to obtain the Floquet modes, one should apply a unitary transformation back into the laboratory frame as we describe in Appendix A. Therefore, the Floquet k-eigenmodes $|\Phi^{(\pm)}_{k,m}, t\rangle = \hat{U}_{k,m}(t)|\chi^{(\pm)}_{k,m}\rangle$ can be written in terms of the states

$$\begin{aligned} |\chi^{(+)}_{k,m}\rangle &= \cos\phi_{k,m}|1_{-k}, 1_k\rangle - \sin\phi_{k,m}|0_{-k}, 0_k\rangle, \\ |\chi^{(-)}_{k,m}\rangle &= \sin\phi_{k,m}|1_{-k}, 1_k\rangle + \cos\phi_{k,m}|0_{-k}, 0_k\rangle, \end{aligned} \tag{4.29}$$

satisfying $h_0^{(m)}|\chi^{(\pm)}_{k,m}\rangle = \pm\varepsilon_{k,m}|\chi^{(\pm)}_{k,m}\rangle$, where we have used the basis of doubly occupied $|1_{-k}, 1_k\rangle$ and unoccupied $|0_{-k}, 0_k\rangle$ states of $\pm k$ fermions, and the Bogoliubov angle

$\phi_{k,m}$ is determined by the relation

$$\tan(2\phi_{k,m}) = \frac{-(-1)^m \Delta_k \mathcal{J}_m\left(\frac{4g_1}{\Omega}\right)}{2\delta^{(m)} - \omega_k}. \tag{4.30}$$

In the Nambu subspace the positive-quasienergy Floquet mode around the m-photon resonance is given by the spinor

$$\Phi^{(+)}_{k,m}(t) = e^{\mathrm{i}\left(\frac{m\Omega}{2}t\right)} U_{k,m}(t) \begin{pmatrix} \cos(\phi_{k,m}) \\ -\sin(\phi_{k,m}) \end{pmatrix} = \begin{pmatrix} e^{-\mathrm{i}\left(2\alpha_m(t) - \frac{m\Omega}{2}t\right)} \cos(\phi_{k,m}) \\ -e^{\mathrm{i}\left(2\alpha_m(t) + \frac{m\Omega}{2}t\right)} \sin(\phi_{k,m}) \end{pmatrix}, \tag{4.31}$$

and, correspondingly, the negative-quasienergy Floquet mode is given by

$$\Phi^{(-)}_{k,m}(t) = e^{\mathrm{i}\left(\frac{m\Omega}{2}t\right)} U_{k,m}(t) \begin{pmatrix} \sin(\phi_{k,m}) \\ \cos(\phi_{k,m}) \end{pmatrix} = \begin{pmatrix} e^{-\mathrm{i}\left(2\alpha_m(t) - \frac{m\Omega}{2}t\right)} \sin(\phi_{k,m}) \\ e^{\mathrm{i}\left(2\alpha_m(t) + \frac{m\Omega}{2}t\right)} \cos(\phi_{k,m}) \end{pmatrix}. \tag{4.32}$$

4.4.1. Quantum evolution of an initial paramagnetic state

Now, let us investigate the quantum evolution in the laboratory frame around the m-photon resonance when the system is initialized in a paramagnetic state of the undriven model with all the spin ensemble polarized along the x axis

$$|\psi_m, 0\rangle = \bigotimes_{i=1}^{N} |\rightarrow\rangle_i = \bigotimes_{k\geq 0} |0_{-k}, 0_k\rangle, \tag{4.33}$$

such that $\hat{\Pi}|\psi_m, 0\rangle = |\psi_m, 0\rangle$, where Π is the parity operator Eq. (4.2). Restricted to the Nambu subspace for a given $0 \leq k \leq \pi$, such an initial state corresponds to the spinor $\Psi^{\dagger}_{k,m}(0) = (u^*_{k,m}(0), v^*_{k,m}(0)) = (0, 1)$, whose quantum evolution is given by

$$\Psi_{k,m}(t) = U_{k,m}(t) \exp(-\mathrm{i}h^{(m)}_{0,k}t)\Psi_{k,m}(0) = -\sin(\phi_{k,m})\Psi^{(+)}_{k,m}(t) + \cos(\phi_{k,m})\Psi^{(-)}_{k,m}(t), \tag{4.34}$$

where $\Psi^{(\pm)}_{k,m}(t) = e^{-\mathrm{i}\varepsilon^{(\pm)}_{k,m}t}\Phi^{(\pm)}_{k,m}(t)$ denote the Floquet states restricted to the Nambu subspace.

In general, one can write the Floquet states as follows

$$|\Psi^{(\pm)}_m, t\rangle = \bigotimes_{k\geq 0} |\Psi^{(\pm)}_{k,m}, t\rangle = \bigotimes_{k\geq 0} e^{-\mathrm{i}\varepsilon^{(\pm)}_{k,m}t} |\Phi^{(\pm)}_{k,m}, t\rangle = \exp(-\mathrm{i}NE^{(\pm)}_m t) \bigotimes_{k\geq 0} |\Phi^{(\pm)}_{k,m}, t\rangle, \tag{4.35}$$

where $E^{(\pm)}_m = \pm \int_0^{\pi} \frac{dk}{2\pi} \varepsilon_{k,m}$ is the total quasienergy and $\varepsilon_{k,m}$ is the quasienergy dispersion defined in Eq. (4.27).

4.4.2. The dynamics of the transverse magnetization

By using the exact quantum evolution of the initial paramagnetic state, we are able to calculate the dynamics of physical observables in the laboratory frame. The transverse magnetization density $M_x(t)$ gives us information about the occurrence of a macroscopic polarization of the spins along the x axis. Let us consider the expectation value $M_x(t) = \frac{1}{N}\langle\psi_m, t|\sum_{i=1}^{N}\sigma_i^x|\psi_m, t\rangle$ close to the m-th resonance,

$$M_x(t) = -\int_0^{\pi}\frac{dk}{\pi}\Psi_{k,m}^{\dagger}(t)\sigma^z(k)\Psi_{k,m}(t) = 1 - 2\int_0^{\pi}\frac{dk}{\pi}\sin^2(\varepsilon_{k,m}t)\sin^2(2\phi_{k,m}), \tag{4.36}$$

where

$$\sigma^z(k) = \frac{1}{2}\frac{\partial\mathcal{H}_k}{\partial g_0} = \begin{pmatrix} 1 & 0 \\ 0 & -1 \end{pmatrix}, \tag{4.37}$$

and $\mathcal{H}_k$ is the FBdG Hamiltonian Eq. (4.11). Fig. 4.4 depicts the dynamics of the magnetization density in the thermodynamic limit calculated using RWA (black curve). In particular, Fig. 4.4 (a) shows the dynamics for parameters in the nonequilibrium paramagnetic phase, Fig. 4.4 (b) at the Ising-like critical line $\delta^{(m)} = J$, and Fig. 4.4 (c) for the ferromagnetic phase FMZ. We observe that in the paramagnetic phase the system exhibits a stationary state which corresponds to a polarized state along the local field direction. In contrast, for parameters corresponding to the critical line and the ferromagnetic phase FMZ, the state is not totally polarized along this direction. Furthermore, at the Ising-like critical line, the magnetization density does not exhibit oscillations. The green curve in Fig. 4.4 depicts the result of exact numerical calculation (see Appendix E) of the magnetization density for a finite size system $N = 100$.

In this dynamical scenario the connection with criticality is not obvious. Rather, signatures of quantum criticality in the laboratory frame may appear in the asymptotic dynamics. Let us consider now the time evolution of the expectation value of a general observable

$$\mathcal{O}(t) = \langle\psi_m, t|\hat{\mathcal{O}}|\psi_m, t\rangle = \int_0^{\pi}\frac{dk}{2\pi}\Psi_{k,m}^{\dagger}(t)\mathcal{O}_k\Psi_{k,m}(t). \tag{4.38}$$

In general, following the argument established in [91], it is possible to show that $\mathcal{O}(t) = \mathcal{O}^{\rm per}(t) + \mathcal{O}^{\rm tr}(t)$, where

$$\mathcal{O}^{\rm per}(t) = \sum_{\lambda\in\{+,-\}}\int_0^{\pi}\frac{dk}{2\pi}|A_\lambda|^2[\Phi_{k,m}^{(\lambda)}(t)]^{\dagger}\mathcal{O}_k\Phi_{k,m}^{(\lambda)}(t) \tag{4.39}$$

is the *periodic* contribution to the expectation value, which correspond to synchronization with the external driving. Here we consider $A_+ = -\sin[\phi_{k,m}]$ and

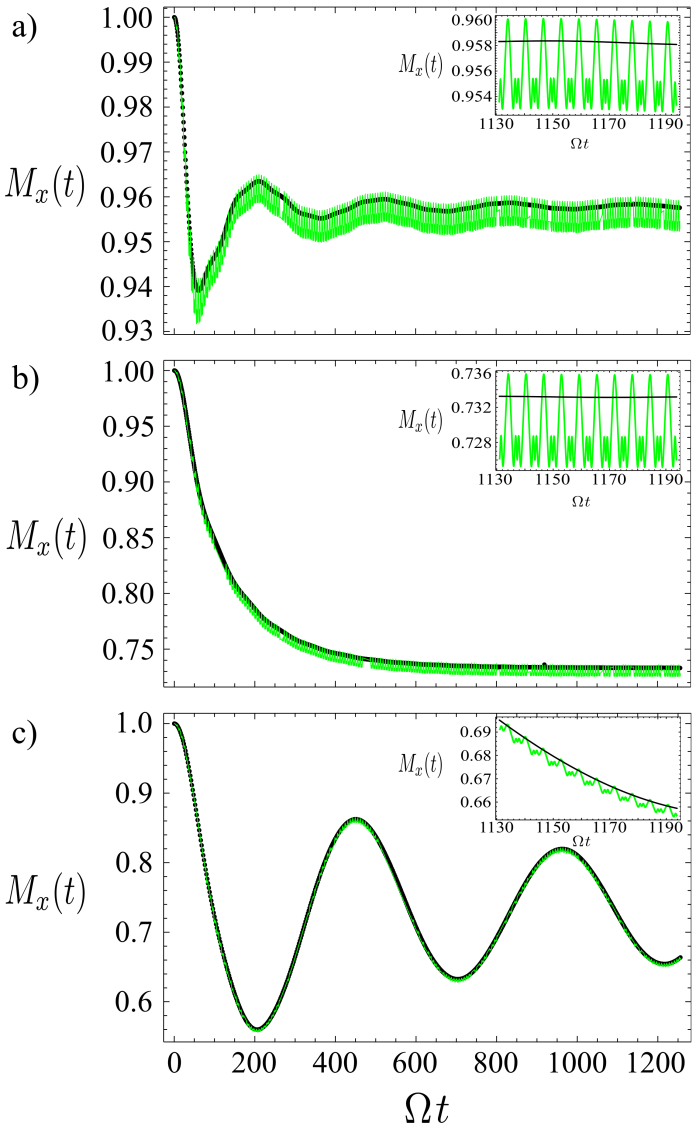

Figure 4.4.: Time evolution of the dimensionless magnetization density $M_x(t)$ in the thermodynamic limit (black curve) and exact numerical result for a finite system consisting of $N = 100$ spins (green curve) for $0 < t < 200T$, where $T = 2\pi/\Omega$ is the period of the external driving. Time evolution for parameters corresponding to (a) the nonequilibrium paramagnetic phase ($\delta^{(m)} > J$), for $m = 2$, where $(g_1/\Omega, g_0/\Omega) = (1, 0.515)$, (b) the Ising-like critical line ($\delta^{(m)} = J$), for $m = 2$, where $(g_1/\Omega, g_0/\Omega) = (1, 0.510)$, and (c) time evolution for parameters corresponding to the nonequilibrium ferromagnetic phase (FMZ) ($\delta^{(m)} < J$), for $m = 2$, where $(g_1/\Omega, g_0/\Omega) = (1, 0.505)$. The insets show the detail of the magnetization curves. For this plot, we consider $J/\Omega = 0.01$.

$A_- = \cos[\phi_{k,m}]$. Correspondingly,

$$\mathcal{O}^{\rm tr}(t) = \int_0^\pi \frac{dk}{\pi} \Re \left\{ A_+^* A_- e^{-2i\varepsilon_{k,m}t} [\Phi_{k,m}^{(+)}(t)]^\dagger \mathcal{O}_k \Phi_{k,m}^{(-)}(t) \right\}. \tag{4.40}$$

denotes the *transient* component, which decays to zero in the long-time limit as a consequence of destructive interference in time [91]. Therefore, the system tends to synchronize with the external control in the long-time limit. The particular case $\delta^{(m)} = 0$ for $m = 0$ has been discussed in Ref. [89] in the context of freezing of the response in a manybody system. In this case, the system only exhibits the conventional anisotropic transition, which is reflected in the behavior of the magnetization dynamics. Furthermore, the anisotropic critical lines $\mathcal{J}_0(4g_1/\Omega) = 0$ are related to the effect of maximal freezing discussed in Ref. [89]. We conclude that in the asymptotic dynamics, the Floquet modes determine the quantum critical behavior, as we discuss in the next section.

4.4.3. Cycle-averaged expectation values in Floquet eigenstates

We now define cycle-averaged expectation values of physical observables. In the case of a time-dependent Hamiltonian $\hat{H}(t)$, the energy is not conserved. Therefore, to describe signatures of the quantum phase transition in the laboratory frame we define the averaged energy $\bar{H}_m^{(\pm)}$ in the Floquet state Eq. (4.35) as

$$\begin{aligned} \bar{H}_m^{(\pm)} &\equiv \frac{1}{N} \int_0^T \frac{dt}{T} \left\langle \Psi_m^{(\pm)}, t \left| \hat{H}(t) \right| \Psi_m^{(\pm)}, t \right\rangle = \int_0^T \frac{dt}{T} \int_0^\pi \frac{dk}{2\pi} [\Psi_{k,m}^{(\pm)}(t)]^\dagger H_k(t) \Psi_{k,m}^{(\pm)}(t) \\ &= \int_0^T \frac{dt}{T} \int_0^\pi \frac{dk}{2\pi} \left(\varepsilon_{k,m}^{(\pm)} + i[\Phi_{k,m}^{(\pm)}(t)]^\dagger \frac{\partial}{\partial t} \Phi_{k,m}^{(\pm)}(t) \right). \end{aligned} \tag{4.41}$$

By using the analytic expressions for the Floquet modes Eqs. (4.31) and (4.32) we obtain the expression

$$\bar{H}_m^{(\pm)} = \pm \int_0^\pi \frac{dk}{2\pi} \left(\varepsilon_{k,m} + \frac{m\Omega}{2} \cos(2\phi_{k,m}) \right), \tag{4.42}$$

where $\phi_{k,m}$ is the Bogoliubov angle defined in Eq. (4.30). On resonance $\delta^{(m)} = 0$, we get an analytical expression for the cycle averaged energy

$$\bar{H}_m^{(\pm)} = \pm \frac{2J}{\pi} E \left[1 - \left[\mathcal{J}_m \left(\frac{4g_1}{\Omega} \right) \right]^2 \right], \tag{4.43}$$

where $E[z]$ is the complete elliptic integral of the second kind (see Appendix D). This result confirms our prediction based on the description of the system in the

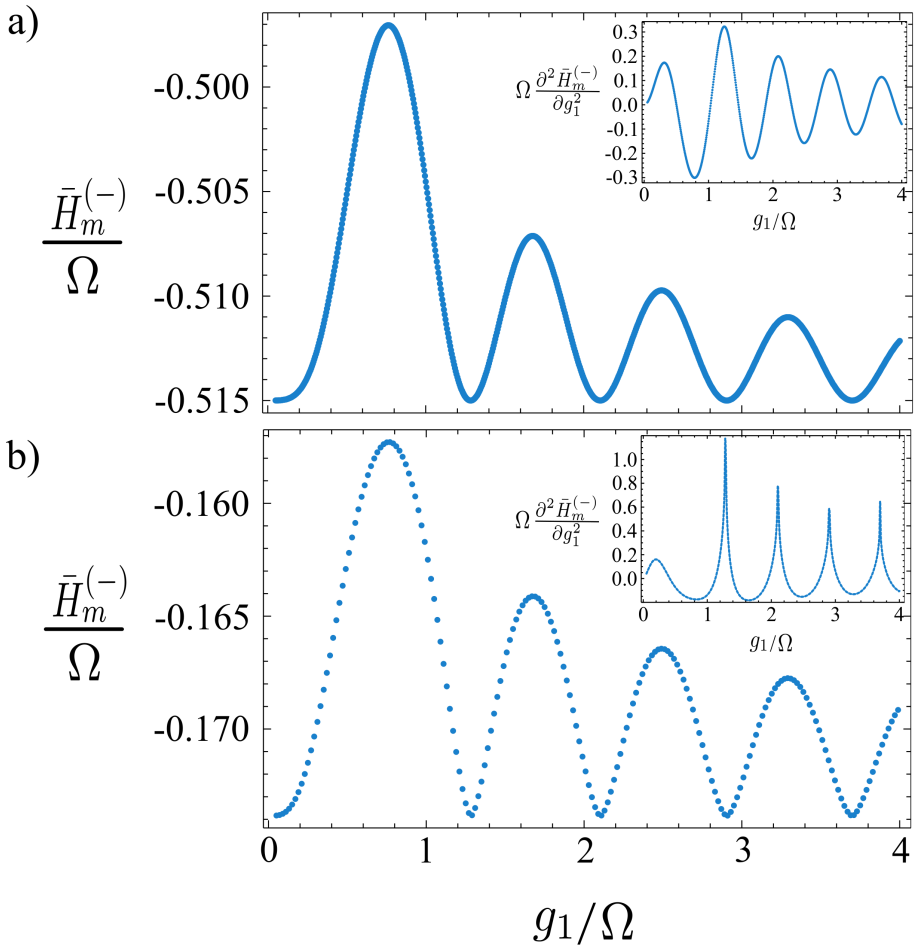

Figure 4.5.: Cycle-averaged energy $\bar{H}_m^{(-)}$ as a function of the driving amplitude g_1. (a) For parameters in nonequilibrium paramagnetic phase ($\delta^{(m)} > J$), for $m = 2$, where $g_0/\Omega = 0.515$. (b) For parameters inside the ladder of ferromagnetic phases ($\delta^{(m)} < J$), for $m = 2$, where $g_0/\Omega = 0.505$. The insets depict the second derivative of the cycle-average energy as a function of the driving amplitude g_1. For this plot, we consider $J/\Omega = 0.01$.

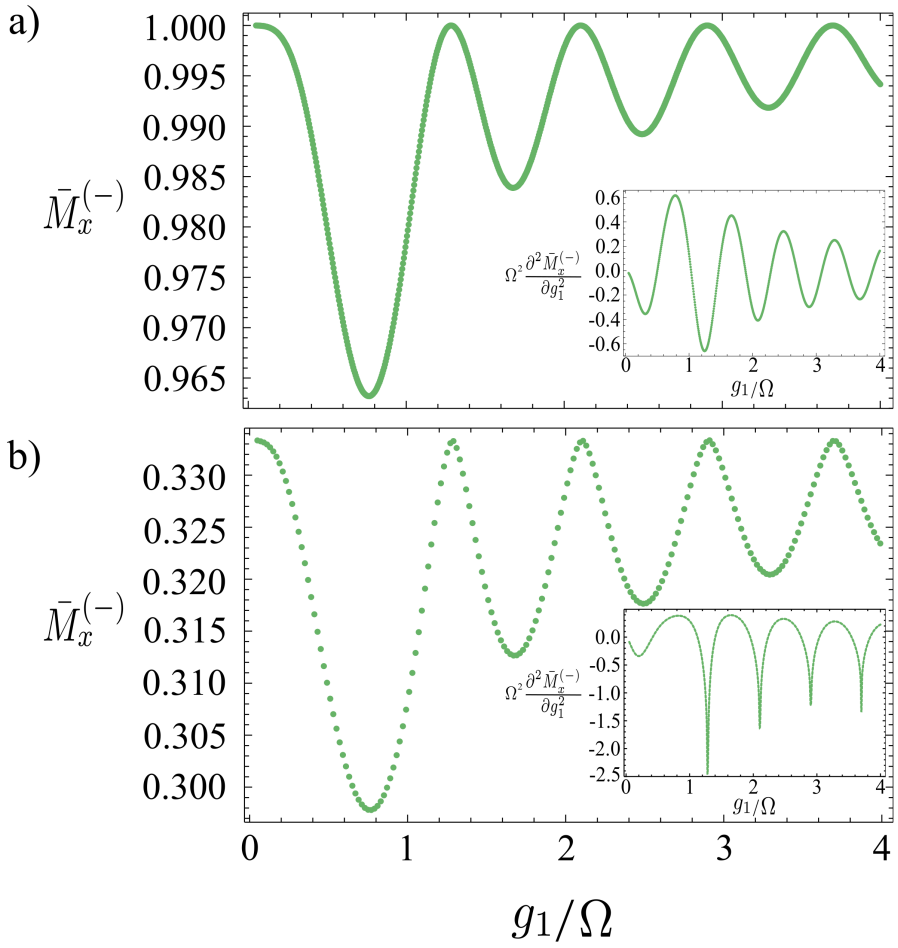

Figure 4.6.: Cycle-averaged dimensionless magnetization $\bar{M}_z^{(-)}$ as a function of the driving amplitude g_1. (a) For parameters in the nonequilibrium paramagnetic phase ($\delta^{(m)} > J$), for $m = 2$, where $g_0/\Omega = 0.515$. (b) For parameters inside the ladder of ferromagnetic phases ($\delta^{(m)} < J$), for $m = 2$, where $g_0/\Omega = 0.505$. The insets depict the second derivative of the cycle-average magnetization as a function of the driving amplitude g_1. For this plot we consider $J/\Omega = 0.01$.

rotating frame (see Fig. 4.3). The cycle-averaged energy exhibits singularities at the zeros of the Bessel function, i.e., $\mathcal{J}_m\left(\frac{4g_1}{\Omega}\right) = 0$. This is a clear signature of a critical nonequilibrium behavior. Finally, we calculate the cycle-averaged transverse magnetization in the Floquet state Eq. (4.35). By considering the extension of the Hellmann-Feynman theorem for Floquet theory [95], we can compute the cycle-averaged magnetization $\bar{M}_x^{(\pm)}$ in terms of derivatives of the quasienergies as follows

$$\begin{aligned}\bar{M}_x^{(\pm)} &\equiv \frac{1}{N}\int_0^T \frac{dt}{T}\left\langle \Psi_m^{(\pm)}, t \left| \sum_{i=1}^{N} \sigma_i^x \right| \Psi_m^{(\pm)}, t \right\rangle \\ &= -\int_0^T \frac{dt}{T}\int_0^\pi \frac{dk}{2\pi}[\Psi_{k,m}^{(\pm)}(t)]^\dagger \left(\frac{\partial \mathcal{H}_k}{\partial g_0}\right)\Psi_{k,m}^{(\pm)}(t) \\ &= -\int_0^\pi \frac{dk}{2\pi}\frac{\partial \varepsilon_{k,m}^{(\pm)}}{\partial g_0} = \mp\int_0^\pi \frac{dk}{\pi}\cos(2\phi_{k,m}). \end{aligned} \tag{4.44}$$

Figures 4.5 and 4.6 show the cycle-averaged expectation values of observables. Similarly to the undriven case, the system exhibits nonanalyticities in the second derivative of observables as can be seen in the corresponding insets, thus resembling a continuous phase transition. Such nonanalyticities arise as a consequence of CDT [99, 100], and therefore, from the gapless quasienergy spectrum.

4.5. Experimental realization

Recently, experimental realizations of one-dimensional spin chains have been suggested, where a quantum simulation of the system close to the phase transition is possible, and a wide freedom on the control of the parameters is achieved [27, 28, 29, 30, 31, 32]. A possible experimental implementation of our model could be achieved based on a configuration of superconductor quantum bits with programable spin-spin interaction [27], such a setup allows for a high degree of control of the system parameters. We anticipate that under an adiabatic change of the static local field g_0 and the driving amplitude g_1 our model could be interesting in the context of quantum annealing, as the effective Hamiltonian Eq. (4.23) corresponds to the XY model. Another experimental setups can be realized by means of cold atoms [28, 29, 32], and in fully C-labelled sodium butyrate using liquid state nuclear magnetic resonance [101, 102].

5. AC-driven Quantum Phase Transitions in the Wen-plaquette Model

States of matter are commonly characterized within the Landau paradigm as symmetry-broken phases, i.e., a solid corresponds to a translation-symmetry broken phase, a magnet to rotational-broken symmetry, and a superconductor to a $U(1)$-broken phase. However, rather recently, novel states of matter have been discovered, which cannot be characterized within the Landau criteria. Examples of such a states of matter include integer and fractional quantum Hall effect [7, 8], topological insulators and superconductors [5, 6, 9]. In contrast to the usual QPTs, a topological quantum phase transition (TQPT) is a change of phase in which the symmetry of the ground state does not change, the low energy effective theory describing this novel phases corresponds to a topological quantum field theory (TQFT).

In the case of conventional QPT, our experience with the Dicke, LMG and Ising models shows that under the effect of an external driving, the system exhibits effective interactions, which give rise to novel "synthetic" quantum phases. Such states correspond to metastable states and their description involves higher order terms of the order parameter in the low-energy effective theory. In these examples, even under the effect of driving, the quantum states of matter correspond to symmetry broken phases in the thermodynamic limit, i.e., the superradiant state does not conserve the parity Eq. (2.2). Our aim in this chapter is to study the behavior of the topological quantum phase transition in the Wen-plaquette model (WPM) under external driving. The WPM has intriguing relations to other models studied in the literature. For example, it has been shown that the WPM can be exactly mapped to the toric code of Kitaev [103, 104]. Furthermore, the toric code in a paralell magnetic field has low energy properties that resemble the two dimensional transverse Ising model, which allows to study the influence of an external field in the TQPT [105]. The effect of a transverse perturbation on the topological protection in the toric code has been explored by using a mapping onto the Xu-Moore model, which subsequently can be mapped onto the Compass model [106]. We show that under the effect of a nonadiabatic driving the system exhibits a novel topological phase. We define generalized "string"-like topological order parameters by

considering cycle-averaged expectation values of string operators in a Floquet state [107].

5.1. The driven transverse Wen-plaquette model

In this section we focus on the driven Wen-plaquette model in a transverse field on a $N \times N$ square lattice

$$\hat{H}(t) \;=\; -g(t)\sum_{i,j}\hat{X}_{i,j} - J\sum_{i,j}\hat{F}^{z}_{i,j}, \tag{5.1}$$

where

$$\hat{F}^{z}_{i,j} = \hat{X}_{i,j}\hat{Y}_{i+1,j}\hat{X}_{i+1,j+1}\hat{Y}_{i,j+1} \tag{5.2}$$

is the plaquette operator, $\hat{X}_{i,j}$,$\hat{Y}_{i,j}$, $\hat{Z}_{i,j}$ are the Pauli operators acting on the (i,j)-th site, and we consider a time-dependent transverse field $g(t) = g_0 + g_1\cos\Omega t$.

Fig. 5.1 (a) depicts the geometry of the plaquette operator. A plaquette is even (odd) if the relation $(-1)^{i+j} = 1$ ($(-1)^{i+j} = -1$) is satisfied [108], as depicted in Fig. 5.1 (b). In the topological order, the undriven Wen plaquette model hosts three types of quasiparticles: Z_2 charges, Z_2 vortices, and fermions, and three types of string operators T_1, T_2, T_3 are defined, respectively [108]. The T_1 string operator for a Z_2 charge is given by

$$\widehat{W}_{\mathrm{c}}(C) = \bigotimes_{C}\hat{Y}_{i,j}. \tag{5.3}$$

$\widehat{W}_{\mathrm{c}}$ is the product of spin operators along a path C connecting even plaquettes of neighboring links (see Fig. 5.1 (c)). Correspondingly, the T_2 string operator for a Z_2 vortex is given by

$$\widehat{W}_{\mathrm{v}}(\widetilde{C}) = \bigotimes_{\widetilde{C}}\hat{X}_{i,j}. \tag{5.4}$$

In this case, $\widehat{W}_{\mathrm{v}}$ is the product of spin operators along a path $\tilde{C}$ connecting odd plaquettes of neighboring links (see Fig. 5.1 (c)). Finally, the T_3 string operators are defined as bounded states of T_1 and T_2 strings, they are charge-vortex composite objects, and their definition is given in Refs. [108, 109].

5.1.1. String-net states and string-net operators

Now, let us discuss briefly the quantum states of the theory. In the last section we have defined string excitation operators $\widehat{W}_{\mathrm{c}}(C)$ and $\widehat{W}_{\mathrm{v}}(\widetilde{C})$, the effect of these

operators is to create nonlocal excitations above the ground state of the system. Therefore, a generic string state has the form

$$|C_1\ C_2 \cdots\rangle = \widehat{W}(C_1)\widehat{W}(C_2)\cdots|0\rangle, \tag{5.5}$$

where $C_1, C_2, \ldots$ are strings with no overlapping ends. Such a state is called a string-net state and the operator $\widehat{W}(C_{\text{net}}) = \widehat{W}(C_1)\widehat{W}(C_2)\cdots$ is a string-net operator.

5.1.2. The duality transformation

In this section we show that the Wen-plaquette model can be mapped into a set of decoupled one-dimensional Ising chains via a duality transformation [104, 108, 109]. Therefore, in the thermodynamic limit $N \to \infty$, using this duality, the TQPT can be understood in terms of the Ising quantum phases. To obtain the mapping, we observe that the operators $\hat{F}^z_{i,j}$ and $\hat{X}_{i,j}$ satisfy the following commutation relations

$$\begin{aligned}
[\hat{F}^z_{a,b}, \hat{X}_{c,d}] &= 2\hat{F}^z_{a,b}\hat{X}_{c,d}(\delta_{a+1,b} + \delta_{a,b+1})\delta_{c,d}, \\
[\hat{F}^z_{a,b}, \hat{F}^z_{c,d}] &= 0, \\
[\hat{X}_{a,b}, \hat{X}_{c,d}] &= 0.
\end{aligned} \tag{5.6}$$

Now, let us define a representation of this algebra by means of Pauli matrices $\{\tau^x_{i,j}, \tau^y_{i,j}, \tau^z_{i,j}\}$ on the dual lattice

$$\begin{aligned}
\hat{F}^z_{i^*,j^*} &\mapsto \tau^x_{i^*,j^*}, \\
\hat{X}_{i^*,j^*} &\mapsto \tau^z_{i^*,j^*}\tau^z_{i^*,j^*+1}.
\end{aligned} \tag{5.7}$$

We parametrize the sites of the dual lattice by means of $(i^*, j^*) = (i - j + 1, j)$. Under this duality transformation the Hamiltonian Eq. (5.1) can be written in terms of N decoupled 1-dimensional Ising chains [104, 108, 109]. In this work i^* denotes the chain index and j^* the sites along the corresponding Ising chain. Under this representation we are able to write the Wen-plaquette Hamiltonian Eq. (5.1) as follows

$$\hat{H}^\tau(t) = -g(t)\sum_{i^*,j^*}^{N}\tau^z_{i^*,j^*}\tau^z_{i^*,j^*+1} - J\sum_{i^*,j^*}^{N}\tau^x_{i^*,j^*} = \sum_{i^*=1}^{N}\hat{H}^\tau_{i^*}(t), \tag{5.8}$$

where

$$\hat{H}^\tau_{i^*}(t) = -g(t)\sum_{l=1}^{N}\tau^z_l\tau^z_{l+1} - J\sum_{l=1}^{N}\tau^x_l, \tag{5.9}$$

and N is the length of the spin chain. For the i^*-th Ising chain, we have introduced the identification $\tau^\alpha_l = \tau^\alpha_{i^*,l}$ for $\alpha \in \{x, y, z\}$ in order to avoid the use of the vector

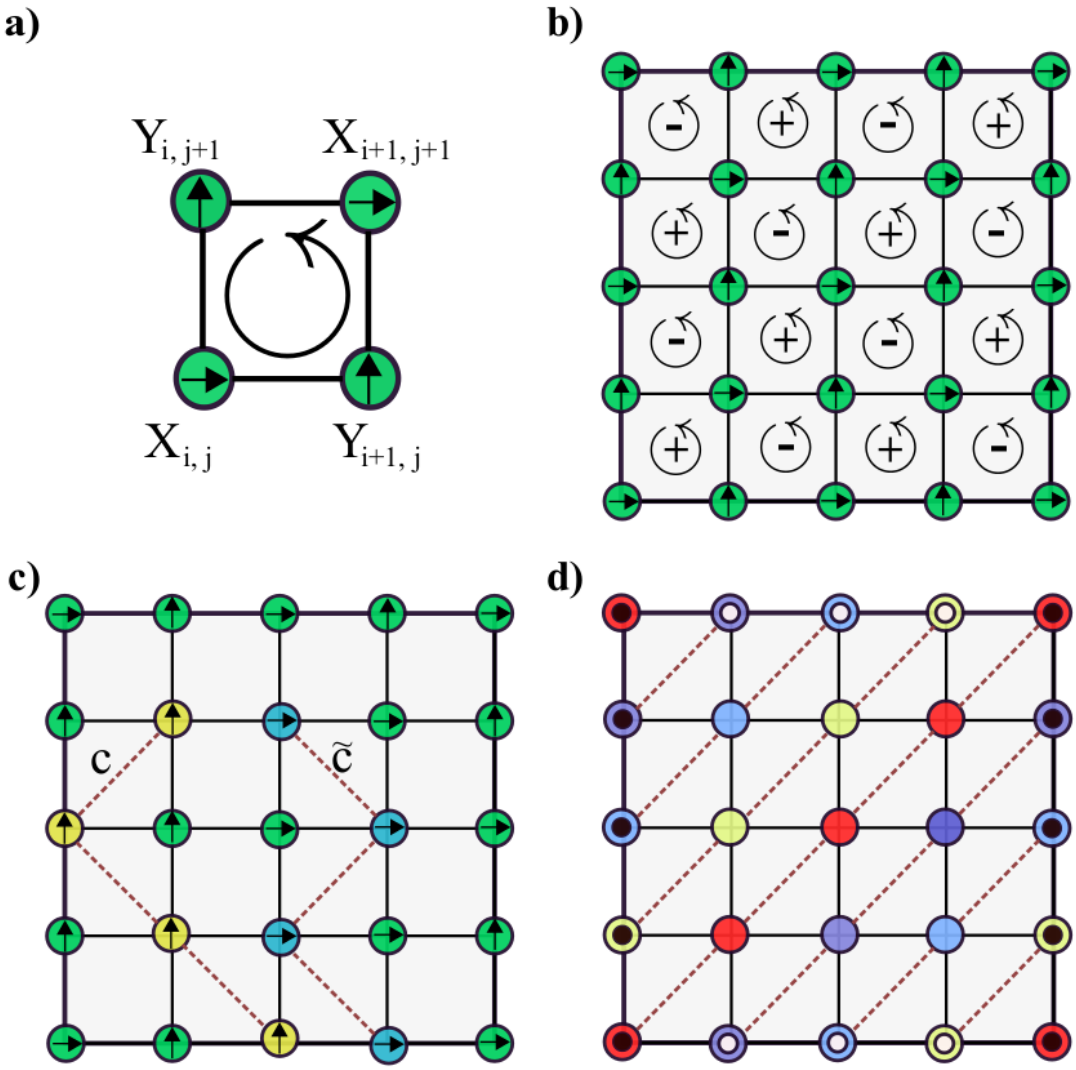

Figure 5.1.: The Wen-plaquette model. In (a) we represent the geometry of plaquette operator at the site (i, j). Figure (b) depicts the real space lattice and the corresponding even $(+)$ and odd plaquettes $(-)$. (c) Shows the T_1 string operators along the path C, and T_2 string operator along $\widetilde{C}$. Figure (d) shows the dual lattice and represent the N decoupled Ising chains, the colors represent the lattice points belonging to the same Ising chain. To describe the boundary conditions, we depict white and black dots to identity the equivalent lattice points.

indices introduced previously. The geometry of the decoupled Ising chains in shown in Fig. 5.1 (d) and in Fig. 5.2 (d). Therefore, to understand the novel behavior of the Wen model under the effect of driving we must understand the quantum criticality in the driven Ising model Eq. (5.9). However, one can take advantage of the Kramers-Wannier self duality [110, 111]

$$\begin{aligned} \tau_l^x &\mapsto \sigma_l^z \sigma_{l+1}^z, \\ \tau_s^z &\mapsto \bigotimes_{r\leq s} \sigma_r^x \end{aligned} \tag{5.10}$$

and obtain a dual spin Hamiltonian

$$\hat{H}_{i^*}^{\sigma}(t) \;=\; -g(t)\sum_{l=1}^{N}\sigma_l^x - J\sum_{l=1}^{N}\sigma_l^z\sigma_{l+1}^z, \tag{5.11}$$

which corresponds exactly to the Hamiltonian Eq. (4.1) discussed in Sec. 4.1 of Chap. 4. We have previously investigated this model and has a well-known phase diagram [92]. In the next section we discuss the general aspects of the TQPT in the undriven Wen-plaquette model.

5.1.3. The TQPT in the undriven transverse Wen-plaquette model

Now, we are able to understand the TQPT in terms of the well-known phases of the Ising chain. Let us consider first the case of the undriven Wen-plaquette model $g_1 = 0$. It is a well-known fact that in the thermodynamic limit $N \to \infty$, the quantum Ising model exhibits a second order QPT from a paramagnetic phase into a ferromagnetic ordered phase at $g_0 = J$. However, to describe the TQPT in the Wen-plaquette model we should define global order parameters [108, 109, 112] as expectation values of nonlocal operators in the ground state of the system

$$\begin{aligned} \Phi_1 &= \lim_{R\to\infty}\left\langle \bigotimes_{j^*=1}^{R}\hat{X}_{1,j^*}\right\rangle = \lim_{R\to\infty}\left\langle \bigotimes_{l=1}^{R}\tau_l^z\tau_{l+1}^z\right\rangle = \lim_{R\to\infty}\left\langle \tau_1^z\tau_{R+1}^z\right\rangle, \\ \Phi_2 &= \lim_{R\to\infty}\left\langle \bigotimes_{j^*=1}^{R}\hat{F}_{1,j^*}^z\right\rangle = \lim_{R\to\infty}\left\langle \bigotimes_{l=1}^{R}\tau_l^x\right\rangle = \lim_{R\to\infty}\left\langle \sigma_1^z\sigma_{R+1}^z\right\rangle. \end{aligned} \tag{5.12}$$

In the topologically-ordered phase, $g_0 < J$, the correlation function of σ_l^z exhibits long-range order. As a consequence $\Phi_1 = 0$, and $\Phi_2 \sim \left(1-\left(\frac{g_0}{J}\right)^2\right)^{\frac{1}{4}} \neq 0$. This implies that the T_1 and T_2 closed strings are condensed in contrast to the open

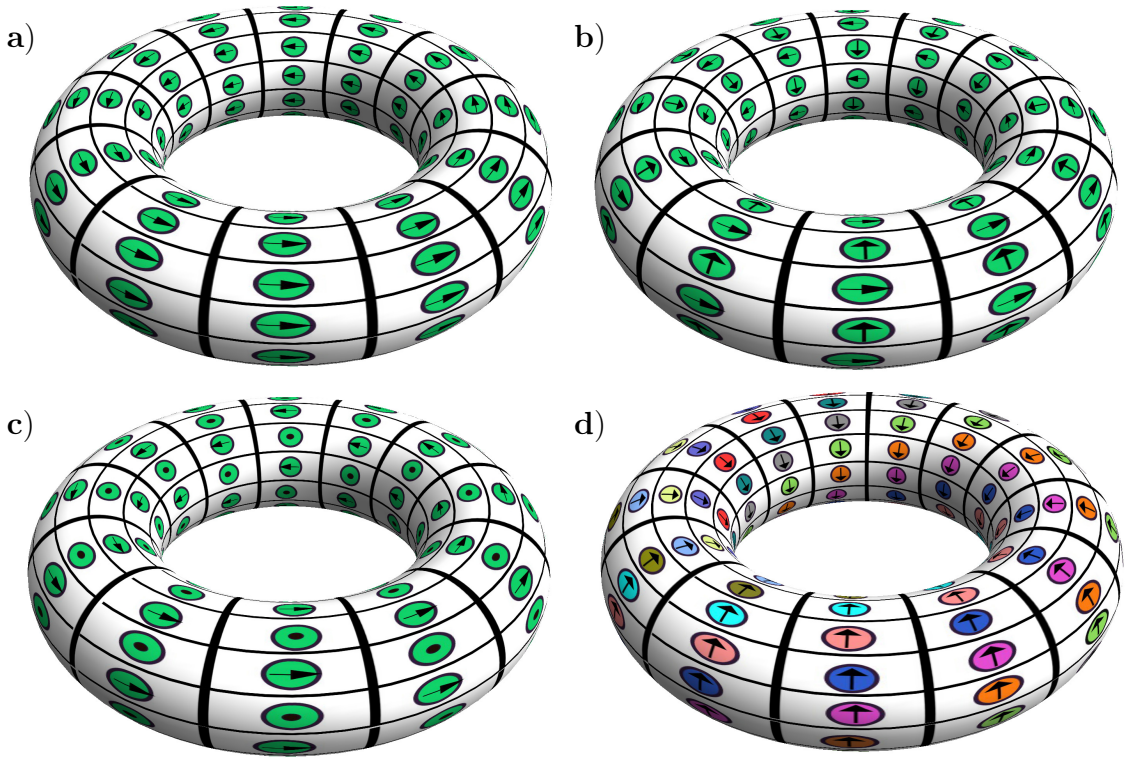

Figure 5.2.: Caricature of the spin textures in the Wen-plaquette model. (a) Depicts the topologically trivial spin texture on the torus ($g_0 \gg J$) in the absence of driving, (b) depicts the topological state in the case ($g_0 \ll J$), and (c) shows the novel driving-induced topological state (in the spin texture on the torus, the dots represent spins pointing to the positive z-direction). Finally, (d) depict the dual spin configuration depicted in 5.1 (d).

T_1 and T_2 strings. In the spin polarized phase, $g_0 > J$, a long-range order of the correlation function of τ_l^z indicates the condensation of open strings close to the TQPT, i.e., $\Phi_1 \sim \left(1 - \left(\frac{J}{g_0}\right)^2\right)^{\frac{1}{4}} \neq 0$ and $\Phi_2 = 0$.

Interestingly, using the duality between the Ising QPT and the Wen model we conclude that for $g_0 < J$ the paramagnetic phase of the τ-spin model (ferromagnetic phase of the σ-spin model) corresponds to the topologically-ordered (closed-string condensation) phase. Correspondingly, for $g_0 > J$ the ferromagnetic phase of the τ-spin model (paramagnetic phase of the σ-spin model) is dual to the spin-polarized phase of the Wen plaquette model (open string condensation) [108, 109, 112]. Figure 5.2 (a) depicts the spin-polarized phase of the Wen plaquette model on the torus and figure 5.2 (b) the topological phase. From this discussion we conclude that the global order parameters Φ_1 and Φ_2 are dual [108, 109], and therefore, to characterize the topological phase transition one of them is necessary. As a consequence of this, we consider generalized order parameters to characterize the topological phases, and we will not discuss about the order parameter characterizing the trivial phase.

5.2. The rotating wave approximation and the effective Hamiltonian approach

We perform here an alternative description of the system in the real lattice based on the RWA [52]. Let us perform a unitary transformation of Hamiltonian Eq. (5.1) into a convenient rotating frame via the unitary operator

$$\hat{U}_m(t) = \exp\left(\mathrm{i}\alpha_m(t)\sum_{i,j}\hat{X}_{i,j}\right), \tag{5.13}$$

where $\alpha_m(t) = m(\Omega/4)t + \frac{g_1}{\Omega}\sin\Omega t$. In the rotating frame the dynamics is governed by the Hamiltonian $\hat{H}_m(t) = [\hat{U}_m(t)]^\dagger \hat{\mathcal{H}} \hat{U}_m(t)$, where $\hat{\mathcal{H}} = \hat{H}(t) - \mathrm{i}\frac{\partial}{\partial t}$ is the Floquet Hamiltonian [50]. The explicit form of this operator is given by

$$\begin{aligned}
\hat{H}_m(t) \;=\; & -\delta^{(m)}\sum_{i,j}\hat{X}_{i,j} + \frac{J}{2}\sin[4\alpha_m(t)]\sum_{i,j}\hat{X}_{i,j}\hat{Y}_{i+1,j}\hat{X}_{i+1,j+1}\hat{Z}_{i,j+1} \\
& + \frac{J}{2}\sin[4\alpha_m(t)]\sum_{i,j}\hat{X}_{i,j}\hat{Z}_{i+1,j}\hat{X}_{i+1,j+1}\hat{Y}_{i,j+1} \\
& - \frac{J}{2}\left\{1+\cos[4\alpha_m(t)]\right\}\sum_{i,j}\hat{X}_{i,j}\hat{Y}_{i+1,j}\hat{X}_{i+1,j+1}\hat{Y}_{i,j+1} \\
& - \frac{J}{2}\left\{1-\cos[4\alpha_m(t)]\right\}\sum_{i,j}\hat{X}_{i,j}\hat{Z}_{i+1,j}\hat{X}_{i+1,j+1}\hat{Z}_{i,j+1},
\end{aligned} \tag{5.14}$$

where the detuning $\delta^{(m)} = g_0 - m(\Omega/4)$ describes how far the system is from resonance, and m is an integer that denotes the order of the multiphotonic resonance [50]. By using the identity Eq. (4.20), the Hamiltonian Eq. (5.14) can be written in the form

$$\hat{H}_m(t) = \sum_{n=-\infty}^{\infty} \hat{h}_n^{(m)} \exp\left(in\Omega t\right). \tag{5.15}$$

In analogy with the standard RWA of quantum optics, we obtain an approximate Hamiltonian to describe the mth resonance by neglecting all the terms in $\hat{H}_m(t)$ with oscillatory time-dependence: $\hat{H}_m(t) \approx \hat{h}_0^{(m)}$. This approximation is valid as long as the condition Eq. (4.22) holds [52].

Finally, we obtain the time-independent effective Hamiltonian

$$\begin{aligned}\hat{h}_0^{(m)} &= -\delta^{(m)} \sum_{i,j} \hat{X}_{i,j} - J_z^{(m)} \sum_{i,j} \hat{X}_{i,j}\hat{Y}_{i+1,j}\hat{X}_{i+1,j+1}\hat{Y}_{i,j+1} \\ &\quad - J_y^{(m)} \sum_{i,j} \hat{X}_{i,j}\hat{Z}_{i+1,j}\hat{X}_{i+1,j+1}\hat{Z}_{i,j+1} \\ &= -\delta^{(m)} \sum_{i,j} \hat{X}_{i,j} - J_z^{(m)} \sum_{i,j} \hat{F}_{i,j}^z - J_y^{(m)} \sum_{i,j} \hat{F}_{i,j}^y,\end{aligned} \tag{5.16}$$

where the parameters are the same that appear in Hamiltonian Eq. (4.23), $\hat{F}_{i,j}^y$ was defined in Eq. (5.2) and

$$\hat{F}_{i,j}^y = \hat{X}_{i,j}\hat{Z}_{i+1,j}\hat{X}_{i+1,j+1}\hat{Z}_{i,j+1} \tag{5.17}$$

corresponds to a driving-induced effective interaction which is absent in equilibrium [43]. This intuitive idea is reinforced when we remind that the topological phases of the undriven Wen plaquette model are closely related to the quantum phases of the Ising model. In the driven case, however, the Ising model Eq. (4.1) studied in Chapter 4 exhibits a novel phase [92]. We conclude therefore that the nonequilibrium QPT diagram depicted in Fig. 4.3 corresponds to the phase diagram of the TQPT in the driven Wen plaquette model. After the last discussion, a natural question arise: Does the effective Hamiltonian allow for novel topological phases, or the driving-induced phase is topologically trivial? To answer this question one should perform a description of the system based on the laboratory frame and cycle-averaged topological order parameters [107].

5.3. Floquet topological quantum phase transition

In the precedent chapters we have discussed extensively the intriguing aspects of criticality in conventional QPTs under the effect of monochromatic driving. In conventional QPT, i.e., within the Landau symmetry-breaking paradigm, the external

control induces effective interactions that lead to the existence of new quantum phases. In driven many-body systems, the periodicity in time induces the possibility to close the gap artificially in a controlled way, by tuning the parameters of the system around quantum resonances [43, 66, 92].

Rather recently, the topological charge of the Floquet Majorana fermions was defined in terms of the Floquet operator [114]. The influence of the external control on the topology of the system via geometric phases has also been explored [115, 116]. Additionally, by using intense circularly polarized light, a gap can be open in the Dirac cone, leading to a photoinduced dc Hall current in graphene [117]. Similarly, by using one-photon resonances, a trivial insulator can be driven into the topological phase, originating a Floquet topological insulator [19, 117].

We show in this section the external control induces a new topological phase, which is absent in the undriven WPM. To explore the topological nature of the quantum phases, we the calculate the Floquet-Chern numbers to characterize topological charges [118, 119].

In this section we focus on the calculation of global cycle-averaged expectation values in the negative-quasienergy Floquet state of the Wen-Plaquette model $|\Psi^{(-)}_{W,m},t\rangle = \bigotimes_{i^*=1}^{N}|\Psi^{(-)}_{m},t\rangle$, where $|\Psi^{(-)}_{m},t\rangle$ is negative-quasienergy Floquet state of one of the decoupled Ising chains, given by Eq. (4.35). We use this particular choice motivated by the fact that in the absence of driving, such a state corresponds to a topologically trivial spin texture (see Fig. 5.2 (a)) in the limit $g_0 \gg J$, and, in the dual picture of the σ-spins, corresponds to a tensor product of stationary paramagnetic states of the Hamiltonian Eq. (4.1) (in the case $g_1 = 0$) with all the spin polarized along the x axis

$$|\Psi^{(-)}_{W,m},t\rangle = \exp(-\mathrm{i}N^2E^{(-)}_{G}t)\bigotimes_{i^*=1}^{N}\bigotimes_{k\geq 0}|0_{-k},0_k\rangle. \tag{5.18}$$

where $E^{(-)}_{G}$ is the ground-state energy of the undriven Ising model given by Eq. (4.5).

5.3.1. Floquet topological order from long-range magnetic order in the dual Ising model

We focus here on the calculation of cycle-averaged global order parameters defined along the diagonal string of the dual lattice $(i^*,j^*) = (1,l)$, where l is a positive integer number running from 1 to R, in the limit when $R \to \infty$. Our definition of $\bar{\Phi}_2$ is a generalization to driven quantum systems of the global order parameters defined in equilibrium [108, 109]. However, the existence of $\bar{\Phi}_3$ has no analogue in equilibrium and a nonvanishing value of it would give rise to a topological configuration induced entirely by the external control and with a different topological charge.

By using the spin dualities Eq. (5.7) and Eq. (5.10) we define

$$\bar{\Phi}_2 = \lim_{R\to\infty} \frac{1}{T}\int_0^T \left\langle \bigotimes_{j^*=1}^{R} \hat{F}^z_{1,j^*} \right\rangle \, dt = \lim_{R\to\infty} \frac{1}{T}\int_0^T \left\langle \sigma^z_1 \sigma^z_{1+R} \right\rangle \, dt,$$
$$\bar{\Phi}_3 = \lim_{R\to\infty} \frac{1}{T}\int_0^T \left\langle \bigotimes_{j^*=1}^{R} \hat{F}^y_{1,j^*} \right\rangle \, dt = \lim_{R\to\infty} \frac{1}{T}\int_0^T \left\langle \sigma^y_1 \sigma^y_{1+R} \right\rangle \, dt. \tag{5.19}$$

Interestingly, the cycle-averaged order parameters correspond to cycle-averaged correlation functions of the dual one-dimensional driven Ising model Eq. (4.1). Such correlation functions characterize the long-range magnetic order under the effect of external driving. One can calculate the cycle-averaged nonequilibrium spin correlation functions in terms of the well-known results for the XY model [96, 97, 113]. We can write explicitly (as we show in Appendix F) the topological order parameters as follows:

$$\bar{\Phi}_2 = \frac{2}{J}\lim_{R\to\infty}[J_z^{(m)}\rho_{zz}(R) + J_y^{(m)}\rho_{yy}(R)],$$
$$\bar{\Phi}_3 = \frac{2}{J}\lim_{R\to\infty}[J_z^{(m)}\rho_{yy}(R) + J_y^{(m)}\rho_{zz}(R)], \tag{5.20}$$

where $J_z^{(m)}$, $J_y^{(m)}$ are the effective anisotropies in the rotating frame defined in Sec. 4.3 of chapter 4. Furthermore, for $\alpha \in \{y, z\}$ we define $\rho_{\alpha\alpha}(R) = \left\langle \chi_m^{(-)} \left| \sigma_1^\alpha \sigma_{1+R}^\alpha \right| \chi_m^{(-)} \right\rangle$ to be spin correlation functions calculated in the rotating frame (see Appendix F), where

$$|\chi_m^{(-)}\rangle = \bigotimes_{k\geq 0} |\chi_{k,m}^{(-)}\rangle, \tag{5.21}$$

and $|\chi_{k,m}^{(-)}\rangle$ is given by Eq. (4.29).

We have that $\bar{\Phi}_2 = \bar{\Phi}_3 = 0$ in the topologically trivial phase $|\delta^{(m)}| > J$ and for $|\delta^{(m)}| < J$

$$\lim_{R\to\infty}\rho_{zz}(R) = \begin{cases} \frac{2(|\gamma^{(m)}|)^{1/2}}{1+|\gamma^{(m)}|}\left(1-\left(\frac{\delta^{(m)}}{J}\right)^2\right)^{1/4} & \gamma^{(m)} > 0 \\ 0 & \gamma^{(m)} < 0 \end{cases},$$
$$\lim_{R\to\infty}\rho_{yy}(R) = \begin{cases} 0 & \gamma^{(m)} > 0 \\ \frac{2(|\gamma^{(m)}|)^{1/2}}{1+|\gamma^{(m)}|}\left(1-\left(\frac{\delta^{(m)}}{J}\right)^2\right)^{1/4} & \gamma^{(m)} < 0 \end{cases}, \tag{5.22}$$

where $\gamma^{(m)} = (-1)^m \mathcal{J}_m\left(\frac{4g_1}{\Omega}\right)$ is the anisotropy parameter. As a limiting case, our description recovers the physics of the undriven model ($g_1 = 0$) in the particular case

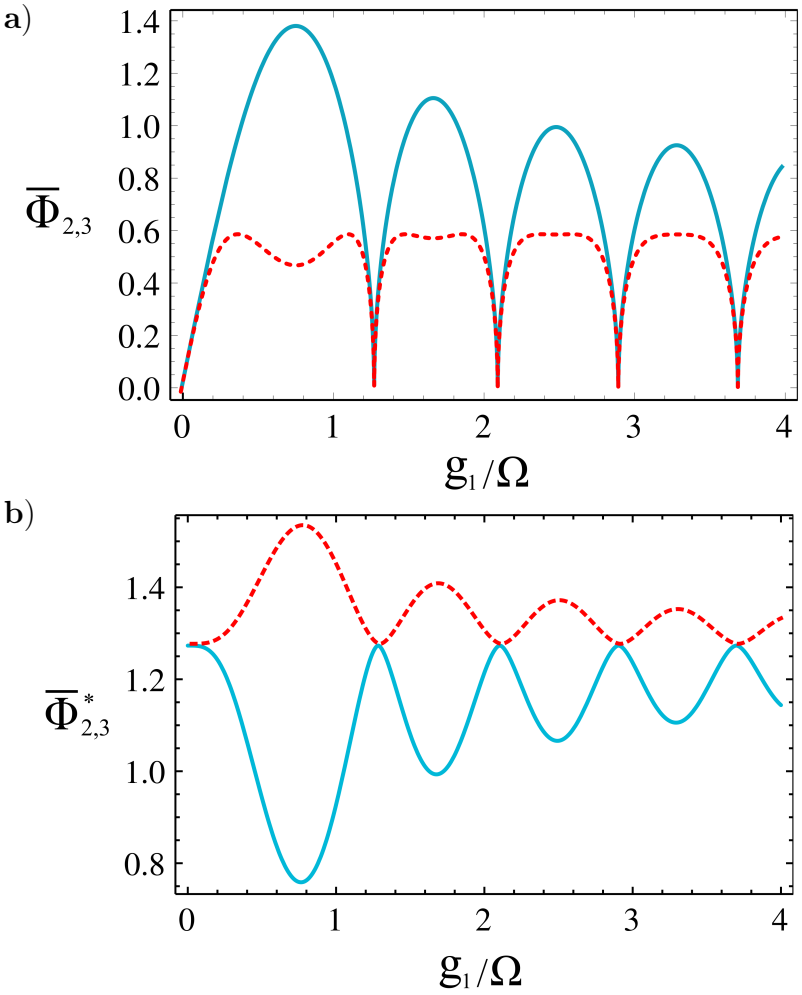

Figure 5.3.: Cycle-averaged order parameters. (a) Depicts the cycle-averaged topological order parameters based on long-range magnetic order. The blue curve (continuous line) represents the order parameter $\bar{\Phi}_2$, and the red curve (dotted line) the novel order parameter $\bar{\Phi}_3$. (b) Shows the cycle-averaged topological order parameters based on short-range magnetic order. The blue curve (continuous line) represents the order parameter $\bar{\Phi}^*_3$, and the red curve (dotted line) the novel order parameter $\bar{\Phi}^*_2$. At the anisotropic transition lines of the dual model (see Fig. 4.3), the short-range correlations coincide. We consider the plot on exact resonance $\delta^{(m)} = 0$ for $m = 2$ and we consider $J/\Omega = 0.01$

$m = 0$, where $\delta^{(0)} = g_0$, $\gamma^{(0)} = 1$, $J_z^{(0)} = J$, and $J_y^{(0)} = 0$. Therefore, we obtain that the nonlocal order parameters satisfy $\bar{\Phi}_2 = \Phi_2$ and $\bar{\Phi}_3 = 0$. We plot the dependence of the order parameters along the ladder of topological phases (ferromagnetic phases FMZ and FMY from the dual Ising model) in Fig. 5.3 (a).

5.3.2. Floquet topological order from short-range magnetic order in the dual Ising model

An alternative way to define global order parameters for the Wen plaquete model is to redefine the limit in Eq. (5.19) by considering $R = N - 1$, where N is the length of the dual Ising chains. In contrast to the previous procedure used to calculate the cycle-averaged order parameters, this special case gives rise to a different definition based on the short-range magnetic order. In particular, by using this procedure we obtain

$$\begin{aligned}
\bar{\Phi}_2^* &= \lim_{N\to\infty} \frac{1}{T}\int_0^T \left\langle \bigotimes_{j^*=1}^{N-1} \hat{F}^z_{1,j^*} \right\rangle \, dt = \frac{1}{T}\int_0^T \langle \sigma_1^z \sigma_2^z \rangle \, , \\
\bar{\Phi}_3^* &= \lim_{N\to\infty} \frac{1}{T}\int_0^T \left\langle \bigotimes_{j^*=1}^{N-1} \hat{F}^y_{1,j^*} \right\rangle \, dt = \frac{1}{T}\int_0^T \langle \sigma_1^y \sigma_2^y \rangle \, ,
\end{aligned} \tag{5.23}$$

where we have used translational invariance and the periodic boundary conditions. In Appendix F we show that the order parameters can be written as follows

$$\begin{aligned}
\bar{\Phi}_2^* &= \frac{2}{J}[J_z^{(m)} \rho_{zz}^* + J_y^{(m)} \rho_{yy}^*], \\
\bar{\Phi}_3^* &= \frac{2}{J}[J_z^{(m)} \rho_{yy}^* + J_y^{(m)} \rho_{zz}^*],
\end{aligned} \tag{5.24}$$

where

$$\begin{aligned}
\rho_{zz}^* &= \int_0^\pi \frac{dk}{\pi} \frac{1}{\varepsilon_{k,m}} - \frac{2J_y^{(m)}}{J} \int_0^\pi \frac{dk}{\pi} \frac{\sin^2 k}{\varepsilon_{k,m}}, \\
\rho_{yy}^* &= \int_0^\pi \frac{dk}{\pi} \frac{1}{\varepsilon_{k,m}} - \frac{2J_z^{(m)}}{J} \int_0^\pi \frac{dk}{\pi} \frac{\sin^2 k}{\varepsilon_{k,m}}.
\end{aligned} \tag{5.25}$$

In the last equations $\varepsilon_{k,m}$ is the quasienergy dispersion defined in Eq. (4.27). On exact resonance, i.e., when $\delta^{(m)} = 0$, we obtain

$$\begin{aligned}
\bar{\Phi}_2^* \;=\; & \frac{4\left[1 + \left(\gamma^{(m)}\right)^2\right]}{\pi\left[1 - \left(\gamma^{(m)}\right)^2\right]} E\left[1 - \left(\gamma^{(m)}\right)^2\right] \\
& - \frac{8\left(\gamma^{(m)}\right)^2}{\pi\left[1 - \left(\gamma^{(m)}\right)^2\right]} K\left[1 - \left(\gamma^{(m)}\right)^2\right]
\end{aligned} \tag{5.26}$$

and

$$\bar{\Phi}_3^* = \frac{4}{\pi} E\left[1 - \left(\gamma^{(m)}\right)^2\right], \tag{5.27}$$

where $K[z]$ and $E[z]$ are the complete elliptic integrals of the first and second kind [48], respectively. We plot the dependence of the order parameters along the ladder of topological phases (ferromagnetic phases FMZ and FMY from the dual Ising model) in Fig. 5.3 (b).

5.3.3. The Floquet-Chern Number

In this section we calculate explicitly the Chern numbers that characterize the different topological phases of Ac-driven Wen plaquette model Hamiltonian Eq. (5.1). To carry out this calculation we focus on the dynamics in the rotating frame and perform the rotating wave approximation, this implies that in the rotating frame, the dynamics is governed by Hamiltonian Eq. (5.16). Under the duality transformations Eqs. (5.7) and (5.10) is possible to write

$$\hat{H}_m^{\sigma}(t) \approx \hat{h}_0^{(\sigma,m)} = \sum_{i^*=1}^{N} h_{i^*,0}^{(\sigma,m)} = \sum_{\tilde{k},k\geq 0} \hat{h}_{\tilde{k},k}^{(\sigma,m)}, \tag{5.28}$$

where $\hat{h}_0^{(\sigma,m)}$ is the effective Hamiltonian Eq. (5.16) in the dual picture of the σ-spins, $h_{i^*,0}^{(\sigma,m)}$ is the effective Hamiltonian Eq. (4.23), and $\hat{h}_{\tilde{k},k}^{(\sigma,m)}$ the corresponding effective Hamiltonian in the reciprocal lattice Eq. (4.24) discussed in Sec. 4.3 of Chap. 4.3. The matrix representation of $\hat{h}_{\tilde{k},k}^{(\sigma,m)}$ in the Nambu subspace is given by

$$h_{\tilde{k},k}^{(\sigma,m)} = \begin{pmatrix} 2\delta^{(m)} - 2\omega_k & (-1)^m \Delta_k \mathcal{J}_m(\frac{4g_1}{\Omega}) \\ (-1)^m \Delta_k \mathcal{J}_m(\frac{4g_1}{\Omega}) & -2\delta^{(m)} \end{pmatrix}, \tag{5.29}$$

where $\omega_k = 2J\cos k$, and $\Delta_k = 2J\sin k$. In terms of the effective Anderson pseudospin vector $\boldsymbol{d}_{\tilde{k},k}^{(m)} = ((-1)^m \Delta_k \mathcal{J}_m(\frac{4g_1}{\Omega}), 0, 2\delta^{(m)} - \omega_k)$, the Bogoliubov Hamiltonian Eq. (5.29) can be alternatively written as $h_{\tilde{k},k}^{(\sigma,m)} = -\omega_k \mathbb{1}_{\tilde{k},k} + \boldsymbol{d}_{\tilde{k},k}^{(m)} \cdot \boldsymbol{\sigma}_{\tilde{k},k}$, where $\mathbb{1}_{\tilde{k},k}$ is the identity operator and $\boldsymbol{\sigma}_{\tilde{k},k} = (\sigma_{\tilde{k},k}^x, \sigma_{\tilde{k},k}^y, \sigma_{\tilde{k},k}^z)$ is a vector of Pauli operators acting on the Nambu subspace.

Now let us define the Gauss map $\hat{\boldsymbol{d}}^{(m)} : T^2 \longmapsto S^2$ from the two-dimensional torus $T^2 = S^1 \times S^1$ into the sphere S^2 similarly to Refs. [19, 118, 119]

$$\hat{\boldsymbol{d}}_{\tilde{k},k}^{(m)} = \frac{\boldsymbol{d}_{\tilde{k},k}^{(m)}}{\|\boldsymbol{d}_{\tilde{k},k}^{(m)}\|} = (\sin\theta\cos\phi_{k,m}, \sin\theta\sin\phi_{k,m}, \cos\theta), \tag{5.30}$$

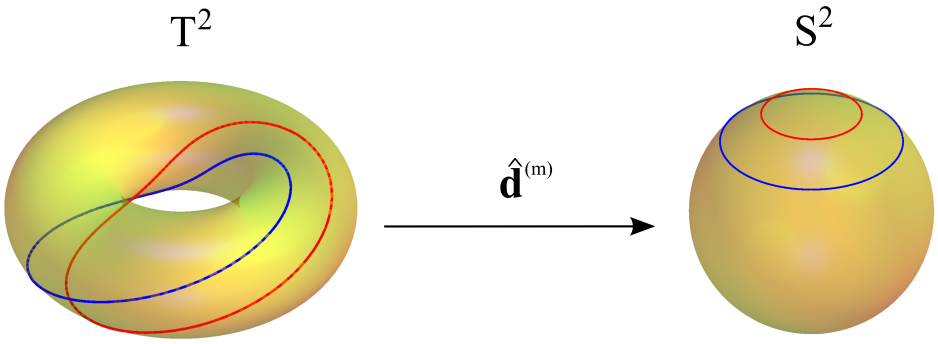

Figure 5.4.: Mapping from two "leaves" of the foliation on the torus on two circles over the sphere

where we have used spherical coordinates and the Bogoliubov angle $\phi_{k,m}$ is defined in Eq. (4.30). Figure 5.4 depicts the Gauss map and two FBZ of the Ising chains being mapped onto circles on the sphere. Following a similar method to Ref. [19], we define the Floquet-Chern number as

$$C_{\mathrm{F}} = \frac{1}{4\pi}\int_{T^2} \sin\theta \; d\theta \; d\phi_{k,m} = \frac{1}{2\pi}\int_0^{\pi} \; d\phi_{k,m}, \tag{5.31}$$

The Floquet-Chern number C_F counts the number of times that the Gauss map $\hat{\boldsymbol{d}}^{(m)}$ wraps the unit sphere as $(\tilde{k}, k)$ wraps around the entire FBZ in quasimomentum space—which in this case is topologically equivalent to T^2. Based on Eq. (5.31) we find that the Chern number can be $C_{\mathrm{F}} = 0$, $C_{\mathrm{F}} = 1$ and $C_{\mathrm{F}} = -1$ for the paramagnetic phase, the ferromagnetic phase FMZ, and the ferromagnetic phase FMY respectively. Interestingly, in the absence of driving, $C_{\mathrm{F}} = 0$ characterizes the trivial phase, and $C_{\mathrm{F}} = 1$ the topological phase. Therefore, we conclude that the driving induces a topologically-nontrivial configuration, i.e., with Chern number $C_{\mathrm{F}} = -1$ which cannot be generated from continuous deformations of the undriven phases. Geometrically, the Chern number formula given in Eq. (5.31) corresponds to the winding number of the Anderson pseudospin vector restricted to a "leave" of the foliation of the torus, such a "leave" corresponds to the FBZ in quasimomentum space (topologically equivalent to a circle S^1) of a particular Ising chain as can be seen in Figs. 5.1 (d) and 5.2 (d). Figure 5.5 depicts the geometry of the pseudospin Anderson vector and the intepretation of the Chern-Floquet number in terms of the direction of rotation.

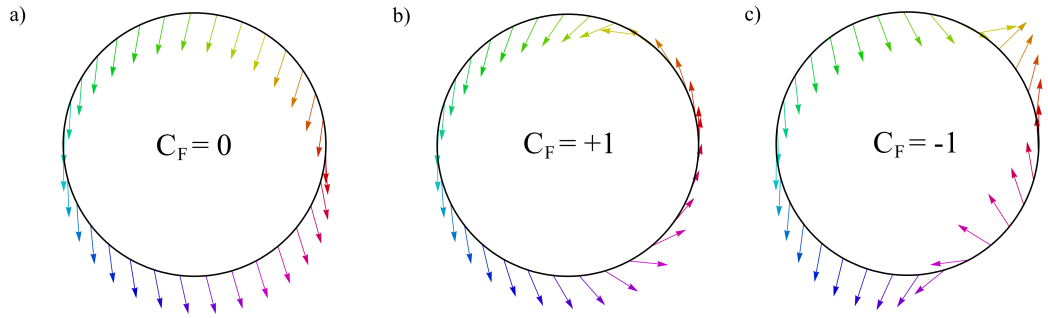

Figure 5.5.: Winding of the pseudospin Anderson vector restricted to a "leave" of the foliation on the torus.

5.4. Experimental realization

Recently, a realization of quantum magnets in a system of cold atoms placed in an optical lattice has been suggested [34, 35, 36], to allow the implementation of the spin-1/2 Kitaev model on a hexagonal lattice. Importantly, further investigation in spin systems with topological order [6] will have a huge potential for applications in quantum information as topologically-protected qubits. By controlling the tunneling and the self-interaction strength of the ensemble of cold atoms, simulation of anisotropic Heisenberg-like interactions of the effective spin system on a honeycomb lattice is possible [34]. A promising experimental realization of the driven Wen-plaquette model could be achievable by using a Rydberg atom quantum simulator [36]. To simulate it is necessary to construct a quantum circuit consisting of nonlocal gates that encode the interactions of the effective system.

6. Conclusion and outlook

This thesis focuses on the description of quantum criticality under the effect of monochromatic driving in $(d+1)$-dimensional systems ranging from the Dicke and LMG models in $d=0$, the transverse Ising model in $d=1$, and the Wen-plaquette model in $d=2$. We have developed a method to describe QPTs in these models based on effective Hamiltonians, which allow us to study driving-induced effective interactions. Our methodology is potentially interesting in the context of quantum simulation with cold atoms. We have investigated systems which exhibit second-order QPTs in the absence of driving. When the external control is close to resonance with the excitation energies of the undriven system, novel quantum phases are generated as a result of the effective interactions.

In the study of the Dicke and LMG models, we have defined a quasienergy landscape to characterize the stable configurations, the number of which increases with the amplitude of the external driving. As the stable configurations are macroscopically separated, tunneling between minima is suppressed in the thermodynamic limit. For the driven Dicke model, we show how the "no-go theorem" is circumvented in cavity QED. Further studies may reveal the relation between Berry phase and driving-induced multistability.

We have shown the existence of anisotropic transitions in the driven Ising model which are absent in equilibrium. We have discussed how the quantum phases correspond to states which are synchronized with the driving. Based on this fact, we have defined cycle-averaged quantities to describe critical signatures in nonequilibrium. In particular, at the critical lines—similarly to the usual undriven second-order QPTs—the cycle-averaged energy exhibits nonanalyticities in the second derivative. A next step in further investigations is the detailed study of the multicritical points and critical exponents.

In the context of TQPT, we have studied the driven version of the Wen-Plaquette model. We have shown the existence of a new nontrivial topological phase and introduced a nonlocal cycle-averaged order parameter to describe it. It will be interesting to understand the braiding of anyonic excitations under the effect of driving and investigate the driven versions of paradigmatic models such as the toric code and Kitaev honeycomb lattice.

Abbreviations

DM Dicke Model

QPT Quantum Phase Transition

QED Quantum Electrodynamic

RWA Rotating wave approximation

LMG Lipkin-Meshkov-Glick

LQE Lowest quasienergy

FBZ First Brillouin zone

BdG Bogoliubov-de Gennes

FBdG Floquet-Bogoliubov-de Gennes

CDT Coherent destruction of tunneling

TQPT Topological quantum phase transition

TQFT Topological quantum field theory

WPM Wen Plaquette Model

Appendix

A. Background to Floquet Theory

In this appendix we concisely summarize the more important aspects of Floquet theory for time-periodic Hamiltonians [50]. Based on this analysis we describe the physical interpretation of the effective Hamiltonian approach that we use in this thesis to describe AC-driven QPTs by means of the RWA [52]. Finally, we discuss the relation between RWA and Floquet theory.

A.1. The Floquet Hamiltonian

In this thesis we are interested in the analysis of periodically driven systems, which are described by a time-periodic Hamiltonian

$$\hat{H}(t+T) = \hat{H}(t) \ , \tag{A.1}$$

where $T = 2\pi/\Omega$ is the period, and Ω is the angular frequency of the external driving. In this case, the symmetry of the Hamiltonian under discrete time translations enables us to write the solution of the Schrödinger equation as

$$|\Psi(t)\rangle = \sum_\alpha a_\alpha |\Psi_\alpha(t)\rangle = \sum_\alpha a_\alpha e^{-\mathrm{i}\varepsilon_\alpha t}|\Phi_\alpha(t)\rangle \ . \tag{A.2}$$

The states $|\Psi_\alpha(t)\rangle = e^{-\mathrm{i}\varepsilon_\alpha t}|\Phi_\alpha(t)\rangle$ are the so-called Floquet states, $|\Phi_\alpha(t+T)\rangle = |\Phi_\alpha(t)\rangle$ are the Floquet modes, and ε_α are the quasienergies, which are unique up to integer multiples of Ω. The Floquet modes satisfy the eigenvalue equation

$$\hat{\mathcal{H}}|\Phi_\alpha(t)\rangle = \varepsilon_\alpha|\Phi_\alpha(t)\rangle \ , \tag{A.3}$$

where

$$\hat{\mathcal{H}} = \hat{H}(t) - \mathrm{i}\frac{\partial}{\partial t} \tag{A.4}$$

is the Floquet Hamiltonian. We immediately notice that the modified Floquet modes

$$|\Phi_{\alpha n}(t)\rangle = e^{\mathrm{i}n\Omega t}|\Phi_\alpha(t)\rangle \ , \tag{A.5}$$

with n being an integer number denoting the Fourier index, are eigenvalues of the Floquet Hamiltonian Eq. (A.4), but with the shifted quasienergy $\varepsilon_{\alpha n} = \varepsilon_\alpha + n\Omega$. As a consequence, the set of eigenvalues $\{\varepsilon_\alpha\}_{\alpha\in\Gamma}$ (Γ is a set of indices that labels the quasienergies) can be mapped into a first Brillouin zone (FBZ) in the quasienergy space, obeying $-\Omega/2 \leq \varepsilon_\alpha \leq \Omega/2$.

It is convenient to introduce the extended Hilbert space $\mathscr{H} = \mathscr{R} \otimes \mathscr{T}$, where $\mathscr{R}$ is the Hilbert space of the square integrable functions on configuration space, and $\mathscr{T}$ is the set of time-periodic functions with period $T = 2\pi/\Omega$. In the extended Hilbert space, the quantum state of the system can be expanded as follows

$$|\Psi(t)\rangle = \sum_{\beta,n} c_{\beta,n} |\beta\rangle \otimes |n\rangle, \tag{A.6}$$

where $|\beta\rangle$ is a complete basis for $\mathscr{R}$ and the Fourier states $|n\rangle$ constitute a basis for $\mathscr{T}$ such that $\langle t|n\rangle = e^{in\Omega t}$. Formally, in the extended Hilbert space $\mathscr{H}$, one can define the conjugate variables $\hat{t}$ and $\hat{E} = \mathrm{i}\partial/\partial t$, such that $[\hat{E}, \hat{t}\,] = \mathrm{i}$, as in reference [95]. The operator $\hat{E}$ is diagonal in the basis of Fourier states $\hat{E}|n\rangle = -n|n\rangle$, and $\hat{t}$ is diagonal in the continuous basis $\hat{t}|t\rangle = t|t\rangle$. By using this formalism, one can define the Fourier translation operator $\hat{K}_\Omega = e^{\mathrm{i}\Omega\hat{t}} : \mathscr{T} \mapsto \mathscr{T}$, such that

$$\begin{aligned} \hat{K}_\Omega|n\rangle &= |n+1\rangle, \\ \hat{K}_\Omega|t\rangle &= e^{\mathrm{i}\Omega t}|t\rangle. \end{aligned} \tag{A.7}$$

Therefore, the action of $\hat{K}_\Omega$ allows us to couple sectors with different Fourier indices n in the extended Hilbert space $\mathscr{H}$, such a interpretation is very useful in the context of RWA.

A.2. Floquet operator

For periodically driven systems it is useful, from the numerical point of view, to use an alternative method to calculate the Floquet states and quasienergies. The method is based on the fact that the Floquet states are eigenstates of the Floquet operator

$$\hat{\mathcal{F}} = \hat{U}(T,0) = \hat{T}\exp\left[-\mathrm{i}\int_0^T \hat{H}(t)\,dt\right], \tag{A.8}$$

where $\hat{T}$ is the time-ordering operator, and $\hat{U}(T,0)$ is the evolution operator in one period of the driving, which can be obtained by numerical integration of the Schrödinger equation. The Floquet operator is a unitary operator, i.e., the eigenvalues must be unimodular complex numbers

$$\hat{\mathcal{F}}|\Phi_\alpha(0)\rangle = e^{-\mathrm{i}\varepsilon_\alpha T}|\Phi_\alpha(0)\rangle\,, \tag{A.9}$$

where the phases ε_α are exactly the set of Floquet quasienergies introduced above, and the eigenvectors correspond to the Floquet states evaluated at the initial time. The Floquet operator description gives us the possibility to perform a stroboscopic observation of the system at times nT, where n is a natural number. In one period, the evolution of the initial quantum state $|\Psi(0)\rangle$ is given by

$$\hat{\mathcal{F}}|\Psi(0)\rangle = |\Psi(T)\rangle \ , \tag{A.10}$$

which can be generalized to

$$\hat{\mathcal{F}}^n|\Psi(0)\rangle = |\Psi(nT)\rangle \ . \tag{A.11}$$

A.3. Floquet theory and RWA

In this section we establish the relation between Floquet theory and RWA. The principal ingredient of this analysis relies on the transformation into a convenient rotating frame via a unitary transformation $\hat{U}_m(t)$. In the rotating frame, the dynamics is governed by the Hamiltonian

$$\hat{H}_m(t) = \hat{U}_m^\dagger(t)\hat{\mathcal{H}}\hat{U}_m(t), \tag{A.12}$$

where $\hat{\mathcal{H}}$ is the Floquet Hamiltonian Eq. (A.4). In the extended Hilbert space $\mathscr{H}$, the Hamiltonian Eq. (A.12) can be decomposed as a formal Fourier series

$$\hat{H}_m(t) = \sum_{n=-\infty}^{\infty} \hat{h}_n^{(m)} \hat{K}_\Omega^n = \sum_{n=-\infty}^{\infty} \hat{h}_n^{(m)} e^{\mathrm{i}n\Omega\hat{t}}, \tag{A.13}$$

where $\hat{h}_n^{(m)}$ is an operator acting on $\mathscr{R}$. For parameters close to a m-photon resonance, we can perform the RWA by neglecting all the terms that couple different Fourier states in the expansion, i.e., by considering $\hat{H}_m(t) \approx \hat{h}_0^{(m)}$. In this thesis, we consider $\hat{h}_0^{(m)}$ as our effective Hamiltonian, because it resembles the behavior of a time-independent Hamiltonian, however, with effective interactions which are absent in equilibrium. Interestingly, under RWA, $\hat{h}_0^{(m)}$ and the Floquet Hamiltonian Eq. (A.4) are isospectral operators, and their eigenvalues correspond to the quasienergies. Let us assume the eigenvalue problem $\hat{h}_0^{(m)}|\tilde{\phi}_{\alpha,m}\rangle = \varepsilon_{\alpha,m}|\tilde{\phi}_{\alpha,m}\rangle$. To obtain the eigenvectors of the Floquet Hamiltonian (A.4) for parameters close to a m-photon resonance, one should apply a unitary transformation back into the laboratory frame

$$|\tilde{\Phi}_{\alpha,m}(t)\rangle = \hat{U}_m(t)|\tilde{\phi}_{\alpha,m}\rangle. \tag{A.14}$$

In the next appendix we discuss the relation between RWA and Floquet theory in a very instructive particular example.

B. The periodically-driven two-level system

Our aim in this section is to apply the formalism discussed in the last section to one particular example. Therefore, we focus here on the periodically driven two-level system [95]

$$\hat{H}(t) = -\varepsilon(t)\sigma_z - \Delta\sigma_x, \tag{B.1}$$

where $\varepsilon(t) = \varepsilon_0 + \varepsilon_1 \cos\Omega t$ corresponds to a time-periodic asymmetry, and Δ is the tunneling amplitude. In the laboratory frame, for a given n, the monochromatic driving induces transitions between Fourier states $|n\rangle$ and $|n \pm 1\rangle$ in $\mathscr{H}$, as can be seen from the identity $2\cos\Omega t = \langle t|\hat{K}_\Omega + \hat{K}_\Omega^\dagger|t\rangle$.

In the absence of driving, the system is exactly solvable, and is characterized by the eigenenergies $E^{(\pm)} = \pm\sqrt{\varepsilon_0^2 + \Delta^2}$. Under the effect of driving, multiphoton transitions can occur when the relation $E^{(+)} - E^{(-)} = m\Omega$ is satisfied, where m is an integer labeling the number of photons involved in the transition. Such a condition implies a crossing of the energy spectrum of the two-level system, when the energies $E^{(\pm)}$ are folded into the FBZ in energy space, because $m\Omega \equiv 0$ modulus Ω. In the case of weak tunneling amplitude $\Delta \ll \Omega$, the resonance condition reads $\varepsilon_0 \approx m\Omega/2$. In the next section, we perform the RWA for parameters close to a multiphoton resonance.

B.1. The RWA and the effective Hamiltonian

Now, let us consider a transformation into the rotating frame via the unitary operator

$$\hat{U}_m(t) = \exp(\mathrm{i}\alpha_m(t)\sigma_z), \tag{B.2}$$

where $\alpha_m(t) = \frac{m\Omega t}{2} + \frac{\varepsilon_1}{\Omega}\sin\Omega t$. In the rotating frame the, quantum evolution is governed by the Hamiltonian

$$\hat{H}_m(t) = -\delta^{(m)}\sigma_z - \Delta\left\{\sigma_x \cos 2\alpha_m(t) + \sigma_y \sin 2\alpha_m(t)\right\}, \tag{B.3}$$

where $\delta^{(m)} = \varepsilon_0 - m\Omega/2$ is the detuning from resonance. By using the identity Eq. (4.20), the Hamiltonian Eq. (B.3) can be written in the form of Eq. (A.13). In analogy with the standard RWA of quantum optics, we obtain an approximate Hamiltonian to describe the mth resonance by neglecting all the terms in $\hat{H}_m(t)$ with oscillatory time-dependence: $\hat{H}_m(t) \approx \hat{h}_0^{(m)}$. This approximation is valid as long as the condition

$$\delta^{(m)}, \Delta\mathcal{J}_m\left(\frac{2\varepsilon_1}{\Omega}\right) \ll \Omega \tag{B.4}$$

holds [52]. The effective Hamiltonian reads

$$\hat{h}_0^{(m)} = -\delta^{(m)}\sigma_z - (-1)^m\Delta\mathcal{J}_m\left(\frac{2\varepsilon_1}{\Omega}\right)\sigma_x, \tag{B.5}$$

where we have use the property $\mathcal{J}_{-l}(z) = (-1)^l \mathcal{J}_l(z)$ of the Bessel functions [48]. The quasienergies of the system are given by

$$\tilde{\varepsilon}_{\pm,m} = \pm\sqrt{[\delta^{(m)}]^2 + \left[\Delta \mathcal{J}_m\left(\frac{2\varepsilon_1}{\Omega}\right)\right]^2}. \tag{B.6}$$

It is tempting to define the Floquet modes as $|\tilde{\Phi}_{\pm,m}(t)\rangle = \hat{U}_m(t)|\phi_{\pm,m}\rangle$. Under this definition, however, we have the relation $|\tilde{\Phi}_{\pm,m}(T)\rangle = \hat{U}_m(T)|\phi_{\pm,m}\rangle = \exp(\mathrm{i}m\pi\sigma_z)|\phi_{\pm,m}\rangle$, which implies that for even m, the eigenvectors of the Floquet Hamiltonian Eq. (A.4) are periodic, whereas for odd m they are antiperiodic. A solution to this problem is to define the Floquet modes as $|\Phi_{\pm,m}(t)\rangle = e^{\frac{\mathrm{i}m\Omega t}{2}}\hat{U}_m(t)|\phi_{\pm,m}\rangle$ with the corresponding shifted quasienergies

$$\varepsilon_{\pm,m} = \pm\sqrt{[\delta^{(m)}]^2 + \left[\Delta \mathcal{J}_m\left(\frac{2\varepsilon_1}{\Omega}\right)\right]^2} + \frac{m\Omega}{2}. \tag{B.7}$$

B.2. Coherent destruction of tunneling in a nutshell

In this section we discuss briefly the concept of coherent destruction of tunneling (CDT) [99, 100]. At the beginning of this appendix we discussed the condition under which a multiphoton resonance can occur in the absence of driving. When the external control is switched on, however, the degeneracy is lifted in general, and there are Rabi oscillations between the two quasienergy eigenstates $|\Phi_{\pm,m}(t)\rangle$ with frequency $\omega_m = \varepsilon_{+,m} - \varepsilon_{-,m}$. A seminal result of the theory of externally-driven quantum systems is that, as a consequence of a generalized parity in the extended Hilbert space $\mathscr{H}$, under the effect of periodic driving the tunneling between quasienergy eigenstates can be slowed down or totally suppressed in a perfect coherent way, a phenomenon commonly referred to as coherent destruction of tunneling (CDT) [99, 100]. In particular, starting from the analytical results obtain from RWA, we can observe that on resonance, i.e., when $\delta^{(m)} = 0$, the Rabi frequency ω_m vanishes when the system parameters are tuned up such that the condition $\mathcal{J}_m\left(\frac{2\varepsilon_1}{\Omega}\right) = 0$ is satisfied [95], which implies a suppression of the Rabi oscillations related to a crossing of the quasienergies $\varepsilon_{+,m}$ and $\varepsilon_{-,m}$. Therefore, there is a dynamical freezing in the two-level system dynamics as a consequence of the external control.

C. Description of the driven Ising model for finite size

In this appendix we introduce the fundamental tools used in the solution of the Ising model following the methods and the notation of reference [12].

Let us consider the Hamiltonian Eq. (4.1) in the case of even number of lattice sites N. For convenience, we use the Jordan-Wigner representation of the Pauli matrices

$$\begin{aligned}\sigma_j^x &= 1 - 2\hat{c}_j^\dagger \hat{c}_j, \\ \sigma_j^y &= -i(\hat{c}_j^\dagger - \hat{c}_j) \prod_{l=1}^{j-1} (1 - 2\hat{c}_l^\dagger \hat{c}_l), \\ \sigma_j^z &= (\hat{c}_j^\dagger + \hat{c}_j) \prod_{l=1}^{j-1} (1 - 2\hat{c}_l^\dagger \hat{c}_l). \end{aligned} \tag{C.1}$$

Under this representation of the angular momentum algebra, the parity operator Eq. (4.2) acquires the form

$$\hat{\Pi} = \bigotimes_{i=1}^{N} \sigma_i^x = \prod_{j=1}^{N} (1 - 2\hat{c}_j^\dagger \hat{c}_j). \tag{C.2}$$

Using this parity operator we are able to define projectors onto the subspaces with even (+) and odd (−) number of fermionic quasiparticles as follows

$$\hat{\mathcal{P}}_\pm = \frac{1}{2}(1 \pm \hat{\Pi}). \tag{C.3}$$

The projectors $\hat{\mathcal{P}}_\pm$ satisfy the usual properties of orthogonal projection operators such as $\hat{\mathcal{P}}_+ + \hat{\mathcal{P}}_- = 1$, $\hat{\mathcal{P}}_+ \hat{\mathcal{P}}_- = \hat{\mathcal{P}}_- \hat{\mathcal{P}}_- = 0$, and $(\hat{\mathcal{P}}_\pm)^2 = \hat{\mathcal{P}}_\pm$. Using these properties and the algebra of fermionic operators, it is possible to show that the Hamiltonian Eq. (4.1) can be decomposed as follows

$$\hat{H}(t) = \hat{\mathcal{P}}_+ \hat{H}^{(+)}(t) \hat{\mathcal{P}}_+ + \hat{\mathcal{P}}_- \hat{H}^{(-)}(t) \hat{\mathcal{P}}_-, \tag{C.4}$$

where

$$\hat{H}^{(\pm)}(t) = -g(t) \sum_{i=1}^{N} (1 - 2\hat{c}_i^\dagger \hat{c}_i) - J \sum_{i=1}^{N} (\hat{c}_i^\dagger - \hat{c}_i)(\hat{c}_{i+1}^\dagger + \hat{c}_{i+1}). \tag{C.5}$$

To perform the splitting we have defined antiperiodic boundary conditions in the even (+) subspace $\hat{c}_{N+1} = -\hat{c}_1$ and periodic boundary conditions in the odd (−) subspace $\hat{c}_{N+1} = \hat{c}_1$. In this thesis we focus on the projection $\hat{H}^{(+)}$ in the even subspace. Translational invariance suggest to use the discrete Fourier transform

$$\hat{c}_n = \frac{e^{-\mathrm{i}\pi/4}}{\sqrt{N}} \sum_k \hat{c}_k e^{\mathrm{i}kn} = \frac{e^{-\mathrm{i}\pi/4}}{\sqrt{N}} \sum_{k \geq 0} \left(\hat{c}_k e^{\mathrm{i}kn} + \hat{c}_{-k} e^{-\mathrm{i}kn} \right), \tag{C.6}$$

which is compatible with the antiperiodic boundary conditions when

$$k \in \left\{ \pm\frac{\pi}{N}, \pm\frac{3\pi}{N}, \ldots, \pm\frac{(N-1)\pi}{N} \right\}. \tag{C.7}$$

The discrete Fourier transform maps $\hat{H}^{(+)}$ into Hamiltonian Eq. (4.6).

D. The QPT in the anisotropic XY spin chain in a transverse field

Here we consider the critical behavior in a model described by the Hamiltonian

$$\hat{H} = -h\sum_{i=1}^{N}\sigma_i^x - \sum_{i=1}^{N}(J_z\sigma_i^z\sigma_{i+1}^z + J_y\sigma_i^y\sigma_{i+1}^y), \tag{D.1}$$

which is unitarily equivalent to the Hamiltonian of an anisotropic XY spin chain in a transverse field [96, 97, 98].

Similarly to the Ising model, after Jordan-Wigner transformation (C.1), and a discrete Fourier transform (C.6), the Hamiltonian Eq. (D.1) in the even subspace (the subspace with a even number of fermionic quasiparticles) acquires the form

$$\begin{aligned}\hat{H} &= \sum_{k\geq 0}\left\{2\left[h-(J_z+J_y)\cos k\right](\hat{c}_k^\dagger\hat{c}_k + \hat{c}_{-k}^\dagger\hat{c}_{-k}) - 2h\right\} \\ &\quad + \sum_{k\geq 0} 2(J_z-J_y)\sin k(\hat{c}_k^\dagger\hat{c}_{-k}^\dagger + \hat{c}_{-k}\hat{c}_k).\end{aligned} \tag{D.2}$$

The diagonalization of this Hamiltonian is completed after a Bogoliubov transformation,

$$\hat{H} = \sum_k E_k\left(\hat{\gamma}_k^\dagger\hat{\gamma}_k - \frac{1}{2}\right), \tag{D.3}$$

where

$$E_k = 2\sqrt{\left(h-(J_z+J_y)\cos k\right)^2 + \left[(J_z-J_y)\sin k\right]^2}. \tag{D.4}$$

The system exhibits an Ising-like QPT along the lines $|h| = J_z+J_y$ and an anisotropic QPT along the line $J_z = J_y$, providing that $|h| < J_z+J_y$. The anisotropic transition is characterized by two ferromagnetic phases, i.e., for $J_z > J_y$ the system is in a ferromagnetically ordered phase along z direction FMZ, while it is the other way around in the FMY phase. Similarly to reference [96], we consider a reparametrization of

the asymmetries

$$J_z = \frac{J}{2}(1+\gamma),$$
$$J_y = \frac{J}{2}(1-\gamma), \tag{D.5}$$

where γ is dimensionless parameter characterizing the degree of anisotropy in the zy-plane. Under this reparametrization, the Ising-like critical lines correspond to $|h| = J$, and the anisotropic transition occurs at $\gamma = 0$, as long as $|h| < J$.

Interestingly, in the absence of a transverse field, i.e., for $h = 0$, the scaled ground-state energy can be written in the thermodynamic limit as

$$\begin{aligned} E_{GXY} &= -\lim_{N\to\infty} \frac{1}{N}\sum_k \frac{E_k}{2} \\ &= -J\int_{-\pi}^{\pi} \frac{dk}{2\pi}\sqrt{1-(1-\gamma^2)\sin^2 k} \\ &= -\frac{2J}{\pi}E[1-\gamma^2], \end{aligned} \tag{D.6}$$

where $E[z]$ is the complete elliptic integral of the second kind [48]. The scaled ground state energy exhibits a nonanalyticity of the second derivative at the critical line of the anisotropic transition $\gamma = 0$ [96], which is a generic characteristic of a second-order QPT [3].

E. Numerical calculation of the expectation values

By using the BCS ansatz Eq. (4.7) we can solve the Schrödinger equation for the Ising model in terms of the solution of the Schrödinger equation for an effective two-level system described by the BdG Hamiltonian Eq. (4.8), which is parametrized by the quasimomentum $k \in \{\pm\frac{\pi}{N}, \pm\frac{3\pi}{N}, \ldots, \pm\frac{(N-1)\pi}{N}\}$.

In the numerical calculation we assume that the system is prepared initially in the unoccupied state $|0_{-k}, 0_k\rangle$, which implies that $\Psi_k^\dagger(0) = (u_k^*(0), v_k^*(0)) = (0,1)$. After numerical integration of the dynamical BdG Eq. (4.9), we find the spinor $\Psi_k(t)$. To calculate the scaled expectation value of the transverse magnetization $M_x(t) = \frac{1}{N}\left\langle \sum_{i=1}^N \sigma_i^x \right\rangle$ for a given system size N we use the formula

$$M_x(t) = -\frac{2}{N}\sum_{k\geq 0}[\Psi_k(t)]^\dagger \sigma^z(k)\Psi_k(t). \tag{E.1}$$

In the last expression we have used the definition of $\sigma^z(k)$ given in Eq. (4.37). For example, to calculate the dynamics of the system for $N = 4$, we perform the

numerical integration of Eq. (4.9) for $k \in \{\frac{\pi}{4}, \frac{3\pi}{4}\}$. Based on the solution of this equation we find the solution of the Schrödinger equation for Hamiltonian Eq. (4.1) using the BCS ansatz

$$|\psi, t\rangle = |\psi_{\pi/4}, t\rangle \otimes |\psi_{3\pi/4}, t\rangle, \tag{E.2}$$

where

$$|\psi_{\pi/4}, t\rangle = \left[u_{\pi/4}(t)|1_{-\pi/4}, 1_{\pi/4}\rangle + v_{\pi/4}(t)|0_{-\pi/4}, 0_{\pi/4}\rangle\right], \tag{E.3}$$

and

$$|\psi_{3\pi/4}, t\rangle = \left[u_{3\pi/4}(t)|1_{-3\pi/4}, 1_{3\pi/4}\rangle + v_{3\pi/4}(t)|0_{-3\pi/4}, 0_{3\pi/4}\rangle\right]. \tag{E.4}$$

F. Cycle-averaged correlation functions

In this section we perform a description of the calculation of the spin correlation functions in nonequilibrium of the i^*-th Ising chain described by Hamiltonian Eq. (4.1). In particular, we are interested in the spin spatial correlations

$$\eta_{\alpha\alpha}(R, t) = \left\langle \Phi_m^{(-)}(t) \left| \sigma_1^\alpha \sigma_{1+R}^\alpha \right| \Phi_m^{(-)}(t) \right\rangle \tag{F.1}$$

for $\alpha \in \{y, z\}$, where

$$\begin{aligned} |\Phi_m^{(-)}(t)\rangle &= \exp(-\mathrm{i}NE_m^{(-)}t)\hat{U}_m(t) \bigotimes_{k>0} |\chi_{k,m}^{(-)}\rangle \\ &= \exp(-\mathrm{i}NE_m^{(-)}t)\hat{U}_m(t)|\chi_m^{(-)}\rangle \end{aligned} \tag{F.2}$$

is the negative-quasienergy Floquet eigenstate, where $E_m^{(-)} = -\int_0^\pi \frac{dk}{2\pi}\varepsilon_{k,m}$ is the total quasienergy—$\varepsilon_{k,m}$ is the quasienergy dispersion defined in Eq. (4.27). Without loss of generality, let us perform here the explicit calculation for the particular case $\alpha = z$:

$$\begin{aligned} \eta_{zz}(R, t) &= (1 + \cos[4\alpha_m(t)]) \left\langle \chi_m^{(-)} \left| \sigma_1^z \sigma_{1+R}^z \right| \chi_m^{(-)} \right\rangle \\ &\quad + (1 - \cos[4\alpha_m(t)]) \left\langle \chi_m^{(-)} \left| \sigma_1^y \sigma_{1+R}^y \right| \chi_m^{(-)} \right\rangle \\ &\quad + \sin[4\alpha_m(t)] \left(\left\langle \chi_m^{(-)} \left| \sigma_1^z \sigma_{1+R}^y \right| \chi_m^{(-)} \right\rangle + \left\langle \chi_m^{(-)} \left| \sigma_1^y \sigma_{1+R}^z \right| \chi_m^{(-)} \right\rangle \right). \end{aligned} \tag{F.3}$$

After averaging over a cycle we get

$$\begin{aligned} \frac{1}{T}\int_0^T \eta_{zz}(R, t) &= \left[1 + (-1)^m \mathcal{J}_m\left(\frac{4B_1}{\Omega}\right)\right] \left\langle \chi_m^{(-)} \left| \sigma_1^z \sigma_{1+R}^z \right| \chi_m^{(-)} \right\rangle \\ &\quad + \left[1 - (-1)^m \mathcal{J}_m\left(\frac{4B_1}{\Omega}\right)\right] \left\langle \chi_m^{(-)} \left| \sigma_1^y \sigma_{1+R}^y \right| \chi_m^{(-)} \right\rangle \end{aligned} \tag{F.4}$$

Bibliography

[1] L. D. Landau, Z. Sowjetunion **11**, 26 (1937).

[2] L. D. Landau, and E. M. Lifschitz, *Statistical Physics—Course of Theoretical Physics Vol. 5* (Pergamon, London, England, 1999).

[3] S. Sachdev, *Quantum Phase Transitions* (Cambridge University Press, Cambridge, England, 1999).

[4] K. Binder, Rep. Prog. Phys. **50**, 783 (1987).

[5] A. Yu. Kitaev, Ann. Phys. (NY) **303**, 2 (2003)

[6] A. Yu. Kitaev, Ann. Phys. (NY) **321**, 2 (2006)

[7] H. Aoki and T. Ando, Solid State Commun. **38**, 1079 (1981)

[8] D. J. Thouless, M. Kohmoto, M. P. Nightingale, and M. den Nijs, Phys. Rev. Lett. **49**, 405 (1982)

[9] A. Yu. Kitaev, Phys. Usp. **44**, 131 (2001)

[10] M. Z. Hasan, and C. L. Kane, Rev. Mod. Phys. **82**, 3045 (2010).

[11] X.-L. Qi, and S.-C. Zhang, Rev. Mod. Phys. **83**, 1057 (2011).

[12] J. Dziarmaga, Phys. Rev. Lett. **95**, 245701 (2005).

[13] T.W. B. Kibble, J. Phys. A **9**, 1387 (1976); Phys. Rep. **67**, 183 (1980); W. H. Zurek, Nature (London) **317**, 505

[14] A. Altland, V. Gurarie, T. Kriecherbauer, and A. Polkovnikov, Phys. Rev. A **79**, 042703 (2009).

[15] A. Polkovnikov, K. Sengupta, A. Silva, and M. Vengalattore, Rev. Mod. Phys. **83**, 863 (2010).

[16] A. Eckardt, C. Weiss, and M. Holthaus, Phys. Rev. Lett. **95**, 260404 (2005).

[17] G. Vacanti, S. Pugnetti, N. Didier, M. Paternostro, G. M. Palma, R. Fazio, and V. Vedral, Phys. Rev. Lett. **108**, 093603 (2012).

[18] C. E. Creffield, and T. S. Monteiro, Phys. Rev. Lett. **96**, 210403 (2006).

[19] N. H. Lindner, G. Refael, and V. Galitski, Nat. Phys. **7**, 490 (2011).

[20] J. Inoue, and A. Tanaka, Phys. Rev. Lett. **105**, 017401 (2011).

[21] R. H. Dicke, Phys. Rev. **93**, 99 (1954).

[22] K. Hepp and E.H. Lieb, Phys. Rev. A **8**, 2517 (1973).

[23] C. Emary and T. Brandes, Phys. Rev. Lett. **90**, 044101 (2003); Phys. Rev. E **67**, 066203 (2003).

[24] K. Baumann, C. Guerlin, F. Brennecke, and T. Esslinger, Nature (London) **464**, 1301 (2010).

[25] R. Mottl, F. Brennecke, K. Baumann, R. Landig,T. Donner, and T. Esslinger, Science **336**, 1570 (2012).

[26] K. Baumann, R. Mottl, F. Brennecke, and T. Esslinger, Phys. Rev. Lett. **107**, 140402 (2011).

[27] M. W. Johnson, et. al, Nature (London) **473**, 194 (2011).

[28] J. Barreiro, M. Müller, P. Schindler, D. Nigg, T. Monz, M. Chwalla, M. Hennrich, C. F. Roos, P. Zoller, and R. Blatt, Nature (London) **470**, 486 (2011).

[29] J. Simon, B. S. Bakr, R. Ma, M. E. Tai, P. M. Preiss, and M. Greiner, Nature (London) **472**, 307 (2011).

[30] R. Coldea, D. A. Tennant, E. M. Wheeler, E. Wawrzynska, D. Prabhakaran, M. Telling, K. Habitch, P. Smeibidl, and K. Kiefer, Science **327**, 177 (2010).

[31] S. Mostame and R. Schützhold, Phys. Rev. Lett. **101**, 220501 (2008).

[32] S. Trotzky, P. Cheinet, S. Fölling, M. Feld, U. Schnorrberger, A. M. Rey, A. Polkovnikov, E. A. Demler, M. D. Lukin, and I. Bloch, Science **319**, 295 (2008).

[33] H. Lignier, C. Sias, D. Ciampini, Y. Singh, A. Zenesini, O. Morsch, and E. Arimondo, Phys. Rev. Lett. **99**, 220403 (2007).

[34] L.-M. Duan, E. Demler and M.D. Lukin, Phys. Rev. Lett. **91**, 090402 (2003).

[35] A. Micheli, G. K. Brennen, and P. Zoller, Nature Phys. **2**, 341 (2006).

[36] H. Weimer, M. Müller, I. Lesanovsky, P. Zoller, and H. P. Büchler, Nature Phys. **6**, 382 (2010).

[37] P. Nataf and C. Ciuti, Nature Commun. **1**, 1 (2010).

[38] O. Viehmann, J. von Delft, and F. Marquardt, Phys. Rev. Lett. **107**, 113602 (2011).

[39] S. De Liberato, D. Gerace, I. Carusotto, and C. Ciuti, Phys. Rev. A **80**, 053810 (2009).

[40] P. Alsing, D.-S. Guo, and H. J. Carmichael, Phys. Rev. A **45**, 5135 (1992).

[41] V. Peano and M. Thorwart, Phys. Rev. B **82**, 155129 (2010).

[42] J. Hausinger and M. Grifoni, Phys. Rev. A **83**, 030301 (R) (2011).

[43] V. M. Bastidas, C. Emary, B. Regler and T. Brandes, Phys. Rev. Lett. **108**, 043003 (2012).

[44] T. Holstein and H. Primakoff, Phys. Rev. **58**, 1098 (1949).

[45] V. M. Bastidas, J. H. Reina, C. Emary, and T. Brandes, Phys. Rev. A **81**, 012316 (2010).

[46] V. I. Arnold, *Mathematical Methods of Classical Mechanics* (Springer-Verlag, New York, 1978).

[47] A.M. Perelomov and V. S. Popov, Teor. Mat. Fiz. **1**, 360 (1969).

[48] M. Abramowitz and I. A. Stegun, *Handbook of Mathematical Functions with Formulas, Graphs and Mathematical Tables*, edited by M. Abramowitz and I. A. Stegun (Dover, New York, 1972).

[49] B. Öztop, M. Bordyuh, Ö. E. Müstecaplıoğlu, and H. E. Türeci, New Journal of Physics **14**, 085011 (2012) .

[50] J. H. Shirley, Phys. Rev. **138**, B979 (1965).

[51] E. K. Irish, Phys. Rev. Lett. **99**, 173601 (2007).

[52] S. Ashhab, J. R. Johansson, A. M. Zagoskin, and F. Nori, Phys. Rev. A **75**, 063414 (2007).

[53] M. Aparicio Alcalde, and B. M. Pimentel, Physica A **390**, 3385 (2011); J. Keeling, M. J. Bhaseen, and B. D. Simons, Phys. Rev. Lett. **105**, 043001 (2010).

[54] D. Nagy, G. Kónya, G. Szirmai, and P. Domokos, Phys. Rev. Lett. **104**, 130401 (2010)

[55] F. Dimer, B. Estienne, A. S. Parkins, and H. J. Carmichael, Phys. Rev. A **75**, 013804 (2007).

[56] G. Günter et al., Nature (London) **458**, 178 (2009).

[57] M. Sandberg et al., Appl. Phys. Lett. **92**, 203501 (2008).

[58] H. Lipkin, N. Meshkov, and A. Glick, Nucl. Phys. **62**, 188 (1965); N. Meshkov, A. Glick, and H. Lipkin, Nucl. Phys. **62**, 199 (1965); A. Glick, H. Lipkin, and N. Meshkov, Nucl. Phys. **62**, 211 (1965) .

[59] J. Ma, X. Wang, C. P. Sun, and F. Nori, Phys. Rep. **509**, 89 (2011) .

[60] J. Ma and X. Wang, Phys. Rev. A **80**, 012318 (2009) .

[61] P. Solinas, P. Ribeiro, and R. Mosseri, Phys. Rev. A **78**, 052329 (2008) .

[62] T. Caneva, R. Fazio, and G. E. Santoro , Phys. Rev. B **78**, 104426 (2008) .

[63] J. Gong, L. Morales-Molina, and P. Hänggi, Phys. Rev. Lett. **103**, 133002 (2009).

[64] A. Das, K. Sengupta, D. Sen, and B. K. Chakrabarti, Phys. Rev. B **74**, 144423 (2006).

[65] C. Hicke and M. I. Dykman, Phys. Rev. B **78**, 024401 (2008) .

[66] G. Engelhardt, V. M. Bastidas, C. Emary, and T. Brandes, Phys. Rev. E **87**, 052110 (2013) .

[67] P. Ribeiro, J. Vidal, and R. Mosseri, Phys. Rev. E **78**, 021106 (2008) .

[68] S. Dusuel and J. Vidal, Phys. Rev. B **71**, 224420 (2005) .

[69] M. Filippone, S. Dusuel, and J. Vidal, Phys. Rev. A **83**, 022327 (2011) .

[70] S. Kohler, T. Dittrich, and P. Hänggi, Phys. Rev. E **55**, 300 (1997).

[71] C. Zerbe, P. Jung, and P. Hänggi, Phys. Rev. E **49**, 3626 (1994) .

[72] M. Thorwart, P. Reimann, and P. Hänggi, Phys. Rev. E **62**, 5808 (2000) .

[73] V. Peano, M. Marthaler, and M. I. Dykman, Phys. Rev. Lett. **109**, 090401 (2012).

[74] V. Peano and M. Thorwart, Phys. Rev. B **82**, 155129 (2010).

[75] V. Leyton, V. Peano and M. Thorwart, New J. Phys. **14**, 093024 (2012).

[76] F. Arecchi, E. Courtens, R. Gilmore, and H. Thomas, Phys. Rev. A **6**, 2211 (1972) .

[77] T. Zibold, E. Nicklas, C. Gross, and M. K. Oberthaler, Phys. Rev. Lett. **105**, 204101 (2010).

[78] S. Morrison and A. S. Parkins, Phys. Rev. Lett. **100**, 040403 (2008) .

[79] S. Morrison and A. S. Parkins, Phys. Rev. A **77**, 043810 (2008) .

[80] J. Larson, Europhys. Lett. **90**, 54001 (2010) .

[81] S. Longhi, Phys. Rev. A **83**, 034102 (2011) .

[82] G. Chen, J. Li, and J. Liang, Phys. Rev. B **76**, 054512 (2007) .

[83] S. Chaudhury, A. Smith, B. E. Anderson, S. Ghose and P. S. Jessen, Nature (London) **461**, 768 (2009) .

[84] Y. C. Liu, Z. F. Xu, G. R. Jin, and L. You, Phys. Rev. Lett. **107**, 013601 (2011).

[85] V. Mukherjee, U. Divakaran, A. Dutta, and D. Sen, Phys. Rev. B **76**, 174303 (2007) .

[86] V. Mukherjee, A. Dutta, and D. Sen, Phys. Rev. B **77**, 214427 (2008) .

[87] S. Miyashita, K. Saito, and H. De Raedt, Phys. Rev. Lett. **80**, 1525 (1998) .

[88] K. Hijii and S. Miyashita, Phys. Rev. A **81**, 013403 (2010) .

[89] A. Das, Phys. Rev. B **82**, 172402 (2010) .

[90] S. Bhattacharyya, A. Das, and S. Dasgupta, Phys. Rev. B **86**, 054410 (2012) .

[91] A. Russomanno, A. Silva, and G. E. Santoro, Phys. Rev. Lett. **109**, 257201 (2012) .

[92] V. M. Bastidas, C. Emary, G. Schaller, and T. Brandes, Phys. Rev. A **86**, 063627 (2012) .

[93] Y. Niu, S. B. Chung, C. H. Hsu, I. Mandal, S. Raghu, and S. Chakravarty, Phys. Rev. B **85**, 035110 (2012).

[94] L. Goren, E. Mariani, and A. Stern, Phys. Rev. A. **75**, 063612 (2007).

[95] M. Grifoni and P. Hänggi, Phys. Rep. **304**, 229 (1998).

[96] E. Lieb, T. Schultz, and D. Mattis, Ann. Phys. (NY) **16**, 407 (1961).

[97] E. Barouch and B. M. McCoy, Phys. Rev. A **3**, 786 (1971).

[98] J. E. Bunder and R. H. McKenzie, Phys. Rev. B **60**, 344 (1999).

[99] F. Grossmann, T. Dittrich, P. Jung, and P. Hänggi, Phys. Rev. Lett. **67**, 516 (1991).

[100] F. Grossmann and P. Hänggi, Europhys. Lett. **18**, 571 (1992).

[101] J-S. Lee, and A. K. Khitrin, Phys. Rev. A **71**, 062338 (2005)

[102] J-S. Lee, T. Adams, and A. K. Khitrin, New Journal of Physics **9**, 83 (2007)

[103] Z. Nussinov and G. Ortiz, Ann. Phys. **324**, 977 (2009).

[104] B. J. Brown, W. Son, C. V. Kraus, R. Fazio, and V. Vedral, New J. Phys. **13**, 065010 (2011).

[105] J. Vidal, S. Dusuel, and K. P. Schmidt, Phys. Rev. B **79**, 033109 (2009).

[106] J. Vidal, R. Thomale, K. P. Schmidt, and S. Dusuel, Phys. Rev. B **80**, 081104(R) (2009).

[107] V. M. Bastidas, C. Emary, G. Schaller, A. Gómez-León, G. Platero, and T. Brandes, arXiv:1302.0781

[108] X.-G. Wen, Phys. Rev. D **68**, 065003 (2003).

[109] J. Yu, S.-P. Kou, and X.-G. Wen, Europhys. Lett. **84**, 17004 (2008).

[110] I. Peschel, J. Stat. Mech. (2004) P12005.

[111] M. M. Wolf, G. Ortiz, F. Verstraete, and J. I. Cirac, Phys. Rev. Lett. **97**, 110403 (2006)

[112] L. Zhang, S-P. Kou, and Y. Deng, Phys. Rev. A **83**, 062113 (2011).

[113] K. Damle and S. Sadchev, Phys. Rev. Lett. **76**, 4412 (1996).

[114] L. Jiang, T. Kitagawa, J. Alicea, A. R. Akhmerov, D. Pekker, G. Refael, J. I. Cirac, E. Demler, M. D. Lukin, and P. Zoller, Phys. Rev. Lett. **106**, 220402 (2011).

[115] A. Gómez-León and G. Platero, Phys. Rev. B **86**, 115318 (2012).

[116] M. Tomka, A. Polkovnikov, and V. Gritsev, Phys. Rev. Lett. **108**, 080404 (2012).

[117] T. Oka and H. Aoki, Phys. Rev. B **79**, 081406(R) (2009).

[118] A. Gómez-León and G. Platero, Phys. Rev. Lett. **110**, 200403 (2013).

[119] T. Kitagawa, E. Berg, M. Rudner, and E. Demler, Phys. Rev. B **82**, 235114 (2010).